Torque Performance of Optimally Designed Multi-Phase Reluctance DC Machines

Edward Tshitshiri Rakgati

Dissertation presented for the degree of Doctor of Philosophy in Electrical Engineering at the University of Stellenbosch

Promoter:

Prof. Maarten J. Kamper

December 2006

Declaration

The work presented in this dissertation was carried out in the Department of Electrical and Electronic Engineering, University of Stellenbosch under the supervision of Prof. M.J. Kamper from July 2002 to June 2006.

The author wishes to declare that the work contained in this dissertation is his own original work, unless otherwise stated, and has not previously in its entirety or in part submitted at any other university for a degree, diploma or other qualification.

E.T. Rakgati

Signature

Acknowledgements

I would like to express my sincere appreciation to:

- My promoter Prof. M.J. Kamper for his supervision and constant encouragement during the course of the project.
- My sponsor, University of Botswana, for providing financial assistance.
- Dr. R. Wang for his assistance with the finite element software.
- Mr Y. Ai, whom we constantly shared ideas on theoretical and control aspects of brushless DC machines.
- Mr. A. Le Roux for designing the digital signal processors and his constant assistance with the development of the control program.
- Mr. H. de Kock for his assistance in the development of the control program.
- All the people in the workshop for the assembling of the machine and the preparation of the test set up of the machine.
- Mr. F. Rossouw and Mr. A. Swart for the technical support regarding the building of the converter and the practical set up.
- My wife for her love and understanding of the situation and her encouragement.

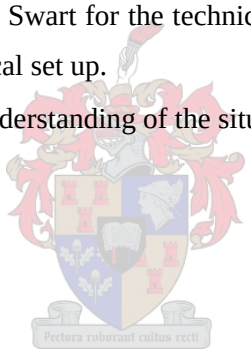

Abstract

The focus of this thesis is on the critical evaluation of the torque performance of the optimum designed reluctance DC machine (RDCM). The thesis focuses on multi-phase RDCM drives with normal laminated salient pole rotors allowing for high power and high-speed applications.

An RDCM is a normal reluctance synchronous machine (RSM) but with direct control of flux and torque just as in brush DC machines. Flux and torque of the RDCM are controlled directly by the use of special phase current waveforms. Specific attention is given in the thesis for the selection of the best current waveform for the RDCM allowing for smooth rotating airgap MMF and less ripple torque.

The absolute optimum designed RDCM can best be obtained by the use of the finite element (FE) method in the design optimisation process. In this thesis a multi-dimensional FE based design optimisation method for the optimum design of the current controlled RDCM is implemented. To compare the torque performance of the RDCM with other RSMs the torque performances of optimum designed 3-phase, 5-phase and 5-phase with the injection of third harmonic current RSMs are performed under the same copper losses and stack volume. The torque performances of RSMs are done with both salient pole rotor and the round rotor with internal flux barriers.

The armature reaction effect of 6-phase RDCMs is also investigated in detail by considering three different rotor structures. These rotor structures are the standard salient pole rotor, the salient pole rotor with slitted poles and the salient pole rotor with chamfered poles. It was shown that the RDCM with the salient pole rotor has a severe armature reaction effect, which can be reduced by slitted or chamfered salient pole rotors.

A per-phase equivalent circuit model of the 6-phase RDCM is also proposed in this thesis. The torque of the machine is calculated based on the per-phase equivalent model and compared with the torque calculated by the FE Maxwell stress tensor method. There is a good agreement between these calculated torques. This thesis shows that the implemented FE based optimisation method can be applied with success to optimally design current controlled RDCMs. It was found, amongst other things, that the torque performance of the optimum designed 6-phase RDCM is slightly higher than that of the optimum designed 5-phase RSM with the injection of 3rd harmonic currents and with the same copper losses and stack volume. The analytical and FE calculated results are confirmed by measured results on a 35 kW 6-phase RDCM drive.

Sinopsis

Die fokus van hierdie tesis is op die kritiese evaluering van die draaimoment-werkverrigting van die optimum ontwerpte reluktansie GS masjien (RGSM). Die tesis fokus op multi-fase RGSM aandrywing met normaal gelamelleerde speekpool rotors wat vir hoë drywing en hoë spoed toepassings toelaat.

‘n RGSM is ‘n normale reluktansie sinchroonmasjien (RSM) maar met direkte beheer van die vloed en die draaimoment, net soos in geborselde GS masjiene. Vloed en draaimoment van die RGSM word beheer direk deur die gebruik van spesiale fase-stroom-golfvorms. Spesifieke aandag word in die tesis gegee aan die keuse van die beste stroom-golfvorm vir die RGSM wat vir ‘n gladde rotasie luggaping MMK en ‘n lae riffeldraaimoment toelaat.

Die absoluut optimum ontwerpte RGSM kan op sy beste verkry word deur die eindige element (EE) metode in die ontwerp-optimeringsproses te gebruik. In hierdie tesis word ‘n multidimensionele EE gebaseerde ontwerp optimeringsmetode vir die optimum ontwerp van die stroom beheerde RGSM geimplementeer. Om die draaimoment-werkverrigting van die RGSM te vergelyk teenoor die van ander RSMe, word die draaimoment-werkverrigting van optimum ontwerpte 3-fase, 5-fase en 5-fase met die byvoeging van 3^{de} harmoniekstrome RSMe teen dieselfde koperverliese en pak volume. Die draaimoment-werkverrigting van RSMe word gedoen met beide speekpoolrotor en ronde rotor met interne vloedmure.

Die ankerreaksie effek van die 6-fase RGSM word ook ondersoek deur gebruik te maak van die optimum RGSM met drie verskillende rotor strukture. Die drie verskillende rotor strukture is die standaard speekpool rotor, die speekpool rotor met gegleufde pole en die speekpool rotor met geronde pole. Dit was gewys dat die RGSM met die speekpool rotor hoë ankerreaksie effek het, wat verminder kan word deur gegleufde of geronde pool rotors.

‘n Per-fase ekwivalente stroombaan model van die 6-fase RGSM word ook voorgestel in die tesis. Die draaimoment van die masjien word bereken gebaseer op die per-fase ekwivalente model en vergelyk met die draaimoment bereken deur die “FE Maxwell stress tensor” metode. Daar is ‘n goeie bymekaarkoming tussen hierdie berekende draaimomente. Die tesis toon dat die voorgestelde EE optimeringsmetode met sukses toegepas kan word om die ontwerp van die stoom beheerde RGSMe te optimeer. Dit was onder andere gevind dat die draaimoment-werkverrigting van die optimum ontwerpte 6-fase RGSM effens hoëer is as die van die optimum 5-fase met die byvoeging van 3^{de} harmoniekstrome RSM teen dieselfde koperverliese en pak volume. Die analitiese en eindige element berekende resultate was bevestig deur gemete resultate op ‘n 35kW 6-fase RGSM.

Pectora roborant cultus recti

Table of Contents

List of Symbols

I_s	space vector of stator currents [**A∠rad**]
I_m	amplitude of the current phasor [A]
I_{m3}	amplitude of the 3rd harmonic current phasor [A]
r_s	stator resistance [Ω]
V_s	space vector of stator voltage [**V∠rad**]
λ_s	space vector of stator flux linkage [**Wb∠rad**]
i_{abc}	instantaneous values of phase currents a, b, c, [A]
v_{abc}	instantaneous values of phase voltages a, b, c, [V]
e_{abc}	instantaneous values of phase back EMFs a, b, c [V]
λ_{abc}	instantaneous values of phase flux linkages a, b, c [Wb]
k_p	Parks transformation matrix
k_t	5-phase transformation matrix
k_{t3}	5-phase +3rd harmonic transformation matrix
ω_r	rotor speed [rad/s]
p	number of pole pairs
L_d, L_q	d and q-axis self inductance [H]
N	number of turns in series per phase
ρ_t	resistivity of conductor at temperature, t [Ω m]
μ_0	absolute permeability [H/m]
l	axial length of the stator/rotor stack [m]
l_e	average length of a coil end [m]
n_a	number of parallel circuits of the stator winding
A_{cu}	active copper area of a stator slot [m^2]
z	number of conductors per slot, alternatively the z-direction.
J	current density [A/m^2]
q	number of slots per pole per phase
θ_r	rotor position [rad]
θ	airgap position [rad]
λ_{abc1}	instantaneous values of fundamental flux linkages of phases a, b, c [Wb]
λ_{abc3}	instantaneous values of 3rd harmonic flux linkages of phases a, b, c [Wb]
T	torque [Nm]
α	current angle [rad]
P_{cu}	copper losses [kW]
V_d, V_q	steady state d- and q-axis stator voltage components [V]

I_d, I_q	steady state d- and q-axis stator current components [A]
V_{d1}, V_{q1}	steady state values of fundamental d- and q-axis stator voltage [V]
V_{D1}, V_{Q1}	steady state values of fundamental D- and Q-axis stator voltage [V]
V_{d3}, V_{q3}	steady state values of 3rd harmonic d- and q-axis stator voltage [V]
I_{d1}, I_{q1}	steady state values of fundamental d- and q-axis currents [A]
I_{d3}, I_{q3}	steady state values of 3rd harmonic d- and q-axis currents [A]
t_w	tooth width [m]
S_{yh}	stator yoke height [m]
d_i	stator inner diameter [m]
d_o	stator outer diameter [m]
st_gw	slot gap width [m]
d_r	rotor outer diameter [m]
d_{sh}	rotor shaft diameter [m]
b_1, b_2, b_3, b_4	four barrier widths [m]
r_c	rotor cut-out depth [m]
σ	rotor cut-out angle [deg.]
β	slot-pitch angle [deg.]
ϕ	sub-machine displacement angle [deg.]
I_F	field current [A]
I_T	torque current [A]
γ	I_F/I_T
φ_q	q-axis flux vector [Wb]
φ_m	magnet flux vector [Wb]
φ_F	field flux vector [Wb]
φ_T	torque flux vector [Wb]
Θ_F	field current conducting angle [deg.]
Θ_T	torque current conducting angle [deg.]
ϑ	θ_F/θ_T
Θ_p	rotor pole arc angle [deg.]
Θ_τ	rotor pole pitch angle [deg.]
m_T	number of torque conducting phases
m_F	number of field conducting phases
B_g	average airgap flux density [T]
r_g	radius of the airgap [m]
Θ_{ps}	rotor pole arc angle with skew taken into account [deg.]

b_p	barrier pitch [m]
b_w	barrier width [m]
ψ	b_w/b_p
L_{abc}	instantaneous values of phase self inductance a, b, c [H]
F	magnetomotive force (MMF) [At]
$\vec{F}_{abcde}$	space phasor of the airgap MMF for the phase coils a - e [$\mathbf{At \angle rad}$]
$\vec{F}_{abcde1}$	space phasor of the fundamental airgap MMF for phase coils a – e [$\mathbf{At \angle rad}$]
$F_{abcde1\,peak}$	amplitude of the fundamental airgap phase MMF [At]
$\vec{F}_s$	resultant stator MMF phasor [$\mathbf{At \angle rad}$]
F_s	amplitude of the space phasor MMF [At]
θ_{F_s}	orientation of the space phasor MMF [rad.]

Abbreviations

FE	Finite Element
EMF	Electromotive Force
RSM	Reluctance Synchronous Machine
RDCM	Reluctance Direct Current Machine
DSP	Digital Signal Processor
VSI	Voltage Source Inverter
BDCM	Brushless Direct Current machine
PWM	Pulse Width Modulation
5 + 3rd RSM	5 – phase with the injection of 3rd harmonic currents RSM
CR–rotor	salient pole rotor with no internal barriers but only cut - outs
FBR–rotor	round rotor with internal barriers

CHAPTER 1 Introduction

Reluctance machines can be classified as either single-salient or double salient reluctance machines. The distinction between the machines is due to the fact that the double salient machine has saliency both on the stator and on the rotor as compared to the single salient reluctance synchronous machine (RSM) that has non-salient pole stators but salient-pole rotors or rotors (non-salient or salient) with magnetic symmetry. The single salient-reluctance machines can be further categorised into brushless AC machines and brushless DC machines. The brushless AC machines are the well-known RSMs that are sinusoidal current driven machines. RSMs have attracted the efforts of various researches especially on the rotor design of the machine. The various research work done focussed on the following types of rotor structures [Kostko (1923), Brinkman (1965), Hosinger (1971), El-Anatably (1985), Matsuo (1994), Kamper (1994), kamper (1996), Vagati (2000)]: (i) salient-pole rotor with cutouts and with/without internal flux barriers; (ii) normal (transverse) laminated round rotor with internal flux barriers; (iii) axially laminated rotors which might be round or with salient poles. In addition to sinusoidal current driven RSMs there are various research work done on torque performance of 5-phase RSMs with the injection of 3rd harmonic currents with both salient pole and round axially laminated rotors [Toliyat (1992, 1998), Xu (1992, 2000)]. Examples of two-pole RSMs with salient-pole and internal-flux barrier rotors are shown in Figure 1.

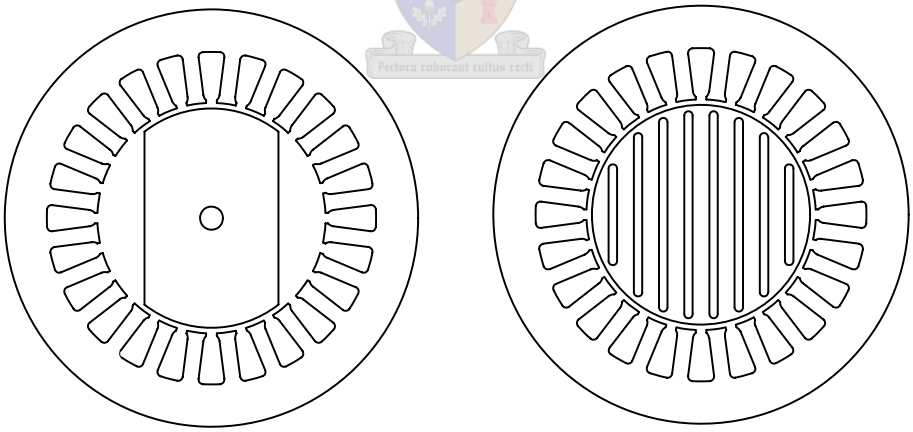

(a) (b)

Figure 1: Two-pole RSMs with (a) salient-pole and (b) internal-flux-barrier rotors.

The brushless DC machines unlike the brushless AC machines are driven by special current waveforms. The special current waveforms in this particular case refer to square, flat-topped current waveforms that have flat-topped DC amplitudes. The focus of this thesis is on brushless DC machines and for the sake of this thesis they are referred to as Reluctance DC machines (RDCMs). RDCMs are practically unknown; the operation principle of the machine

is derived from the well-known brushless DC machines, which are permanent magnet machines. So far, publications on RDCMs are by the following authors: Weh (1984), Mayer (1986), Boldea (1991) and Law (1994, 1996). RDCMs can be defined as RSMs with a salient pole rotor and driven by special current waveforms. The special current waveforms allow that the RDCM be controlled just like a brush DC machine, that is, allowing for field and torque currents to be controlled directly and separately without the need of complex transformations. RDCMs unlike brush DC machines, do not have brushes, hence are referred to as brushless DC machines. The current commutation in an RDCM, unlike in a brush DC machine, is done by means of power electronic switches. Just like for any other RSM, the special current waveform of the RDCM is controlled as a function of position allowing the current to be placed appropriately according to the rotor position.

Why reluctance DC machines? RDCM drives are attractive for drive applications over other reluctance machines because of the following:

(i) The normal disadvantage of reluctance machines of low power or low torque density, poor efficiency and low power factor can be overcome if current and flux distribution are arranged and optimised similar to a situation and configuration given in brush DC machines. This, as initiated by Weh (1984), can be achieved by the multi-phase armature winding and inverter concept on the basis of a coil by coil commutation.

(ii) The control of RDCMs is simple, as the field and torque currents can be controlled directly and independently without any complex transformations.

(iii) With the multi-phase RDCM drive with a salient pole rotor the application can be for high power (using multiphase solid state converter), high-speed low maintenance drives for the petrochemical and mining industry, amongst others, where any arcing e.g. within the electrical machine is not allowed. This thesis focuses specifically on the multiphase, salient pole rotor RDCM drive.

In addition to the attractiveness of the RDCM drive, the RDCM just like any other RSM drive has the following advantages:

(i) There are basically no rotor losses if the rotor is correctly designed, therefore, the rotor stack, shaft and bearings run cooler than the machines with rotor windings.

(ii) The cooling of the machine is less of a problem than in cage-rotor machines as all the losses are concentrated on the stator.

(iii) With no brushes and rotor windings, the RDCM requires less maintenance hence it is more reliable than cage-rotor machines.

With the use of power electronics and current control methods, the performance of reluctance machines, more especially the power or torque density of the machine, can be improved, hence, justifies further research on current controlled RDCMs.

In the next sections an overview of the history of the RDCM is given with the corresponding important publications on the machines. This is followed by the problem statement for the research necessary on the RDCM drive and the approach in solving the problem. Finally the thesis layout is given.

1.1 The history of Reluctance DC machine

The RDCM drive could not be a success if it was not for the advent and intensive use of power electronics in the mid 1970s. It should be noted that it is impossible to operate an RDCM without power electronic converters as the current commutation is done by means of power electronic switching. From literature, it can be seen that there are very few publications on the RDCM drives. This justifies the need for further research on these machines. The research on RDCMs between 1984 and early 1990s was mainly on the control aspects e.g. current control of the machine. There was nothing in the design of the machine in terms of design optimisation and varying dimensions of either the stator or rotor of the machine as a function of the performance. Publications on RDCM drives are summarised as follows:

(i) The work of Weh (1984 & 1985)

The 6-phase RDCM with normal (transverse) laminated rotor was introduced. The rotor structure as proposed by Weh has a large opening along the d-axis as shown in Figure 1.1 so as to reduce the armature reaction effect. The RDCM is square current driven and the control is done in such a way that two phase windings act as field windings (phases 1 and 2) and four as torque windings (phase 3 - 6) as shown in Figure 1.1. The current control in this particular investigation was done by an analogue hysteresis current controller via a 6-phase half-bridge inverter with neutral clamping. The work of Weh in RDCMs was extended to 7–phase machines with axially laminated salient pole rotors [Weh (1985)], but still with the square current waveforms.

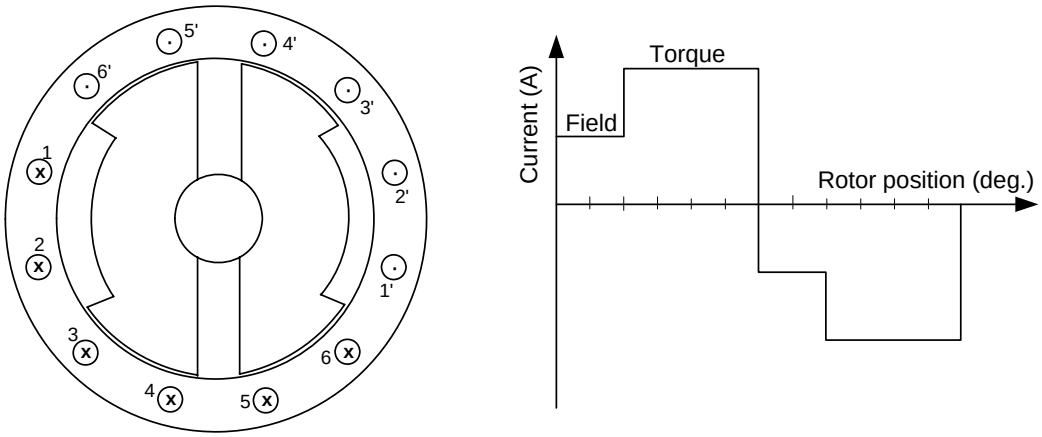

(a) (b)

Figure 1.1:(a) Machine structure (normal laminated) of a 6-phase RDCM and (b) its phase current waveform [Weh (1984)].

(ii) The Work of Mayer (1986)

Mayer focussed on 7-phase RDCMs with field to torque phase winding ratio of 3:4. In this particular investigation, the square current waveform was used as by Weh. The investigation focussed on axially laminated rotor structures. The machine structure showing the details of the rotor structures used are shown in Figure 1.1(c). The reduction of the armature reaction effect was investigated by non-active methods by the use of insulation sheets in between the laminations as shown on the rotor left pole of Figure 1.1(c) and also by active methods by using ferrite permanent magnets in place of insulation sheets as shown on the right pole.

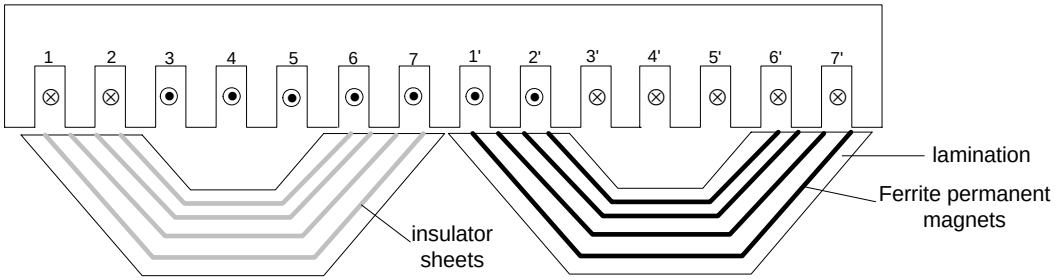

Figure 1.1(c): Machine structure of a 7-phase RDCM showing the axially laminated rotor structure with insulation sheets (left) and with ferrite permanent magnets (right) [Mayer (1986)].

(iii) The Work of Boldea (1991)

Boldea focussed on the same rotor structures and the same square current waveforms as Mayer. The investigation carried out by Boldea focussed on 2-phase, 3-phase and 5-phase RDCMs with field to torque phase winding ratio of 1:1, 1:2 and 2:3 respectively.

(iv) The work of Law (1994, 1996)

Law focussed mainly on the magnetic circuit modelling of 8-phase field regulated reluctance machines. The current waveforms used for the machines were the square current waveform with four field phases and four armature phases. The reluctance machine considered was with an axially laminated rotor structure.

1.2 Problem Statement

As the focus of this thesis is on current controlled RDCMs, it is worth mentioning some design and analysis aspects of the RDCM that stands out from the literature. These are the following:

(i) Axially laminated rotors are not the way forward for further research due to the difficult rotor structure and iron loss problem if large numbers of insulation layers are used. Skewing, which is a way of reducing torque ripple, is very difficult for axially laminated rotors. The iron loss problem as mentioned by Weh (1990) and Vagati (1992), was the main reason behind moving from axially laminated rotors to normal transverse laminated rotors.

(ii) It is amazing that the overall design of the RDCM received no attention in research. From Weh (1984) to Boldea (1991), the research as already mentioned in the history of the RDCMs was more focussed on the control aspects e.g. current control of the machines. In addition to the control aspects of the machine, it is worth considering both the overall design of the machine (stator and rotor) as the machine performance is dependent on the whole machine, not only on the control aspects.

(iii) Most of the design analysis of RDCMs has been done analytically by the use of mathematical formulas. The finite element methods have merely been used for the investigation of the flux density in the air gap with compensated and non-compensated rotor structures [Mayer (1986)] and not to carry out the overall optimum design of the machines. Thus, there seems to be a deficiency in this regard.

(iv) Even though there is some work done by various researchers [Toliyat (1992, 1998), Xu (1992, 2000) on 5-phase RSMs with or without 3^{rd} harmonic currents, it is still not clear how the torque performance of the 3-phase, 5-phase and 5-phase with 3^{rd} harmonic currents with salient pole rotor and round rotor with internal barriers compare. Therefore further research in this regard is necessary.

(v) The special phase current waveforms allow for the simple control of the RDCM with direct control of the flux and torque of the machine. A suitable phase current waveform has to be selected allowing for smooth airgap rotating MMF and less torque ripple. No research has been done in this regard to investigate the phase current waveform to be used for the RDCM.

By keeping the above-mentioned aspects in mind, the question that needs to be answered in this thesis despite the research that has already been done is "What is the torque performance of the multi-phase RDCMs in comparison to other RSMs?" As a first study, this thesis is focussed only on the torque performance of the RDCM, and not on the power factor, efficiency or iron losses of the machine.

When addressing the above-mentioned question it is necessary to carry out an overall machine design (both the stator and the rotor design) optimisation. As the main focus of this thesis is on the torque performance, the torque per copper losses and stack volume as the objective function is maximised for the design optimisation of the RDCM. As a first study, it is necessary to know how the RDCM perform in terms of torque in relation to other RSMs. Therefore, RSMs with same copper losses and stack volume must also be optimised for the same objective function so as to act as a base for the torque comparison of RDCMs and RSMs. An optimisation algorithm is therefore vital to optimise in multi-dimensions the design of both RDCMs and RSMs. It is not conclusive enough to focus on single variables in the design optimisation of the machine; all the machine variables must be optimised for the maximisation (minimisation) of the objective function. The typical number of variables for the design optimisation can easily be up to 10 [Kamper (1996)].

In conclusion, for the above-mentioned designed optimisation to be carried out, the finite element analysis method must be used in some way together with the multi-dimensional optimisation algorithm to optimise the design of the machine. As far as the literature is concerned, this has not been done before for the current controlled RDCM, hence it is the focus of this thesis.

1.3 Approach to problem

The approach followed in this thesis to solve the problem stated in section 1.2 is to try to make use of the finite element program directly in the optimisation procedure. It should also be mentioned that in this thesis only steady state is considered in the design optimisation of

the machines. The Powell optimisation algorithm [Powell (1964)] is used for the design optimisation of the machines.

With the FE commercial packages, it is almost impossible to link the FE to the optimisation algorithm. Therefore for this thesis, the source code of FE program developed at the University of Cambridge [Volshenk (1993)] was used. The FE software was adapted so that it could be used for the analysis of the current controlled RDCM for the first time. With the developed software available for the current controlled RDCM, it was possible to link the FE and the optimisation algorithm to allow for the design optimisation of the machine. With the optimum designed RDCM, the FE torque performance of the machine can then be determined. The FE software was also adapted for the 3-phase, 5-phase and 5-phase with the addition of 3rd harmonic currents so as to derive the torque performance of the optimum designed machines with both the salient pole rotor and the round rotor with internal barriers. The finite element program is described briefly in appendix A and will be referred to in the thesis.

In addressing the question of the suitable current waveform for the RDCM, the analysis of the airgap MMF of the different special current waveforms must be carried out. The best current waveform can then be selected on the basis of outcome of the rotating MMF analysis. The best current waveform will be the one that results in a smooth rotating MMF, less torque ripple and no loss in torque per copper losses.

It is important to give an explanation of the outcomes of the design optimisation. The RDCM suffer from a severe cross coupling effect, therefore, the design optimisation outcomes cannot be explained by analytical methods. These outcomes are thus explained by FE analysis, with particular reference to the cross coupling effect in the machine.

1.4 Thesis Layout

The layout for the remainder of this thesis is as follows:

Chapter 2: In this chapter the steady-state model of the sinusoidal Reluctance synchronous machines is derived. The finite element method of determining the parameters of the model is also described.

Chapter 3: The focus of this chapter is to make a comparative study of the sinusoidal RSM with two rotor structures. It also focuses on the multi-dimensional optimisation of the sinusoidal RSMs with two rotor structures.

Chapter 4: The operation principle of the Reluctance DC machines is described in this chapter. The EMF and the torque equations of the RDCMs are also derived in the chapter.

Chapter 5: The focus of this chapter is on the determination of the torque performance of the optimally designed RDCMs. There is also torque comparison between the optimum designed sinusoidal RSMs and optimum designed RDCMs.

Chapter 6: The per phase modelling of the 6-phase RDCM with the salient pole rotor is described in this chapter. The determination of the different per phase equivalent circuit parameters through FE analysis is described.

Chapter 7: The focus of this chapter is on the measured and FE-calculated torque performance of the built 6-phase RDCM with the salient pole rotor.

Chapter 8: In this chapter, a summary with conclusions is given and recommendations are made for further research.

CHAPTER 2 Review of Sinusoidal RSMs

In this chapter the steady state equivalent circuit diagrams of the sinusoidal RSMs are reviewed. The sinusoidal RSMs considered in this chapter are the 3- phase machine, 5-phase machine and 5- phase with an injection of third harmonic current machine. The 5-phase with an injection of third harmonic current machines are more relevant to the Reluctance dc machines that are described at a later stage in chapter 4. But the 5-phase with an addition of third harmonic current reluctance machine drive is not a commonly known machine, so as background the author starts with the well-known 3-phase RSMs, advances to 5-phase RSMs and finally discusses the 5-phase RSM with an addition of third harmonic currents. In addition to the steady state equivalent circuits, the torque equations of the machines are also given. The method of determining the equivalent circuit parameters of the machines is described with a strong emphasis on the finite element method of determining the *dq* flux linkages. The FE method of determining the flux linkages is used in the next chapter to determine the flux linkages, which can then be used to calculate torque of the machines.

2.1 Three-Phase RSM

In this section the machine model of the 3-phase RSM is defined in the *abc*-reference frame and transformed to the *dq0* reference frame. Based on the steady state *dq0* voltage equations, the equivalent circuit diagram and the torque equations are derived. The determination of the equivalent circuit diagram parameters is also discussed.

2.1.1 dq – Equivalent Circuits

The 3-phase RSM has a normal 3-phase stator. The general equation for the stator voltage, $\mathbf{V}_s$, in the *abc* reference frame in matrix form, is given by

$$\mathbf{V}_s = r_s \mathbf{I}_s + \frac{d\boldsymbol{\lambda}_s}{dt}, \tag{2.1}$$

with $\mathbf{V}_s = \begin{bmatrix} v_a \\ v_b \\ v_c \end{bmatrix}$, $\mathbf{I}_s = \begin{bmatrix} i_a \\ i_b \\ i_c \end{bmatrix}$ and $\boldsymbol{\lambda}_s = \begin{bmatrix} \lambda_a \\ \lambda_b \\ \lambda_c \end{bmatrix}$.

The *abc* voltage equation (2.1) can be transformed to *dq0* voltage equations by the use of Park's transformation as follows

$$\left[V_{dq0}\right] = \left[k_p\right]\left[v_{abc}\right], \tag{2.2}$$

where k_p is the Park's transformation given by

$$k_p = \frac{2}{3}\begin{bmatrix} \cos\theta_r & \cos(\theta_r + \frac{2\pi}{3}) & \cos(\theta_r - \frac{2\pi}{3}) \\ \sin\theta_r & \sin(\theta_r + \frac{2\pi}{3}) & \sin(\theta_r - \frac{2\pi}{3}) \\ \frac{1}{2} & \frac{1}{2} & \frac{1}{2} \end{bmatrix}.$$

Hence applying equation (2.2), the V_{dqo} voltages are as follows

$$\begin{aligned} V_d &= r_s I_d + \frac{d\lambda_d}{dt} - \omega\lambda_q \\ V_q &= r_s I_q + \frac{d\lambda_q}{dt} + \omega\lambda_d \\ V_0 &= r_s I_0 + \frac{d\lambda_0}{dt} \end{aligned} \tag{2.3}$$

This thesis assumes skewed machines, so the effect of *dq* flux linkage variation with rotor position is assumed to be insignificant. Bearing in mind that the analysis in this thesis is based on steady state, and in the steady state the *d-axis* and the *q-axis* currents are pure dc quantities, so as such:

$$\frac{d\lambda_d}{dt} = \frac{\partial\lambda_d}{\partial I_d}\frac{dI_d}{dt} = 0$$
$$\frac{d\lambda_q}{dt} = \frac{\partial\lambda_q}{\partial I_q}\frac{dI_q}{dt} = 0$$

This then further simplifies equation (2.3) into the following steady-state voltage equations given as follows:

$$\begin{aligned} V_d &= r_s I_d - \omega\lambda_q \\ V_q &= r_s I_q + \omega\lambda_d \\ V_0 &= r_s I_0 \end{aligned} \tag{2.4}$$

Note that for a balanced 3-phase system, $V_0 = 0$, hence the steady state voltage equations are simplified to two *dq*-voltage equations. With the steady-state voltage equations, the *dq* equivalent circuit diagram of the 3-phase RSM can be developed as shown in Figure 2.1.

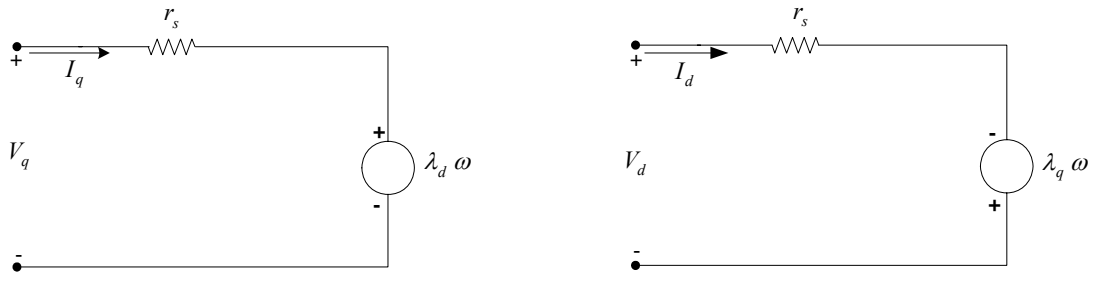

(a) (b)

Figure 2.1: (a) *d-axis* and (b) *q-axis* equivalent circuits of the 3-phase RSM

2.1.2 Torque equation

Based on the *dq* voltage equations of the 3-phase RSM, the torque equation of a *p* pole–pair machine as derived by Krause [1986] on *dq*-axis theory is

$$T = \frac{3}{2} p(\lambda_d I_q - \lambda_q I_d). \tag{2.5}$$

The *d-axis* flux linkage, λ_d, and the *q-axis* flux linkage, λ_q, can be expressed in the steady state as $\lambda_d = L_d I_d$ and $\lambda_q = L_q I_q$ respectively [Kamper (1995), Chiricozzi (1996)]. The torque equation can be defined in terms of the *d –axis* inductance, L_d, and *q-axis* inductance, L_q, as [Parasiliti (1995)]

$$T = \frac{3}{2} p(L_d - L_q) I_d I_q. \tag{2.6}$$

It is noticeable from equation (2.6) that the torque of a 3-phase RSM is a function of the product of the *dq-axis* inductance difference and the *dq-axis* currents.

2.1.3 Determination of the equivalent circuit parameters

As shown from the equivalent circuit diagram of Figure 2.1, the equivalent circuit parameters of interest are the phase resistance, r_s, the speed voltages, $\lambda_q\omega$ and $\lambda_d\omega$, *dq* currents (I_d and I_q) and the *dq* voltages (V_d and V_q). This section focuses on the determination of the above-mentioned equivalent circuit parameters.

(a) Phase resistance

The phase resistance, r_s, is determined from the active copper area at a temperature of, by convention, 75 ^{0}C. The active copper area is determined accurately by applying a fill factor to the slot dimensions. The slot insulation and the conductor insulation are taken into account. The skin effect is ignored in the calculation of r_s. The expression for calculating the phase resistance is given by [Kamper (1996)]

$$r_s = \frac{2 N \rho_t (l + l_e)}{n_a A_{cu}/z}, \tag{2.7}$$

where N is the number of turns in series per phase, l is the stack length of the machine, l_e is the average length of the coil end, A_{cu}/z is the active copper area of a stator conductor, n_a is number of parallel circuits and ρ_t is the resistivity of copper at a temperature t_c given by

$$\rho_t = \rho_{20}(1 + Y_t(t_c - 20)), \tag{2.8}$$

where $\rho_{20} = 17x10^{-9}\,\Omega m$ and $Y_t = 0.0039/^0C$.

(b) Calculation of the speed voltages

Speed voltages, as from the *dq* voltage equations of the 3-phase RSM are a product of flux linkage and the electrical rotor speed. The calculation of flux linkage is done by finite element analysis as explained in appendix A.2. The RSMs under consideration in this thesis are under current control, therefore in calculating the flux linkages of the 3-phase RSM, it is necessary to specify the phasor current, I_m, and the current angle, α, in the FE software. The amplitude of the phasor current, I_m, can be determined by two methods namely:

- From the given RMS current density, *J*, as

$$\mathbf{I_m} = \sqrt{2}\, J\, A_{cu}\, n_a / z\,. \tag{2.9}$$

- From the given copper losses, P_{cu}, as given by

$$\mathrm{I_m} = \sqrt{\frac{2P_{cu}}{3r_s}} = K\left(\frac{n_a}{z}\right)\sqrt{\frac{P_{cu}A_{cu}}{(l+l_e)}}\,, \tag{2.10}$$

$$\text{with } K = \left(\frac{1}{3\,q\,p\,\rho_t}\right)^{1/2}.$$

With the phasor current known from either equation (2.10) or (2.11) and the current angle, the *dq* current components can be calculated by the use of the phasor diagram of Figure 2.2.

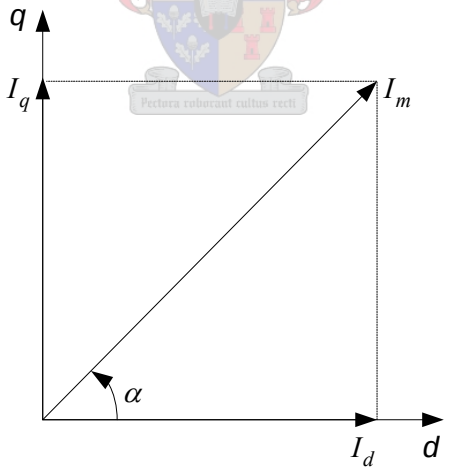

Figure 2.2: *dq*-current phasor diagram

The instantaneous 3-phase currents, i_{abc}, can be calculated using the inverse park transformation. Therefore the 3-phase winding currents are set in the FE program as a function of the rotor position. With the above-mentioned currents and the machine dimensions, the FE analysis method then calculates the total stator flux linkages, λ_{abc}, excluding the end winding flux linkage. But if the machine is skewed, no prominent high

frequency slot ripple will be present in the flux linkage waveform [Alhamadi (1991), Volschenk (1993), Williamson (1994)]. Skew is accounted for in the FE analysis by subdividing the machine axially into five sub-machines as will be shown in the next chapter. The sub-machines are displaced by an angle, which is a fraction of the total skew. With *k* (i.e. *k* is taken to be 5) unskewed machines, the phase flux linkages can be calculated by

$$[\lambda_{abc}] = \frac{1}{k}\left[\sum_{n=1}^{k} \lambda_{abc}(\theta_{rn})\right], \tag{2.11}$$

where $\lambda_{abc}(\theta_{rn})$ denotes the total phase flux linkages of the unskewed machine with the rotor at position θ_{rn}, and calculated by the FE method as by equation A.2. These total phase flux linkages do not only comprise of the fundamental components, they also comprises of a prominent 3rd and less prominent 5th and 7th harmonics. Ignoring the less prominent 5th and 7th harmonic flux linkages, the total flux linkage can be expressed in terms of the fundamental and the 3rd harmonic components as

$$[\lambda_{abc}] \approx [\lambda_{abc1}] + [\lambda_{abc3}], \tag{2.12}$$

whereby λ_{abc1} and λ_{abc3} are the fundamental and the third harmonic flux linkages respectively. The co-phasal 3rd harmonic flux linkages, including the high order triplen harmonics can be obtained from the actual 3-phase flux linkages as follows:

$$\lambda_{a3} = \lambda_{b3} = \lambda_{c3} \approx \frac{1}{3}(\lambda_a + \lambda_b + \lambda_c). \tag{2.13}$$

The aim of the whole above-mentioned exercise is to determine the fundamental total phase flux linkages as given in equation (2.14), with the actual total phase flux linkage and the 3rd harmonic flux linkages known from FE analysis.

$$[\lambda_{abc1}] \approx [\lambda_{abc}] - [\lambda_{abc3}] \tag{2.14}$$

The fundamental flux linkages are then transformed to the *dq* flux linkages, λ_{dq0}, by the use of Park's transformation such that the *dq* flux linkages are given by equation (2.15).

$$[\lambda_{dq0}] = [k_p][\lambda_{abc1}] \tag{2.15}$$

With the *dq* flux linkages known, the *dq* speed voltages can be determined by

$$e_d = -\lambda_q \omega \qquad \text{and} \qquad e_q = \lambda_d \omega \tag{2.16}$$

(c) Calculation of the dq voltages

With the phase resistance, the speed voltages and the *dq* currents known, the *dq* voltages can be determined by the use of equation (2.4).

2.2 Five - phase RSM

In this section, the machine model of the 5-phase RSM is defined in the *abcde*- reference frame and transformed to the *qdQDn* reference frame. Based on the steady state *dqQDn* voltage equations, the equivalent circuit diagrams and the torque equations are derived. The determination of the equivalent circuit parameters is also done in this section.

2.2.1 DQ equivalent circuits

Just like for the 3-phase RSM, the stator voltage in the *abcde* reference frame in matrix form is given by equation (2.17). It is assumed that iron saturation is neglected and that only fundamental air gap flux is taken into account.

$$\mathbf{V}_s = r_s \mathbf{I}_s + \frac{d\boldsymbol{\lambda}_s}{dt}, \tag{2.17}$$

with $\mathbf{V}_s = \begin{bmatrix} v_a \\ v_b \\ v_c \\ v_d \\ v_e \end{bmatrix}$, $\mathbf{I}_s = \begin{bmatrix} i_a \\ i_b \\ i_c \\ i_d \\ i_e \end{bmatrix}$ and $\boldsymbol{\lambda}_s = \begin{bmatrix} \lambda_a \\ \lambda_b \\ \lambda_c \\ \lambda_d \\ \lambda_e \end{bmatrix}$.

Equation (2.17) can be transformed to *qdQDn* voltage equations by the use of a transformation matrix, k_t as follows [Toliyat (2000)]

$$\left[V_{qdQDn}\right] = \left[k_t\right]\left[v_{abcde}\right], \tag{2.18}$$

where k_t is given by

$$k_t = \frac{2}{5}\begin{bmatrix} \cos\theta_r & \cos(\theta_r - \frac{2\pi}{5}) & \cos(\theta_r - \frac{4\pi}{5}) & \cos(\theta_r + \frac{4\pi}{5}) & \cos(\theta_r + \frac{2\pi}{5}) \\ \sin\theta_r & \sin(\theta_r - \frac{2\pi}{5}) & \sin(\theta_r - \frac{4\pi}{5}) & \sin(\theta_r + \frac{4\pi}{5}) & \sin(\theta_r + \frac{2\pi}{5}) \\ 1 & \cos\frac{2\pi}{5} & \cos\frac{4\pi}{5} & \cos\frac{4\pi}{5} & \cos\frac{2\pi}{5} \\ 0 & \sin\frac{2\pi}{5} & \sin\frac{4\pi}{5} & -\sin\frac{4\pi}{5} & -\sin\frac{2\pi}{5} \\ \frac{1}{\sqrt{2}} & \frac{1}{\sqrt{2}} & \frac{1}{\sqrt{2}} & \frac{1}{\sqrt{2}} & \frac{1}{\sqrt{2}} \end{bmatrix}.$$

The *qdQDn* voltages can then be expressed as

$$
\begin{aligned}
V_q &= r_s I_q + \omega\lambda_d + \frac{d\lambda_q}{dt} \\
V_d &= r_s I_d - \omega\lambda_q + \frac{d\lambda_d}{dt} \\
V_Q &= r_s I_Q + \frac{d\lambda_Q}{dt} \\
V_D &= r_s I_D + \frac{d\lambda_D}{dt} \\
V_n &= r_s I_n + \frac{d\lambda_n}{dt}
\end{aligned}
\tag{2.19}
$$

The above equation (2.19) can be further simplified to steady-state equations just like for the 3-phase RSM resulting into

$$
\begin{aligned}
V_q &= r_s I_q + \omega\lambda_d \\
V_d &= r_s I_d - \omega\lambda_q \\
V_Q &= r_s I_Q \\
V_D &= r_s I_D \\
V_n &= r_s I_n
\end{aligned}
\tag{2.20}
$$

Based on the steady state *qdQDn* voltage equation (2.20), the following equivalent circuit diagram of a 5-phase RSM can be derived as shown in Figure 2.3.

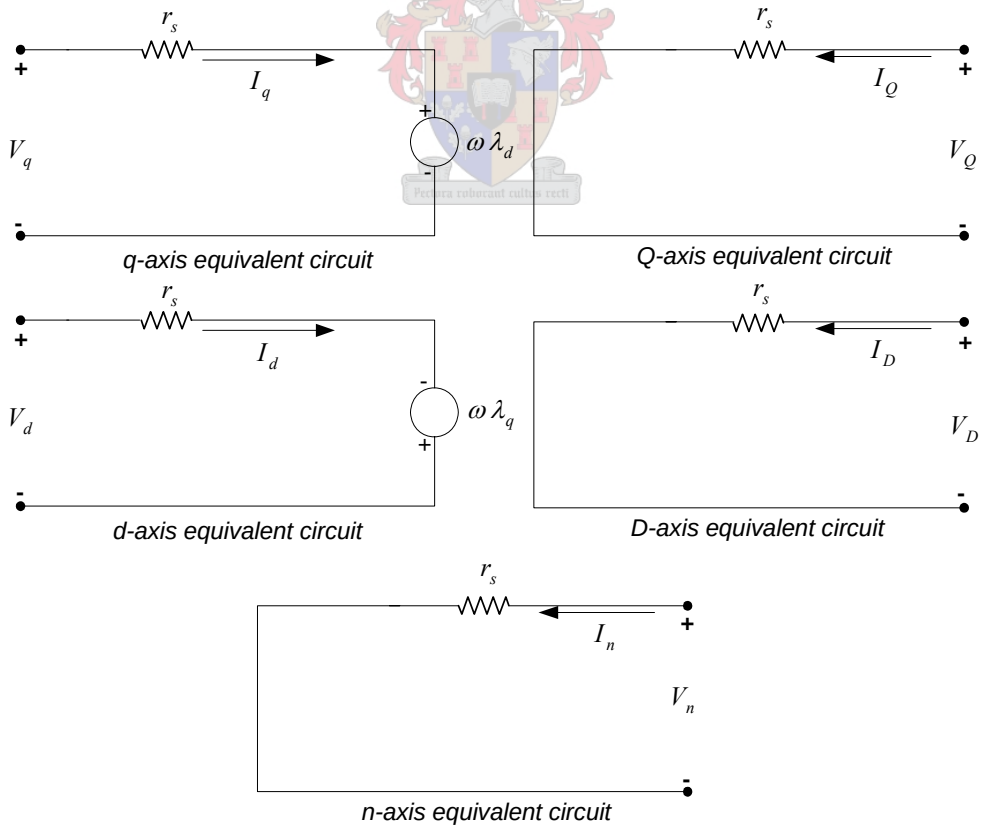

Figure 2.3: Equivalent circuits of 5-phase RSM

2.2.2 Torque equation

Based on the steady state voltage equation (2.20), the torque equation of the 5-phase RSM can be expressed as follows:

$$T = \frac{5}{2} p (\lambda_d I_q - \lambda_q I_d) \tag{2.21}$$

2.2.3 Determination of equivalent circuit parameters

As shown in the equivalent circuit of Figure 2.3, the equivalent circuit parameters are the same as those of the 3-phase RSM so the parameters of interest are the phase resistance, r_s, and the speed voltages $\lambda_q\omega$ and $\lambda_d\omega$. The same method used for determining the equivalent circuit parameters of the 3-phase RSM can then be applied to the 5-phase RSM. Note that the phase resistance can be determined by using equation (2.7), just like for the 3-phase RSM. For the determination of the speed voltages, the FE analysis method is used. For the FE method the amplitude of the phasor current, I_m, and the current angle, α, have to be known. The determination of the amplitude of the phasor current for the 5-phase RSM can be done by the use of the following equation.

$$\mathbf{I_m} = \sqrt{\frac{2P_{cu}}{5r_s}} \tag{2.22}$$

With the amplitude of the current phasor and the current angle, the instantaneous current values, i_{abcde}, of the 5-phase RSM can be determined. The instantaneous currents are then set according to rotor position in the finite element program. With the currents and the machine dimensions known, the finite element program calculates the total stator flux linkages λ_{abcde}. Note that for the 5-phase RSM, the 3rd harmonic flux linkage is ignored and the total flux linkage is assumed to comprise of the 5th harmonic flux linkage. So the total flux linkage can be expressed in terms of the fundamental and the 5th harmonic component as

$$[\lambda_{abcde}] \approx [\lambda_{abcde1}] + [\lambda_{abcde5}], \tag{2.23}$$

where λ_{abcde1} and λ_{abcde5} are the fundamental and the fifth harmonic flux linkages respectively. The co-phasal 5th harmonic flux linkages can be obtained from the actual 5-phase flux linkages as

$$\lambda_{a5} = \lambda_{b5} = \lambda_{c5} = \lambda_{d5} = \lambda_{e5} \approx \frac{1}{5}(\lambda_a + \lambda_b + \lambda_c + \lambda_d + \lambda_e). \tag{2.24}$$

Hence the fundamental total phase flux linkage can approximately be calculated as

$$[\lambda_{abcde1}] \approx [\lambda_{abcde}] - [\lambda_{abcde5}]. \tag{2.25}$$

The fundamental phase flux linkages can be transformed to *dqDQn* flux linkages by the use of the transformation matrix (k_t) of equation (2.18) as

$$\lfloor \lambda_{qdQDn} \rfloor = [k_t][\lambda_{abcde1}] \tag{2.26}$$

But it should be noted that under balanced conditions $\lambda_{QDn} = 0$ as such the fundamental phase flux linkages are transformed to *dq* flux linkages (λ_{qd}). From the *dq* flux linkages, the speed voltages can be calculated by using equation (2.16).

2.3 Five - Phase + 3 rd harmonic RSM

In this section, the machine model of the 5-phase + 3rd RSM is defined in the *q1d1q3d3* reference frame. Based on the steady state voltage equations, the equivalent circuit diagrams and the torque equations are presented. The determination of the equivalent circuit parameters of the machine is also presented. According to the research publications on this type of machine, maximum torque is obtained if the 3rd harmonic current is 33% of the fundamental [Xu (2000)].

2.3.1 dq Equivalent circuits

The same voltage equation as for the previous machines is used as given in equation (2.17); the difference is in the transformation matrix as proposed by Toliyat (1998). The transformation of 5-phase with the injection of 3rd voltages to *qd* voltages is given by

$$\lfloor V_{q1-d1-q3-d3-n} \rfloor = [k_{t3}][v_{abcde}], \tag{2.27}$$

where

$$k_{t3} = \frac{2}{5}\begin{bmatrix} \cos\theta_r & \cos(\theta_r - \frac{2\pi}{5}) & \cos(\theta_r - \frac{4\pi}{5}) & \cos(\theta_r + \frac{4\pi}{5}) & \cos(\theta_r + \frac{2\pi}{5}) \\ \sin\theta_r & \sin(\theta_r - \frac{2\pi}{5}) & \sin(\theta_r - \frac{4\pi}{5}) & \sin(\theta_r + \frac{4\pi}{5}) & \sin(\theta_r + \frac{2\pi}{5}) \\ \cos 3\theta_r & \cos 3(\theta_r - \frac{2\pi}{5}) & \cos 3(\theta_r - \frac{4\pi}{5}) & \cos 3(\theta_r + \frac{4\pi}{5}) & \cos 3(\theta_r + \frac{2\pi}{5}) \\ \sin 3\theta_r & \sin 3(\theta_r - \frac{2\pi}{5}) & \sin 3(\theta_r - \frac{4\pi}{5}) & \sin 3(\theta_r + \frac{4\pi}{5}) & \sin 3(\theta_r + \frac{2\pi}{5}) \\ \frac{1}{\sqrt{2}} & \frac{1}{\sqrt{2}} & \frac{1}{\sqrt{2}} & \frac{1}{\sqrt{2}} & \frac{1}{\sqrt{2}} \end{bmatrix}.$$

From this the following *qd* – voltage equations are obtained

$$
\begin{aligned}
V_{q1} &= r_s I_{q1} + \omega\lambda_{d1} + \frac{d\lambda_{q1}}{dt} \\
V_{d1} &= r_s I_{d1} - \omega\lambda_{q1} + \frac{d\lambda_{d1}}{dt} \\
V_{q3} &= r_s I_{q3} + 3\omega\lambda_{d3} + \frac{d\lambda_{q3}}{dt} \\
V_{d3} &= r_s I_{d3} - 3\omega\lambda_{q3} + \frac{d\lambda_{d3}}{dt} \\
V_n &= r_s I_n + \frac{d\lambda_n}{dt}
\end{aligned}
\tag{2.28}
$$

It can be observed from equation (2.28) that the 5-phase with an injection of 3rd harmonic voltages are transformed into fundamental and third harmonic *qd* voltages respectively. Voltage equations (2.29) can further be simplified to steady state equations as follows:

$$
\begin{aligned}
V_{q1} &= r_s I_{q1} + \omega\lambda_{d1} \\
V_{d1} &= r_s I_{d1} - \omega\lambda_{q1} \\
V_{q3} &= r_s I_{q3} + 3\omega\lambda_{d3} \\
V_{d3} &= r_s I_{d3} - 3\omega\lambda_{q3} \\
V_n &= r_s I_n
\end{aligned}
\tag{2.29}
$$

From the steady state *qd* voltage equations of the 5-phase + 3rd harmonic RSM, the following *qd* equivalent circuit diagrams can be derived as shown in Figure 2.4.

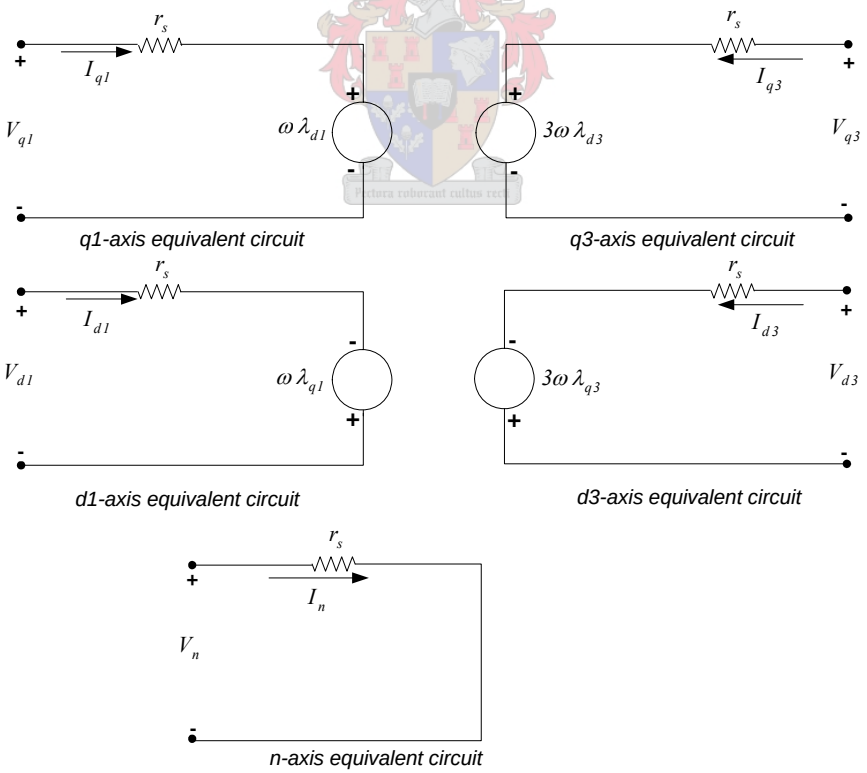

Figure 2.4: Equivalent circuits for the 5-phase + 3rd RSM

2.3.2 Torque equation

Based on the steady state voltage equation (2.29), the torque equation of the 5-phase + 3rd RSM can be expressed as follows

$$T = \frac{5}{2} p\{(\lambda_{d1} I_{q1} - \lambda_{q1} I_{d1}) + 3(\lambda_{d3} I_{q3} - \lambda_{q3} I_{d3})\}. \tag{2.30}$$

where $\lambda_{d1}, \lambda_{q1}, \lambda_{d3}$ and λ_{q3} are the fundamental *dq* flux linkages and the third harmonic *dq* flux linkages respectively. The torque equation of the 5-phase + 3rd RSM unlike for the 3-phase and 5-phase RSMs is made up of two components namely: torque due to the fundamental component and the one due to the third harmonic component.

2.3.3 Determination of the equivalent circuit parameters

The determination of the equivalent circuit parameters of the 5-phase + 3rd RSM involves the determination of the parameters for both the fundamental and the third harmonic circuits. The determination of the parameters is done by the use of finite element analysis.

The phase resistance, r_s, is the same for all the equivalent circuits and is calculated by using equation (2.7). The determination of the fundamental and third harmonic *dq* flux linkages for the 5 + 3rd RSM is determined separately by superposition. The fundamental *dq* flux linkages are determined by applying the 5-phase sinusoidal currents without the third harmonic currents and the third harmonic *dq* flux linkages are determined likewise by applying only the third harmonic currents.

With the 5-phase sinusoidal currents, the amplitude of the current phasor is as given in equation (2.22) and the fundamental phase flux linkages can be determined in the same way as for the 5-phase RSM. With the fundamental phase flux linkages, the fundamental *dq* flux linkages can be calculated as follows:

$$\left[\lambda_{q1-d1-q3-d3-n}\right] = \left[k_{t3}\right]\left[\lambda_{abcde1}\right] \tag{2.31}$$

In the determination of the fundamental flux linkages, λ_{q1-d1}, from equation (2.31) the 3rd harmonic *dq* flux linkages, λ_{q3-d3}, are ignored. The same format is applied in determining the 3rd harmonic phase flux linkages by applying only 3rd harmonic phase currents. The amplitude of the current phasor with 3rd harmonic currents only, I_{m3}, is taken to be 33% of the fundamental as given by

$$I_{m3} = 0.33 I_m \tag{2.32}$$

With the amplitude of the current phasor and the current angle, the finite element analysis calculates 3rd harmonic phase flux linkages. In this particular case, the 3rd harmonic phase flux linkages are taken as the instantaneous phase flux linkages, λ_{abcde}. The 3rd harmonic phase flux linkages are then transformed to 3rd harmonic *dq* flux linkages as follows:

$$\left[\lambda_{q1-d1-q3-d3-n}\right]=\left[k_{t3}\right]\left[\lambda_{abcde}\right] \tag{2.33}$$

In determining the 3rd harmonic *dq* flux linkages, λ_{q3-d3}, from equation (2.33), the fundamental *dq* flux linkages are ignored. The 3rd harmonic *dq* currents are calculated as

$$I_{q3} = \mathrm{I}_{\mathrm{m3}} \sin(3\alpha) \qquad ; \qquad I_{d3} = \mathrm{I}_{\mathrm{m3}} \cos(3\alpha) \tag{2.34}$$

With the fundamental and the 3rd *dq* flux linkages, the speed voltages can then be determined as

$$\begin{aligned} e_{d1} &= -\lambda_{d1}\omega \\ e_{q1} &= \lambda_{q1}\omega \\ e_{d3} &= -\lambda_{d3}\omega \\ e_{q3} &= \lambda_{q3}\omega \end{aligned} \tag{2.35}$$

2.4 Summary

In this chapter the steady state *dq* voltage equations of the 3-phase, 5-phase and 5-phase RSMs with the injection of third harmonic current were developed, and it was realised that the torque equations of the first two machines are similar. The torque equations of the 3-phase and 5-phase RSMs amongst other things are functions of the *dq* flux linkages. For the 5-phase RSM with the injection of third harmonic current, the torque equation is made up of two components, the fundamental torque component (similar to the above 3-phase & 5-phase RSMs) and the third harmonic torque component. The FE method of determining the *dq* flux linkages of the machines is developed, more especially the one for the 5-phase +3rd RSM. The torque equations and the method for determining the equivalent circuit parameters, more especially the flux linkages will be used in chapter 3 to calculate the torque performances of the machines.

Pectora roborant cultus recti

CHAPTER 3 Torque Performance of Sinusoidal RSMs

The chapter's main goal is to carry out a comparative study of the so-called sinusoidal RSMs with two rotor structures. The purpose of the study is to facilitate the selection of the rotor structure for the RDCM and as such acts as a base for the evaluation of the torque performance of the RDCMs. The 5-phase RSM with the addition of third harmonic phase currents is referred to in this thesis as simply 5-phase + 3rd RSM. The torque performances of the above-mentioned sinusoidal optimum RSMs are determined by the use of finite element analysis. The machines are analysed with two rotor structures but with same stator structure: the rotor structures studied are the round rotor with internal barriers and a salient pole rotor with no internal barriers. The machines studied are for only one volumetric size (40 – 50 kW) for comparison purposes. The design optimisation of the machines, more especially the Powell optimisation algorithm is described in detail in this chapter. With the optimised sinusoidal RSMs, the FE torque performances of the machines are compared so as to get a true comparison of the torque performance of the machines. The steady state torque performances of the sinusoidal RSMs are also calculated based on the steady state torque equations from chapter 2. As a further step in verifying the FE torque results, the optimum 3-phase sinusoidal RSM with an FBR – rotor was built and tested and the measured results in comparison with the FE results are presented in this chapter.

3.1 Three Phase RSM

The section focuses on the stator and rotor structures for the three-phase RSM under investigation. The investigation is focussed on a normal (transverse) laminated stator and rotor configurations. This type of structure was chosen rather than the axially laminated structure due to its simple construction and the fact that the rotor can be skewed [El-Antably (1985), Matsuo (1994), Kamper (1994), Conti (1996)]. The normal (transverse) laminated rotor has no iron loss problem associated with axially laminated rotors [Vagati (2000)]. The formulation of the three phase current waveforms is also described in the chapter.

3.1.1 Stator

The stator of the RSM under investigation consists of a conventional cylindrical structure. It has three phases distributed, full pitch windings with wye connection. Note that distributed winding(s) refers to a winding whereby one phase occupies more than one slot. For the three phase RSM under investigation, the three phase windings are placed in space in the following sequence ***A, A, A, A, -B, -B, -B, -B, C, C, C, C*** from left to right. It should also be noted that

the three-phase machine under investigation is a 4 pole, 24 slots machine but only a quarter of the machine is modelled as shown in Figure 3.1.

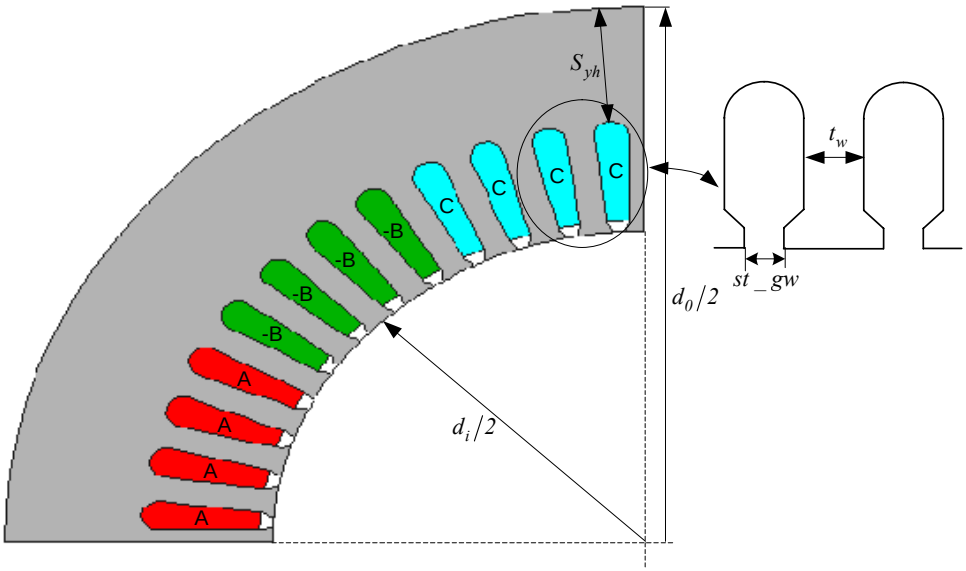

Figure 3.1: Stator configuration (quarter section) of the 3-phase RSM.

The important dimensions of the stator (shown in Figure 3.1) to be optimised, are the tooth width, t_w, stator yoke height, s_{yh}, stator inner diameter, d_i, and the stator outer diameter, d_o. The other thing that can be noticed from the figure is that the construction of the stator is of the open slot configuration so the slot has an opening to the air gap (slot gap width, *st_gw*) that contributes to the flux pulsations in the air gap. The slot gap width is kept constant at 1.88 millimetres in the investigation.

3.1.2 Rotor structures

For the study, two rotor structures were investigated, the round rotor with internal flux barriers (FBR – rotor) and the salient pole rotor with no internal barriers but only cut outs (CR – rotor). The reason for using the two rotor structures for the investigation is to carry out a comparison study that can be used further in the thesis to select a suitable rotor structure from the two for the reluctance DC machines. The two rotors were investigated with the same stator (the above mentioned stator). The two rotor structures are shown in Figures 3.2(a) and 3.2(b) respectively. Just like for the stator part, only a quarter of the rotor part is shown with their corresponding dimensions.

The different dimensions defining the rotor structures, which have to be optimised in the design optimisation, are also shown in Figures 3.2(a) and (b) and are rotor outer diameter, d_r,

shaft diameter, d_{sh}, four barriers widths, b_1, b_2, b_3, b_4, rotor cut-out angle, σ, and the rotor cut-out depth, r_c.

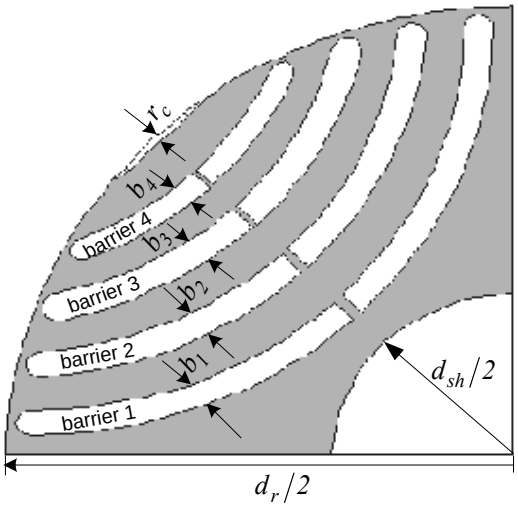

Figure 3.2(a): Structure (quarter section) of the 4-pole FBR-rotor

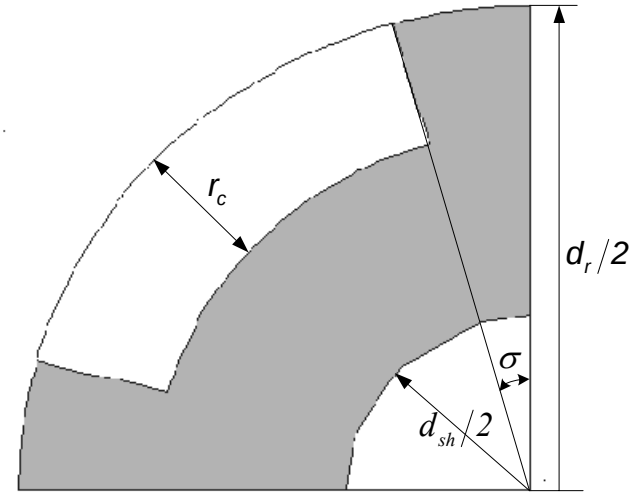

Figure 3.2(b): Structure (quarter section) of the 4-pole CR-rotor

3.1.3 Current Waveforms

Referring to the appendix A on FE, the FE input parameters are the machine dimensions (stator and rotor dimensions) and the currents, since a current regulated PWM voltage source inverter (VSI) is assumed to provide the current waveforms. Note that the investigation of the 3-phase RSM is based on sinusoidal current waveforms so the equations of the stator 3-phase sinusoidal current waveforms are given as

$$
\begin{aligned}
i_a &= \mathrm{I_m}\sin(\theta_r + \alpha) \\
i_b &= \mathrm{I_m}\sin(\theta_r + \alpha - \frac{2\pi}{3}) \\
i_c &= \mathrm{I_m}\sin(\theta_r + \alpha + \frac{2\pi}{3})
\end{aligned}
\tag{3.1}
$$

In the equation, θ_r is the rotor position in electrical degrees measured from the phase *a* magnetic axis to the rotor's q-axis, α is the current angle and $\mathrm{I_m}$ is the amplitude of the current phasor. As mentioned from the previous chapter, with the current phasor and the current angle known, the *dq* currents can then be calculated.

3.2 Five - phase RSM

The same stator and rotor configurations as for the 3-phase RSMs were used for the 5- phase RSMs. But for the 5-phase RSM, two stator types were used, distributed winding and the concentrated winding. The reason for using two stator configurations for the 5-phase machines is that, unlike for the 3-phase machines, where it is common knowledge that the more the slots the less the ripple, this investigation is to re-affirm the logic for multi-phase machines. For the distributed winding, the 5 phase windings are placed in space in the following sequence ***A, A, -C, -C, E, E, -B, -B, D, D*** from left to right. For the distributed winding a 40 slot, 4-pole machine was modelled. The stator with distributed windings is as shown in Figure 3.3(a). While for the concentrated winding a 20 slot machine was modelled, and the 5 phase windings are placed in space in the following sequence ***A, -C, E, -B, D*** from left to right. The stator with concentrated windings is as shown in Figure 3.3(b).

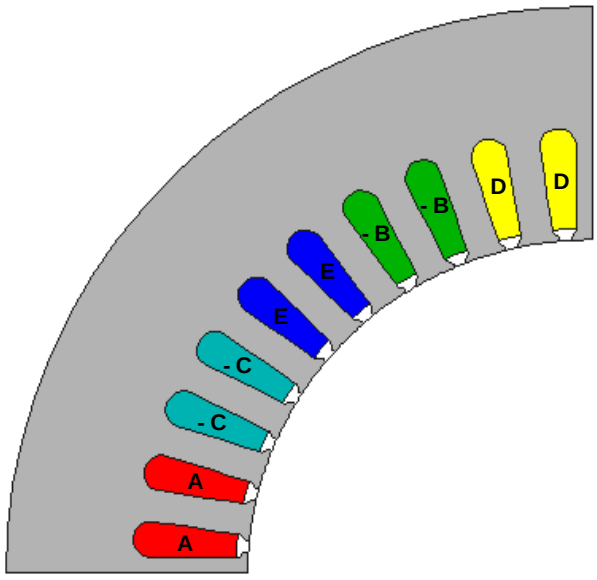

Figure 3.3(a): Stator configuration (quarter section) of the 5-phase RSM with distributed winding

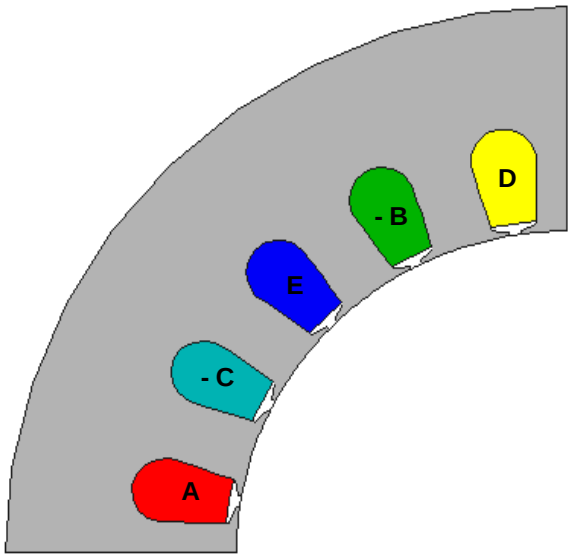

Figure 3.3(b): Stator configuration (quarter section) of the 5-phase RSM with concentrated winding

The stator 5-phase sinusoidal currents as a function of position and current angle are given as follows:

$$\begin{aligned} i_a &= \mathrm{I_m}\sin(\theta_r + \alpha) \\ i_b &= \mathrm{I_m}\sin(\theta_r + \alpha - \frac{2\pi}{5}) \\ i_c &= \mathrm{I_m}\sin(\theta_r + \alpha - \frac{4\pi}{5}) \\ i_d &= \mathrm{I_m}\sin(\theta_r + \alpha + \frac{4\pi}{5}) \\ i_e &= \mathrm{I_m}\sin(\theta_r + \alpha + \frac{2\pi}{5}) \end{aligned} \tag{3.2}$$

The current distribution for the sinusoidal currents with an assumption of a 45^0 current angle is as shown in Figure 3.3(c). From the Figure, it can be observed that the current is sinusoidally distributed in the slots.

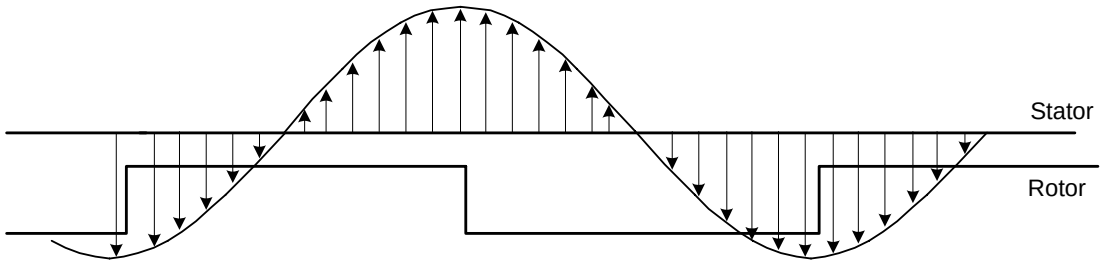

Figure 3.3(c): Current distribution with respect to rotor position of the RSM with the CR-rotor with sinusoidal currents.

3.3 Five-phase plus third harmonic current RSM

The study of the so-called 5-phase plus third harmonic current RSM was with the same stator and rotor structures as for the 5-phase without third harmonic currents. As mentioned in the previous chapter, for optimum performance, the third harmonic current is 33% of the fundamental current [Toliyat (1992)]. So 5-phase stator currents with the addition of 33% third harmonic current are as follows:

$$\begin{aligned}
i_a &= \mathrm{I_m}[\sin(\theta_r + \alpha) + 0.33\sin 3\theta_r] \\
i_b &= \mathrm{I_m}[\sin(\theta_r + \alpha - \frac{2\pi}{5}) + 0.33\sin 3(\theta_r + \alpha - \frac{2\pi}{5})] \\
i_c &= \mathrm{I_m}[\sin(\theta_r + \alpha - \frac{4\pi}{5}) + 0.33\sin 3(\theta_r + \alpha - \frac{4\pi}{5})] \\
i_d &= \mathrm{I_m}[\sin(\theta_r + \alpha + \frac{4\pi}{5}) + 0.33\sin 3(\theta_r + \alpha + \frac{4\pi}{5})] \\
i_e &= \mathrm{I_m}[\sin(\theta_r + \alpha + \frac{2\pi}{5}) + 0.33\sin 3(\theta_r + \alpha + \frac{2\pi}{5})]
\end{aligned} \tag{3.3}$$

It has been found by previous researchers [Toliyat (1992), Xu (2000)] that adding proper 3rd harmonic current to the fundamental component to reshape the spatial MMF results in an increased torque per ampere ratio. On the other hand, the existence of 3rd harmonic magnetic field and current may seriously distort the back EMF. However this study is more focussed on the torque performance of the machine, so the investigation is not extended to the back EMF waveform.

With the addition of 33% 3rd harmonic current, the current distribution with the same assumption as above (i.e. current angle of 45 degrees) is as shown in Figure 3.4. It can be observed from the figure that unlike for the sinusoidal case, the current distribution is non-sinusoidal, that is, sinusoidal with an injection of third harmonic.

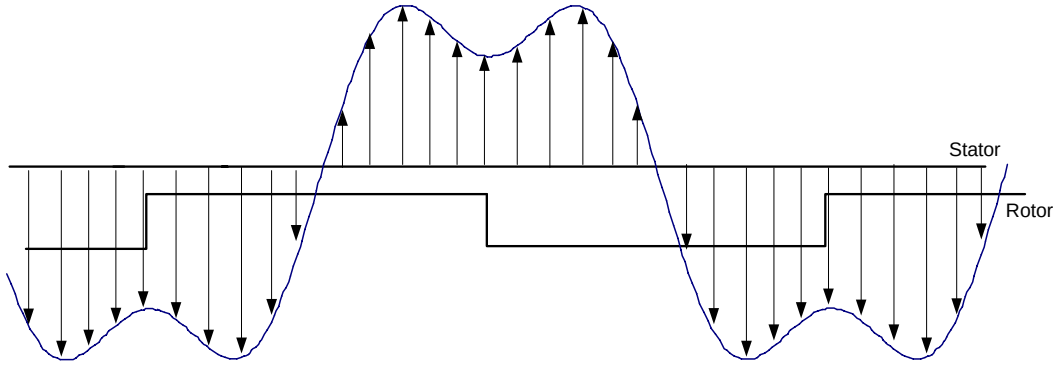

Figure 3.4: Current distribution with respect to rotor position of the RSM with sinusoidal plus an addition of 33% 3rd harmonic currents.

3.4 Design optimisation

The section covers the overall design optimisation of the 3-phase RSMs, 5-phase RSMs and 5-phase + 3rd RSMs. The aim of the optimisation procedure is to maximise, without any constraints, the torque per copper losses of the above-mentioned machines. The work of some of the authors on the design optimisation of electric machines can be summarised as follows:

- Andersen (1967, 1992) made use of the Monte Carlo routine to minimise the objective function with penalty functions.
- Ramamoorty (1979) made use of the Powell method (1964) for the design optimisation of the segmental rotor reluctance machine. In the design optimisation of the machine the cost of the active materials of the motor is minimised subject to the constraints of pull out torque and power factor.
- Li (1990) and Parasiliti (1993) made use of the modified Hooke – Jeves method [Hooke (1961)] for the design optimisation of an induction machine.
- Singh (1992) made use of Schittkowski (1981) method for the design optimisation of the induction motor.
- Kamper (1996) made use of the Powell method (1964) and the quasi-Newton method for the design optimisation of a cageless flux barrier rotor RSM.

In this thesis, Powell's algorithm is used for the overall designed optimisation of the machines. The aim of the design optimisation is to maximise without any constraints the torque per copper losses per given stack volume of the sinusoidal RSMs. The objective function for the unconstrained optimisation problem can simply be written as

$$Y = \mathbf{F}(\mathbf{X}) = T(\mathbf{X}) \tag{3.4}$$

where **X** is a matrix vector representing the machine dimensions and other variables to be optimised, $T(\mathrm{X})$ is the torque objective function to be optimised and Y is the output function value. The optimisation algorithm, thus, finds the multidimensional vector **X** that minimises Y of equation (3.4). The effect of iron losses was not taken into account in the design optimisation of the machines as the accurate calculation of these losses needs further in-depth study, especially for machines with an injection of third harmonic current.

The optimisation procedure for optimising the design of the RSMs can be best explained by the use of the flow chart of Figure 3.5. Using the FE solution, the optimisation algorithm (Powell's method), assigns values to the machine variables, X, that maximise the performance, Y, of the machine. Note that with each iteration r, the optimisation algorithm determines directions of search in multi dimensional along which y (torque) is maximised. The optimisation algorithm is linked with the FE program in such a way that each time the optimisation algorithm requires the output, Y, for a given input, X, it calls the FE program.

The FE program then generates a new mesh according to the changed inputs (it must be mentioned that the meshes were checked for ill shaped triangles). The program then does the pre-processing and the non-linear solution to determine the magnetic vector potentials. From this the FE program calculates the flux linkages and the torque. Due allowance is made for saturation by using the correct B-H curve of the machine steel in the FE program [Kamper (1994)]. The FE program can be called more than once by the algorithm. At the end of each iteration a test is carried out to determine if the maximum is reached; if not the next iteration is executed. Therefore, optimisation can be a time consuming process especially if the number of variables to be optimised are many.

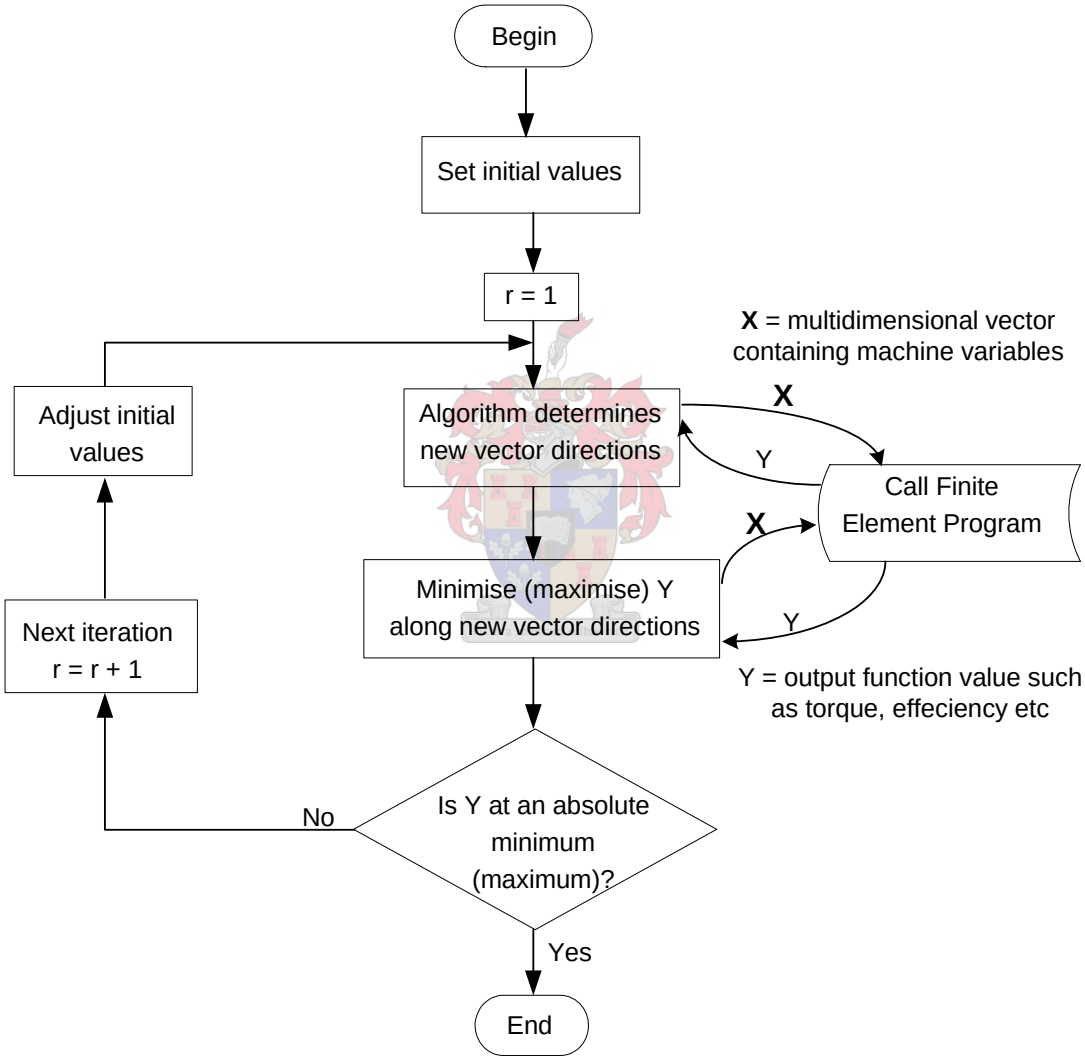

Fig 3.5: Optimisation procedure using FE method [Kamper (1996)]

To be able to compare the different machines under the same copper losses, P_{cu}, the stator phase currents will then have to be expressed as a function of copper losses. The amplitude of the phasor current, I_m, in equations (3.1) – (3.3) can be expressed in terms of copper losses as discussed from the previous chapter as follows:

$$I_m(3-\text{phase}) = \sqrt{\frac{2P_{cu}}{3r_s}} \tag{3.5}$$

$$I_m(5-\text{phase}) = \sqrt{\frac{2P_{cu}}{5r_s}} \tag{3.6}$$

$$I_m(5-\text{phase}+3^{\text{rd}}) = \sqrt{\frac{1.8P_{cu}}{5r_s}} \tag{3.7}$$

Rerunning the optimisation with different initial values and checking if it still converged to the same optimum values, verified the design optimisation. There was no problem of local maxima (or minima) in the optimisation process as the objective functions versus the optimisation variables are very smooth curves with clear maximas. Furthermore, the design optimisation for the 3-phase RSMs, was performed by using two optimisation methods namely Powell and the Quasi-Newton method (which is a gradient method), and the results were the same.

The machines are optimised at 2.5 per unit load, which corresponds to a copper loss of 13.5 kW for the machines investigated. The reason for the latter is that a better overall torque performance is obtained (i.e. for all loads better than optimising at e.g. 1.0. per unit load).

3.4.1 Skew

The design optimisation is done for skewed machines only. The effect of skew on the torque of the machine is accounted for in the 2D FE analysis by dividing the machine axially into five sub-machines as shown in Figure 3.6. The sub-machines are displaced by the angle ϕ and the skewing is done over a slot-pitch angle β. The torque of the skewed machine is calculated by taking the average of the torque of the five sub-machines; this requires five FE field solutions so it can take a longer time [Kamper (1996)].

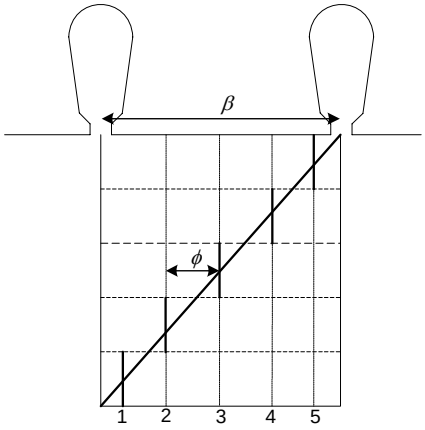

Figure 3.6: Representation of a skewed machine

The average fundamental torque for the skewed machines, T_{skew}, is given by the following equation.

$$T_{skew} = \frac{1}{k}\sum_{n=1}^{k} T_n \tag{3.8}$$

Based on FE used in this study, the torque of the sub-machines, T_n, is calculated as a function of the radial and tangential components of the airgap flux density by the Maxwell stress tensor method. The Maxwell stress tensor method is described in appendix A.4. From a computational perspective, the FE torque calculation method requires the local flux density distribution along a specific contour in the airgap of the machine.

3.4.2 Variables to be optimised

The optimisation was carried out on all the machines mentioned in the previous sections; the RSMs are as follows:

- 3 phase RSM with the CR-rotor and the distributed winding stator
- 3 phase RSM with the FBR-rotor and the distributed winding stator
- 5 phase RSM with the CR-rotor and the distributed winding stator
- 5 phase RSM with the FBR-rotor and the distributed winding stator
- 5 phase RSM with the CR-rotor and the concentrated winding stator
- 5 phase RSM with the FRR-rotor and the concentrated winding stator
- 5 phase RSM + 3rd harmonic currents with the CR-rotor and the distributed winding stator
- 5 phase RSM + 3rd harmonic currents with the FBR-rotor and the distributed winding stator
- 5 phase RSM + 3rd harmonic currents with the CR-rotor and the concentrated winding stator
- 5 phase RSM + 3rd harmonic currents with the FBR-rotor and the concentrated winding stator

For all the above-mentioned RSMs, the optimisation was carried out in the same way, i.e., the same variables were optimised for the machines with the same rotor structure. In the design optimisation, the shaft diameter, d_{sh}, is kept constant and the rotor outer diameter, d_r, is varied with the stator inner diameter, d_i, as the airgap is kept constant. The RSM parameters that are kept constant in the design optimisation are given in Table 3.1.

Table 3.1: Machine constants

Peak copper losses (kW)	13.5
Rated copper losses (kW)	2
Rated speed (r/min)	1500
Number of poles	4
Stack length (mm)	175
Stator outer diameter (mm)	340
Shaft diameter, d_{sh} (mm)	70
Airgap length (mm)	62

For the RSMs with the CR-rotor, six variables were optimised (refer to the Figures 3.1 and 3.2(b)) namely; tooth width, t_w, stator yoke height, s_{yh}, stator inner diameter, d_i, rotor cut-out depth, r_c, rotor cut-out angle, σ, and the current angle, α. For the RSMs with the FBR-rotor (refer to Figures 3.2(a)), nine variables were optimised namely; four rotor barrier widths, b_1, b_2, b_3, b_4, rotor cut-out depth, r_c, and the same stator variables as for the RSMs with the CR-rotor namely t_w, s_{yh}, d_i and α.

3.4.3 Optimisation results

The optimum dimensions of the different RSMs are given in Table 3.2. Note from Table 3.2 that for the 3-phase RSMs only the optimum dimensions of the machines with distributed stator windings are given. For the 5-phase RSMs the optimum dimensions are given for both the distributed and the concentrated stator winding machines.

Table 3.2: Optimisation results

Optimised 3-phase RSM (distributed)			
FBR-rotor		CR-rotor	
b_1 (mm)	5.8	σ (°)	16.3°
b_2 (mm)	6.5	r_c (mm)	24.8
b_3 (mm)	4.8	t_w (mm)	6.7
b_4 (mm)	4.1	s_{yh} (mm)	33.5
r_c (mm)	2.9	d_i (mm)	192.0
t_w (mm)	7.6	α (°)	54.9
s_{yh} (mm)	36.2		
d_i (mm)	199.0		
α (°)	68.0		

Optimised 5-phase RSM (distributed | concentrated.)			
FBR-rotor		CR-rotor	
b_1 (mm)	4.4 | 4.9	σ (°)	15.9° | 15.7°
b_2 (mm)	7.0 | 6.2	r_c (mm)	25.1 | 25.3
b_3 (mm)	6.1 | 5.7	t_w (mm)	8.1 | 17.1
b_4 (mm)	4.1 | 5.0	s_{yh} (mm)	33.5 | 32.8
r_c (mm)	2.2 | 1.7	d_i (mm)	193.5 | 194.5
t_w (mm)	9.4 | 18.8	α (°)	55.3 | 54.8
s_{yh} (mm)	36.4 | 36.7		
d_i (mm)	199.9 | 200.1		
α (°)	67.5 | 61.2		

Optimised 5-phase + 3rd RSM (distributed | concentrated)			
FBR-rotor		CR-rotor	
b_1 (mm)	5.3 | 5.1	σ (°)	15.6 | 15.7
b_2 (mm)	6.1 | 5.1	r_c (mm)	25.1 | 25.3
b_3 (mm)	5.0 | 6.0	t_w (mm)	8.2 | 17.1
b_4 (mm)	5.5 | 5.9	s_{yh} (mm)	32.9 | 32.8
r_c (mm)	4.2 | 3.0	d_i (mm)	194.3 | 194.5
t_w (mm)	9.3 | 18.9	α (°)	56.7 | 54.8
s_{yh} (mm)	36.1 | 36.3		
d_i (mm)	199.6 | 200.4		
α (°)	69.0 | 61.9		

Noticeable from Table 3.2 is the difference in d_i, α and s_{yh} between the FBR and the CR-rotor RSMs. In general terms, to achieve maximum torque, it is necessary for the d-axis reactance to be made as large as possible while the q-axis reactance is made as small as possible. The optimum conditions for this occur when the salient pole arc is very small, for instance, for the optimum 5-phase + 3rd RSM, the ratio of the pole arc to the pole pitch is 0.35 as opposed to 0.2 as mentioned by Lawrenson (1964). For the CR-rotor RSM, the cross coupling effect of the machine is severe, which explains the smaller current angle, α, and the narrow pole arc θ.

3.5 Cross – coupling effect

The torque of the RSM is a function of the *d-* and *q-axis* flux linkages. It is therefore important to consider the effects of saturation and cross-magnetisation on these flux linkages. Cross-coupling effect as defined by Kamper (1996) is the magnetic coupling between the fictitious *d-* and *q-axis* windings of the machine. There are various publications on the cross-coupling effect of reluctance machines with rotor cage windings without rotor flux barriers [Anvari (1985), Binder (1989)]. For the axially laminated rotors, it has been found from the various publications [Xu (1991), Mayer (1986), Matsuo (1994)] that the cross-magnetisation between the d and q-axis is negligible.

In this thesis, the cross coupling effect of the optimum 3-phase machines, both the one with the CR-rotor and the other one with the FBR-rotor, are shown in Figures 3.6(a) – 3.6(d). It is clear from the figures that saturation and specifically cross magnetisation have a considerable effect on the flux linkages of both the CR-rotor RSM and the FBR-rotor RSM. The *d-axis* flux linkage is affected minimally as compared to the *q-axis* flux linkages for the above-mentioned RSMs. In comparing the two RSMs, it can be concluded from the cross-magnetisation graphs that the CR-rotor RSM is more affected by the cross-magnetisation effect than the FBR-rotor RSM.

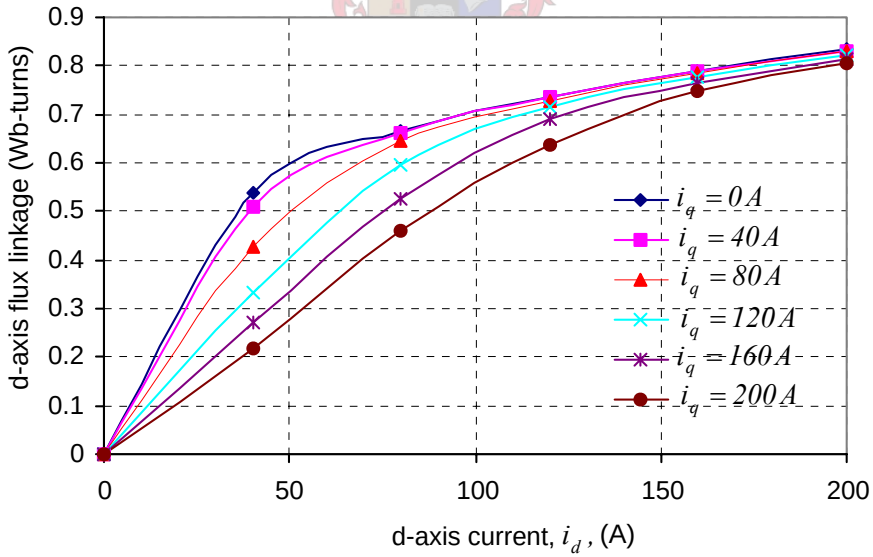

Figure 3.6(a): d-axis flux linkage versus i_d with i_q as a parameter of optimum CR-rotor RSM.

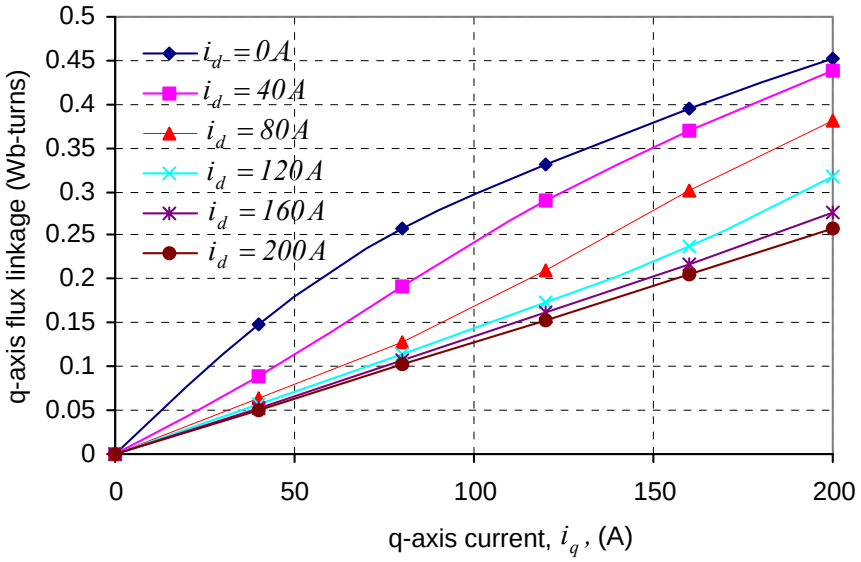

Figure 3.6(b): q-axis flux linkage versus i_q with i_d as a parameter of optimum CR-rotor RSM.

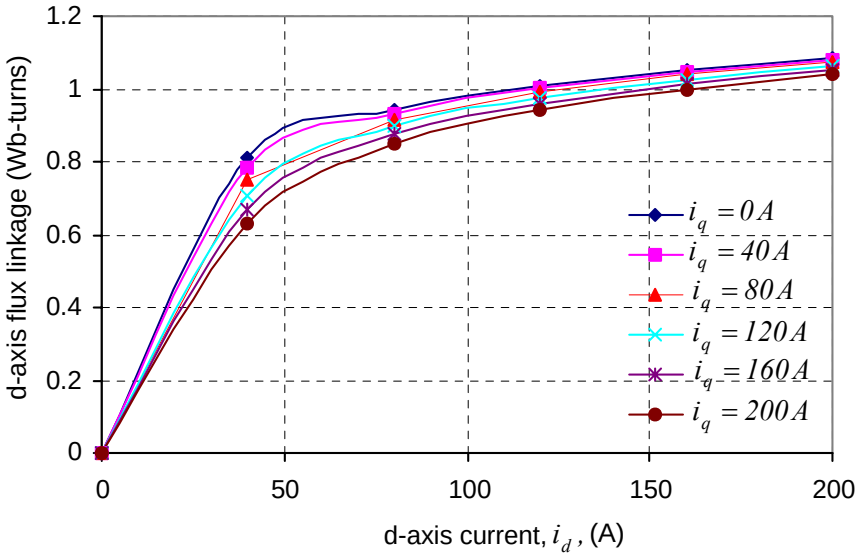

Figure 3.6(c): d-axis flux linkage versus i_d with i_q as a parameter of optimum FBR-rotor RSM.

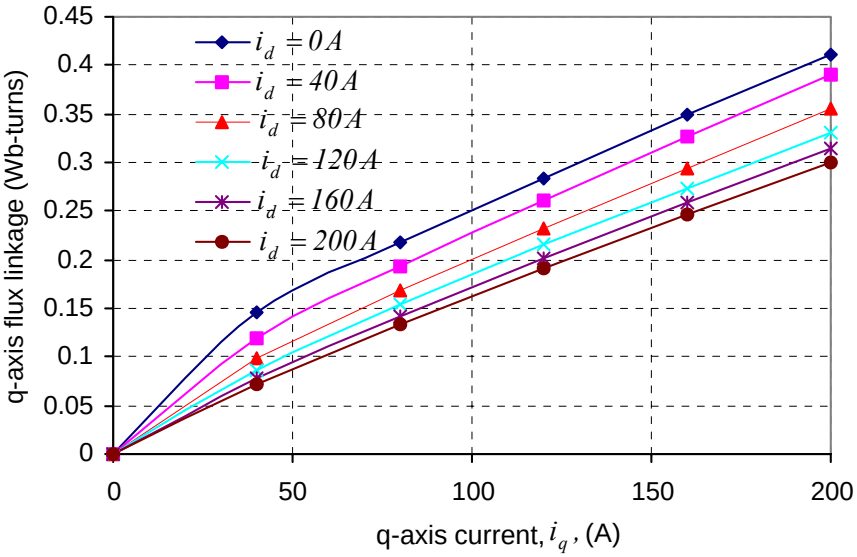

Figure 3.6(d): q-axis flux linkage versus i_q with i_d as a parameter of optimum FBR-rotor RSM.

The cross-coupling effect of the CR-rotor RSM is directly related to the pole arc of the CR-rotor. This then means that a small pole arc angle would result in a less cross coupling effect as compared to a bigger pole arc angle. In order to verify the relation between the pole arc angle and the cross-magnetisation effect, the cross-coupling investigation was extended to a CR-rotor RSM with a bigger pole arc angle. The pole arc angle was extended from the optimum value of 32.6^0 (2 times the rotor cut-out angle) to 50^0. The results of the cross-coupling effect with a bigger rotor cut-out angle are as shown in Figures 3.6(e) and (f). Noticeable from Figures 3.6(e) and (f) in comparison with Figures 3.6(a) and (b) is that there is definitely a severe cross-coupling effect with a larger rotor-cut out angle.

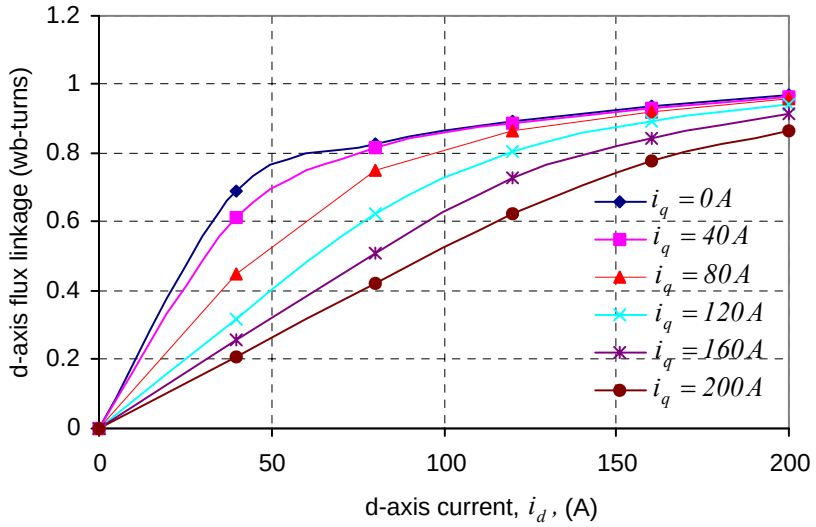

Figure 3.6(e): d-axis flux linkage versus d-axis current for the CR-rotor RSM with bigger pole arc.

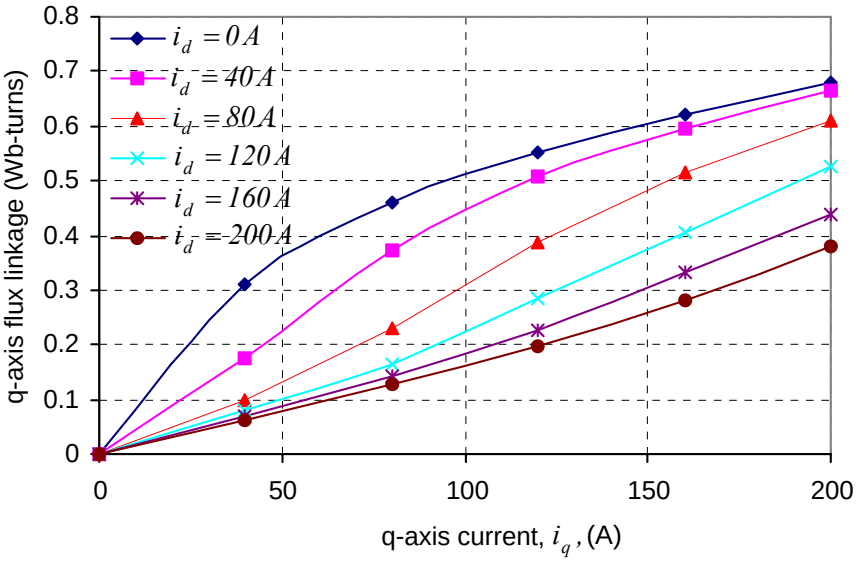

Figure 3.6(f): q-axis flux linkage versus q-axis current for the CR-rotor RSM with bigger pole arc.

The narrow pole arc implies less flux in the machine, which explains the small yoke height, s_{yh}, as compared to the yoke height of the FBR-rotor RSM. By maximising the torque in the design optimisation the latter drop in flux is compensated for by increasing the current of the machine. The current is increased by increasing the slot copper area and by reducing the stator inner diameter, d_i and this then explains the lower value of the stator inner diameter for the CR-rotor RSM.

3.6 Torque profiles

The FE calculated torque performances of the different skewed RSMs at 1 per unit load is shown in Figures 3.7(a) and (b). A summary of the FE average torque performances of the optimum machines at 1.0 per unit and at 2.5 per unit loads are given in Tables 3.3 and 3.4.

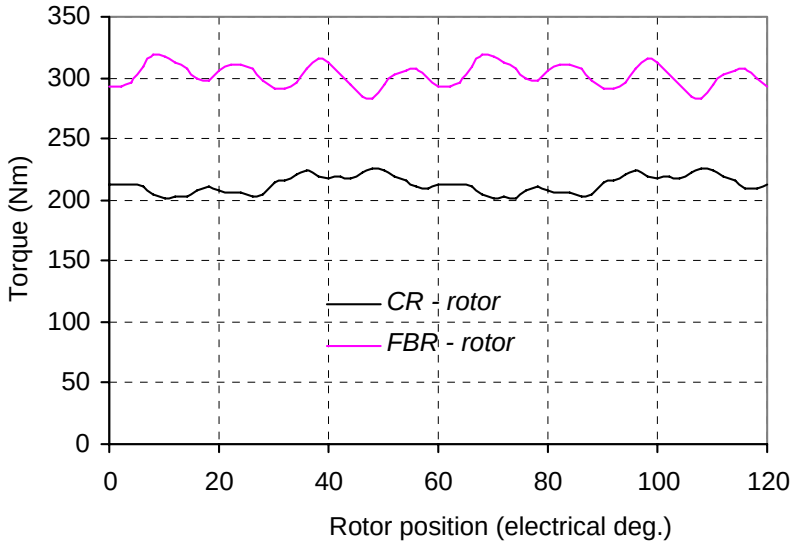

Figure 3.7(a): Torque profiles of optimum skewed 3-phase RSMs with different rotor structures.

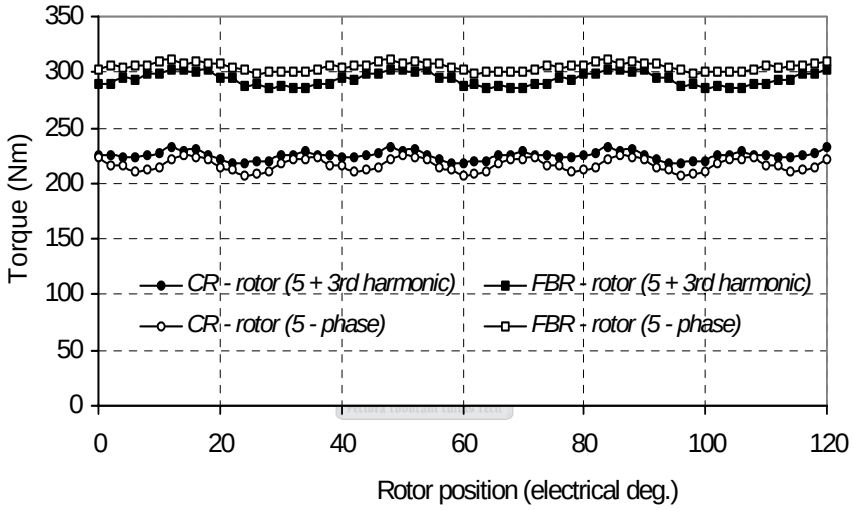

Figure 3.7(b): Torque profiles of optimum skewed 5-phase RSMs with and without 3rd harmonic currents with different rotor structures

Table 3.3: Torque in Nm of optimum designed RSMs at 1.0 per unit load

	FBR – rotor		**CR – rotor**	
Winding	Distributed	Concentrated	Distributed	Concentrated
3 – phase RSM	302	-	213	-
5 – phase RSM	305	276	217	201
5 + 3rd RSM	294	258	225	215

Table 3.4: Torque in Nm of optimum designed RSMs at 2.5 per unit load

	FBR – rotor		**CR – rotor**	
Winding	Distributed	Concentrated	Distributed	Concentrated
3 – phase RSM	770	-	530	-
5 – phase RSM	787	731	544	544
5 + 3rd RSM	757	691	568	574

From Tables 3.3, it can be observed that 5-phase RSMs with sinusoidal currents and the same rotor structure develop slightly higher torque (1% in the case of FBR-rotor RSMs and 2 % in the case of CR-rotor RSMs) as compared to their 3 phase counterparts. The 5-phase RSMs at 2.5 per unit load, as shown from Table 3.4, also develop slightly higher torque (2% in the case of FBR – rotor RSMs and 3% in the case of CR-rotor RSMs) as compared to their 3-phase counterparts. The 5-phase RSMs generate a much higher torque per *rms* current, this obviously implies that the phase current of the 5-phase RSM will be lower than that of a 3-phase RSM. As mentioned by Haataja (2003), increasing the number of phases of the RSM results in a reduced current per phase for higher reliability. The optimum phase current for the 5-phase CR-rotor RSM in relation to that of the 3-phase and 5-phase with the injection of 3rd harmonic currents RSMs is as shown in Figure 3.8.

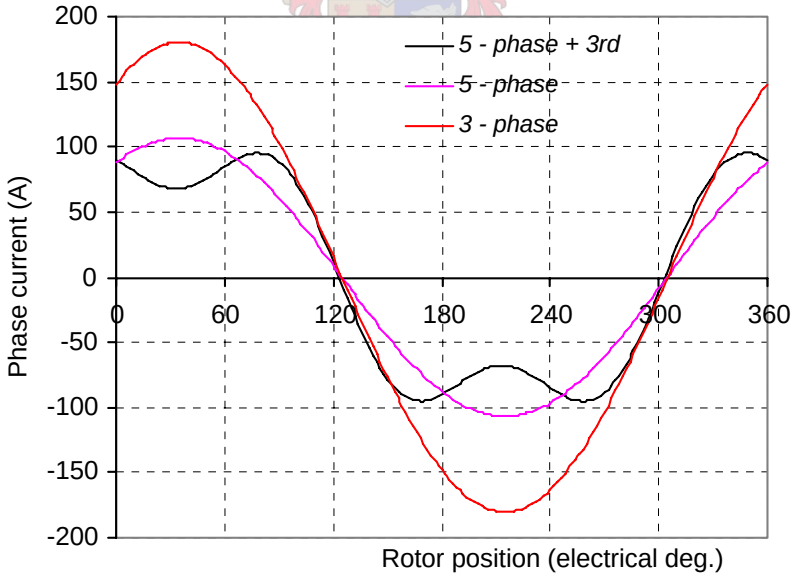

Figure 3.8: Phase current as a function of rotor position for the optimum 3, 5-phase and 5-phase with the addition of 3rd harmonic currents CR-rotor RSM at 1.0 p.u. Load.

Addition of third harmonic currents in case of 5-phase RSMs causes a further 3.7% torque improvement with the CR-rotor RSM but a drop of 3.6% with the FBR-rotor RSM. Similar results have been found by the previous researcher [Toliyat (1992, 1998)], but with a 10% torque boost for the 5-phase RSM with injection of 3rd harmonic currents with a salient pole

rotor. The most important result from Table 3.3, however, is that even though there is a torque decline for the FBR-rotor RSM, it still outperforms the 5-phase + 3rd harmonic current CR-rotor RSM by almost 24 % [Rakgati (2006)].

3.7 Analytical torque calculation

The analytical calculation of average torque is based on the torque equations developed from the previous chapter. The torque equations for the different RSMs are as follows:

- 3-phase RSM

$$T = \frac{3}{2} p(\lambda_d I_q - \lambda_q I_d) \tag{3.9}$$

- 5-phase RSM

$$T = \frac{5}{2} p(\lambda_d I_q - \lambda_q I_d) \tag{3.10}$$

- 5-phase + 3rd RSM

$$T = \frac{5}{2} p\{[\lambda_{d1} I_{q1} - \lambda_{q1} I_{d1}] + 3[\lambda_{d3} I_{q3} - \lambda_{q3} I_{d3}]\} \tag{3.11}$$

To calculate the torque by the use of the above equations, the *dq* flux linkages and the *dq* currents are required. The *dq* - flux linkages and the *dq* currents were determined as described in the previous chapter. With the *dq* - flux linkages and the *dq* - currents together with the number of poles, *p*, for the machines, the torque of the different RSMs were then calculated by the use of equations (3.9) – (3.11). The analytical calculated average torque of the machines at 1 per unit load in comparison with the FE Maxwell stress tensor method calculated torque is given in Table 3.5. It is noticeable from the table that there is a good agreement between the average torque calculated by the analytical torque equations and the one by the FE Maxwell stress tensor method. The torque calculated by the analytical torque equations is subject to a small error due to the approximations in the determination of the fundamental flux linkages as described in the previous chapter.

Table 3.5: Analytical and FE calculated torque at 1.p.u. load

	FBR – rotor		**CR – rotor**	
Machine Type	FE	Analytical	FE	Analytical
3 – phase RSM	302.1	302.8	212.6	212.2
5 – phase RSM	304.9	305.8	216.8	217.8
5 + 3rd RSM	293.7	295.0	224.8	225.8

3.8 Torque Quality

For the context of the investigation, torque quality refers to the smoothness of the torque versus position. So the quality of the torque is directly related to the torque ripple (that is the more ripple the lower the quality). As mentioned by various researchers [Chiricozzi (1996), Vagati (2000)], the main disadvantage of RSMs is the torque ripple that is mainly due to the inductances variation with rotor position. This can result in inaccuracy in motion control, noise and vibrations especially at low speeds.

The RSMs considered in this thesis are all normal (transverse) laminated, thus they do have a large torque ripple [Chiricozzi (1996)]. Skewing of the rotor by a slot pitch minimises the torque ripple [Fratta (1995), Bomela (2002)] of the machines as shown in Figures 3.9(a) to (d). As mentioned earlier in the chapter, the normal transverse laminated rotor structures can be skewed easily. It can be observed from the Figures that skewing the machines (both the FBR-rotor RSM and the CR-rotor RSM) reduces the torque ripple drastically. This thesis does not focus on the torque ripple of the machines as skewed machines are considered.

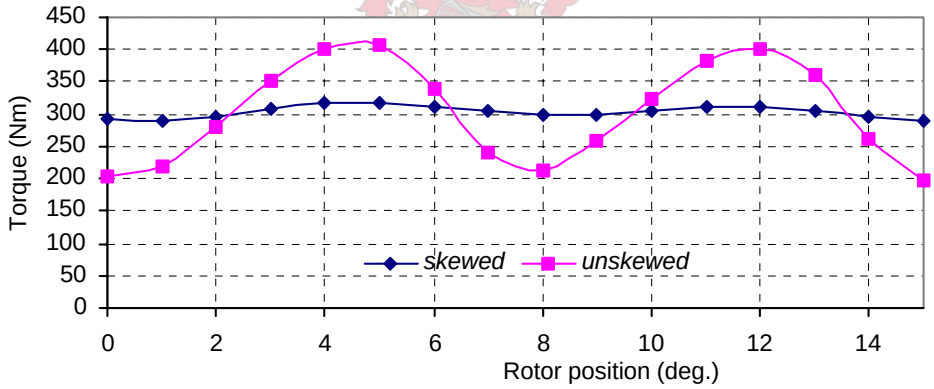

Figure 3.9(a): Torque versus rotor position for 3 - phase FBR – rotor RSM.

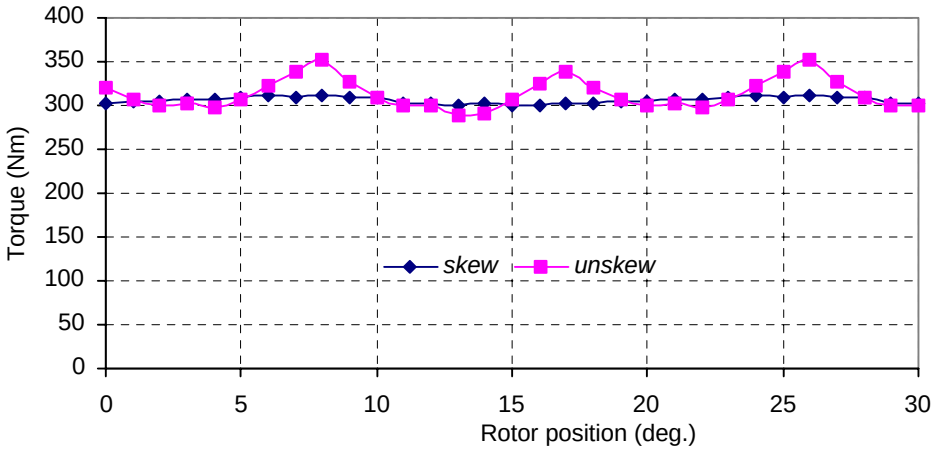

Figure 3.9 (b): Torque versus rotor position for 5-phase FBR-rotor RSM

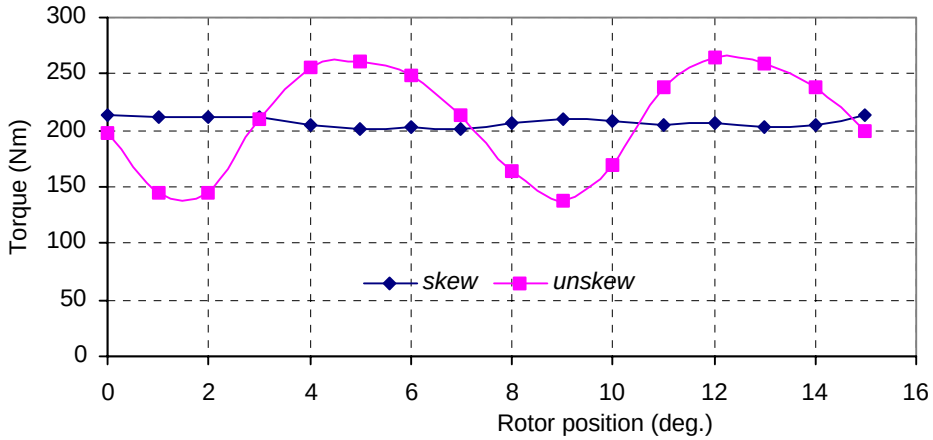

Figure 3.9(c): Torque versus rotor position for 3-phase CR-rotor RSM

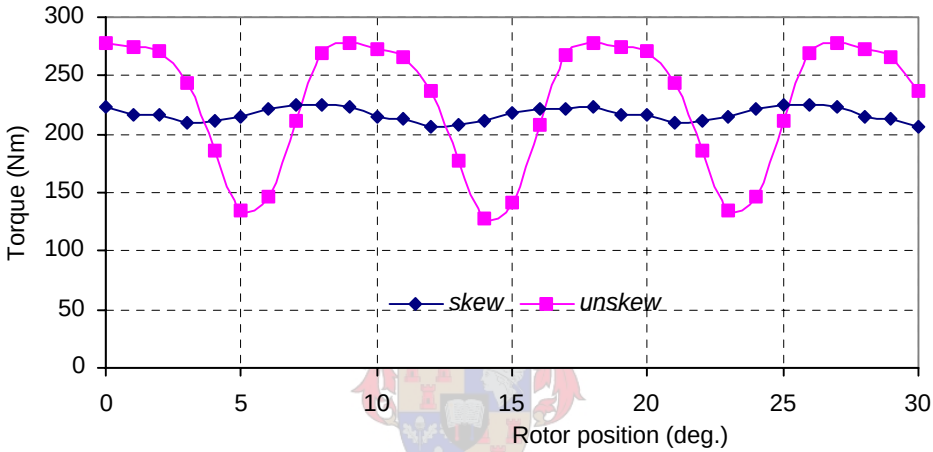

Figure 3.9 (d): Torque versus rotor position for 5 - phase CR-rotor RSM.

3.9 Measured results

In order to verify the accuracy of the FE analysis, practical measurements are performed on the designed RSMs. So the optimally designed 3-phase FBR-rotor RSM was built and tested, with the rotor unskewed and a 48-slot stator winding. For the test of the above-mentioned machine, the drive system of Figure 3.10 was used. The machine was controlled by a fixed point DSP with current and position feedback so as to allow for current control and speed control through a 3-phase IGBT inverter. Fibre optic was used to link the DSP to the inverter. Loading in this case was done by the use of a water-cooled eddy-current dynamometer, which was coupled to the test machine.

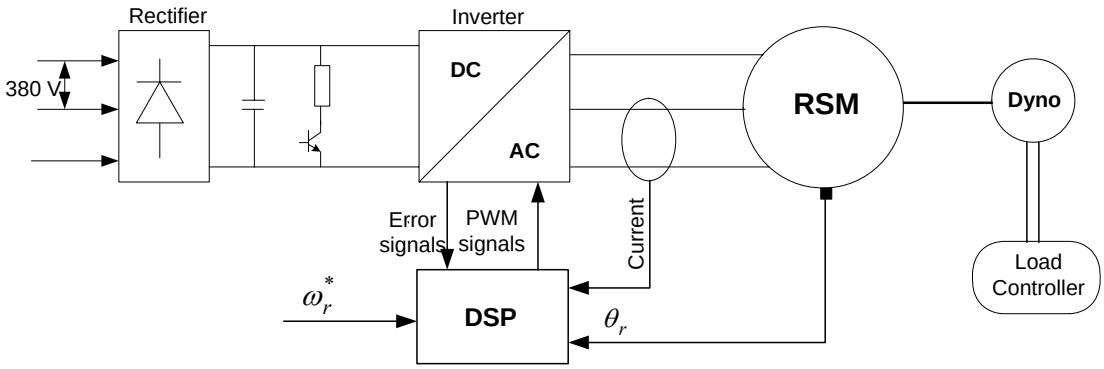

Figure 3.10: The RSM drive system

The steady state torque performance of the machine was conducted at rated speed, to determine the full load torque of the machine as a function of the current angle. The measured as well as the FE calculated results are as shown in Figure 3.11.

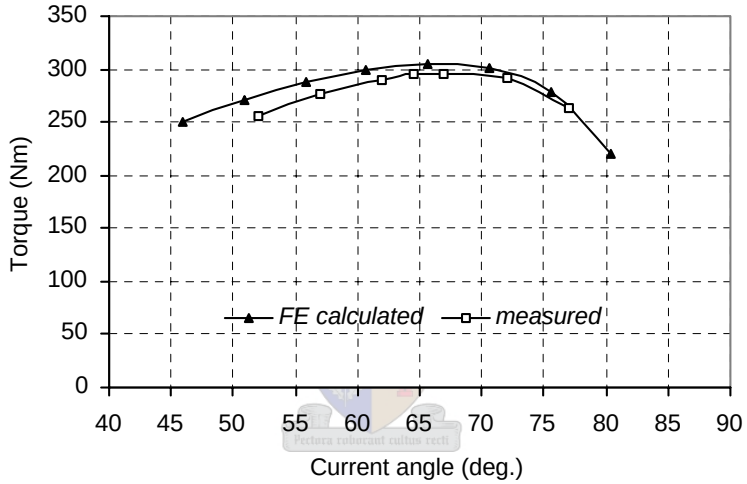

Figure 3.11: Calculated and measured results of torque versus current angle of the 3-phase FBR-rotor RSM

From Figure 3.11, it can be seen that there is a good agreement between the measured and the FE calculated results. The only slight difference is the optimum current angle; the measured optimum current angle is slightly more than the calculated one due to the magnetostatic field solutions that do not account for the damping effect of the eddy currents and iron losses.

There was no further opportunity to build and test the 5-phase RSM as the focus of the thesis is on the 6-phase RDCM that is tackled in the next chapters. The CR-rotor RSM is to be extended to the RDCM principle that finally leads to the building and testing of the 6-phase RDCM.

3.10 Conclusions

From the finite element results and the measured results, the following conclusions are drawn on the torque performances of the different RSMs for the same copper losses and the same stack volume:

- With the same rotor structure the 5-phase RSMs develop slightly more torque than the 3-phase RSMs. The 5-phase RSMs also generate a much higher torque per *rms* phase current.
- Under sinusoidal 3- and 5-phase conditions the RSMs with the internal flux barrier reluctance rotor develop more than 33% higher torque as compared to the RSMs with the cut-out reluctance rotor.
- The 5-phase RSM with the injection of third harmonic currents and using the cut-out reluctance rotor results in only 3.7% increase in torque as compared to the same machine with sinusoidal currents. However, with the internal flux barrier rotor the torque decreases by 3.6%. The increase in torque with 3rd harmonic current injection depends, thus, on the type of the rotor structure used [Xu (1992)].
- Even though there is an increase in torque due to the injection of the 3rd harmonic currents in the case of the 5-phase RSM with the cut-out reluctance rotor, the 3-phase RSM with the internal flux barrier rotor still outperforms this machine by almost 24%.
- It has also been shown that the optimum designed sinusoidal RSMs with more slots per phase (i.e. distributed winding) yielded a higher torque per copper loss as compared to those with concentrated winding.
- From the good agreement of the measured and FE calculated results for the FBR-rotor RSM, thus confirms that FE calculated results can be relied upon.

CHAPTER 4 Reluctance DC Machine

In this chapter the operation principle of the reluctance DC machine (RDCM) based on the working principle of the permanent magnet DC machine is described. The RDCM is an RSM with a salient pole rotor and excited with special current waveforms. The chapter further expands to development of special current waveforms suitable to transform a normal salient pole RSM (CR–rotor RSM) to an RDCM. The RDCM current waveforms are developed from the current waveforms of the 5-phase RSM with the injection of third harmonic currents as discussed in previous chapters. The reason for the latter is that the torque performance of the CR-rotor RSM is improved by the injection of the 3rd harmonic currents. It is also worth mentioning that this chapter focuses on 5-phase machines only.

The best current waveform must yield constant rotating MMF in the airgap. The verification of the current waveforms for the desired rotating MMF is performed both graphically and analytically. The rotating MMF analysis is carried out with field current only in the machine, as the field current is the main player in the production of flux in the machine. The chapter extends to the modelling of the RDCM. The modelling of the machine involves developing the EMF and torque equations of the RDCM based on ideal phase current and flux linkage waveforms.

4.1 Operation principle of the Reluctance DC machine

It is worthwhile to gain insight into the working principle of the RDCM before developing the machine equations. The working principle of RDCM is derived from the operation principle of the permanent magnet brushless DC machine (BDCM).

4.1.1 Permanent Magnet brushless DC machine

The permanent magnet brushless DC machine has magnets fixed to the surface of the rotor and has a normal stator winding as shown in Figure 4.1(a). The machine is configured in such a way that the permanent magnet rotates past the stationary phase current carrying windings, equivalent to the DC commutator motor.

The current in the conductors must change polarity every time the magnet passes by so as to ensure that the torque is unidirectional. In a normal DC motor, the polarity change is done by commutators and brushes while in the brushless DC machines the polarity reversal is done through power electronic switches that are switched in synchronism to the rotor position.

BDCMs are sometimes also referred to as square wave machines because of the fact that the air gap flux density, induced EMF, phase current and applied voltage are ideally of the square waveshape. These machines do conform to the DC commutator machine principles in the sense that during steady state the induced phase EMFs and currents are DC quantities. The basic torque and EMF equations are therefore very simple, and resemble those of a DC commutator motor. The typical phase current waveform for the 5-phase BDCM is shown in Figure 4.1(b) [Hendershot (1984)]. It can be observed from the phase current waveform that the magnet pole angle must at least correspond to the width of the square current waveform which is in this case 108 mechanical degrees.

As mentioned earlier, the switching of the stator winding currents as a function of position is an important aspect for the BDCMs. Consider Figure 4.1(a), showing the 5-phase current distribution in the stator winding along the airgap of the machine. It can be observed that equal current flows only in stator coils A to C, which results in MMF along the *q-axis* of the rotor. No current is flowing in stator coils D and E. Note, however, that with equal current in coils D and E, the resultant MMF is along the *d-axis*. According to the working principle of the machine, currents in the d-axis stator coils will contribute to the flux of the machine, while the q-axis currents will contribute towards the torque of the machine. The stator d-axis currents or field current is not necessary for the BDCM due to the fixed airgap flux provided by the magnets. The current distribution in the q-axis stator coil is symmetrical across the q-axis so as to generate the flux-vector, φ_q, perpendicular to the magnet flux vector, φ_m.

There are two key features which are worth mentioning about the BDCM, namely: (i) the air gap flux provided by the magnet is less affected by the *q-axis* stator current due to the large airgap of the machine, so the cross magnetisation or armature reaction is very small and (ii) due to the fact that the magnets provide for the flux in the machine, the magnet pole can be enlarged to 180 degrees, allowing stator coils D and E to be included as *q-axis* stator coils, resulting in a more efficient machine. Note for explanation purposes of the RDCM in the next section, three phases are assumed to be active anytime resulting in the 108 degree current pulse; for BDCM operation four phases active with 144 degree current pulse can also be assumed. It should be noted that the inverter topology is not considered in this explanation. The inverter can be either a full bridge inverter or a divided DC bus inverter with neutral if the summation of the phase currents is not zero. If the summation of the phase currents is zero a half-bridge inverter can be used.

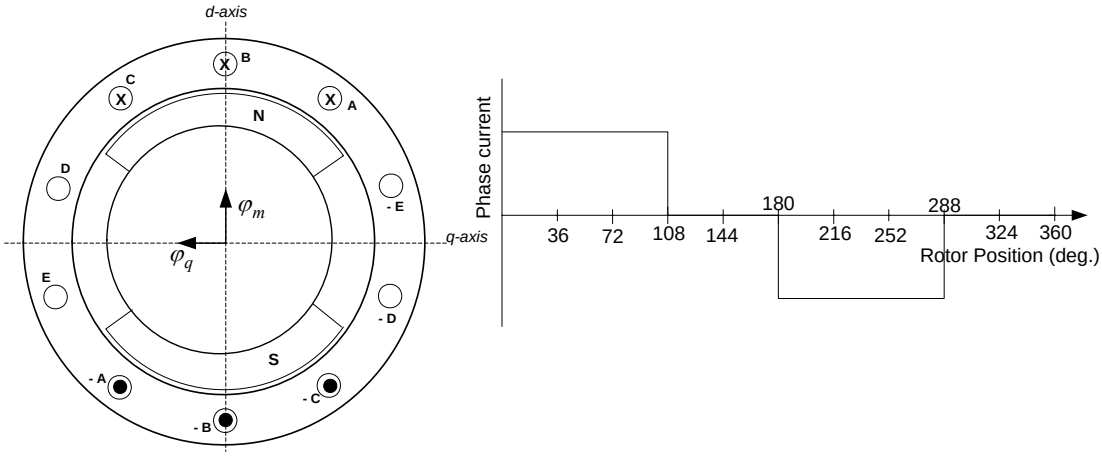

(a) (b)

Figure 4.1(a): 5-phase permanent magnet brushless DC machine and (b) its typical phase current waveform.

4.1.2 Reluctance DC Machine

The operation principle of the RDCM is exactly the same as that of the BDCM, except for the fact that in the RDCM field current is required as there are no magnets that provide for the flux in the machine. The structure of the RDCM is as shown in Figure 4.2(a).

For the RDCM to work exactly the same as the BDCM, the following conditions have to be satisfied:

(i) With the absence of the permanent magnets a magnetic field has to be created in the RDCM. This is done by injecting current in the d-axis stator coils (that is current in coils D and E at the particular position)

(ii) The magnetic field or airgap flux may not be disturbed by the q-axis stator current, that is, the flow of q-axis flux must be reduced so as to reduce cross magnetisation or the so called armature reaction effect. This as shown in Figure 4.2(a) can be obtained by the use of flux barrier rotors.

Based on the typical phase current waveform of the BDCM of Figure 4.1(b), the phase current waveform can be modified to cater for the d-axis stator current as shown in Figure 4.2(b).

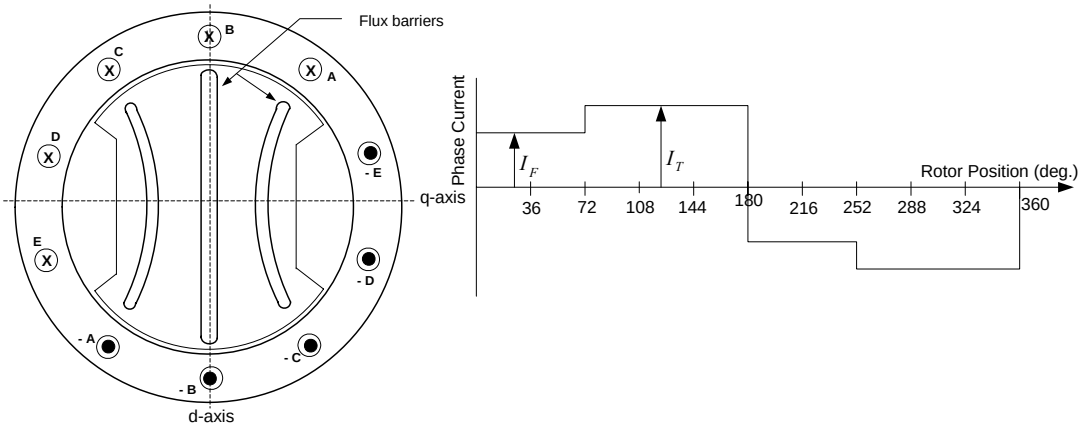

(a) (b)

Figure 4.2(a): 5-Phase reluctance DC machine and (b) Square current waveform [Weh (1984)].

With the rotor at the position shown in Figure 4.2(a), coils A to C act as torque coils while coils D and E act as field coils. For field distribution, the current adjustment in coils D and E must be symmetrical across the *d-axis*. The same applies to the torque generation; the current distribution in coils A to C must be symmetrical across the *q-axis*. As the rotor rotates, the stator coils alternatively function as field or torque producing coils depending on the position of the rotor. For example, if the rotor rotates by one stator slot pitch clockwise, coil C changes from a torque coil to a field coil to operate together with coil D, while coil E changes from a field coil to torque coil to operate together with coils A and B. With the RDCM, the amplitude of the field and torque currents can be varied independently to adjust the field and the torque of the machine directly just like with a separately excited DC machine.

From the above explanations, it can be concluded that the square current waveform is typically used for RDCMs. However the suitability of the square current waveform is questioned. The current waveform is considered to be suitable, according to the context of this thesis, if it yields a constant smooth-rotating MMF, higher torque and less torque ripple. The MMF due to the square current waveform is analysed in this chapter, while the torque performance is analysed in the next chapter.

4.2 Principle of field and torque current components

In this section, a best current waveform for the RDCM is developed based on the current waveform of the 5-phase RSM with the injection of third harmonic currents. As mentioned in chapter 3, the addition of 33% third harmonic currents to the 5-phase sinusoidal currents

results in a boost in the torque of CR-rotor RSMs, so further analysis will now concern RSMs with salient pole rotors.

The 5-phase with the injection of third harmonic currents can then be modified to cater for the separate field and torque currents. Bearing in mind that salient pole rotors are used for the RDCMs, the current distribution has to be arranged in such a way that the field current coincides with the large airgap area and the torque current with the small air gap area (pole arc). The separate field and torque currents can be achieved by adding 100% third harmonic currents to the fundamental as shown in Figure 4.3(a) instead of the 33% third harmonic as discussed in the previous chapter. Just like for the addition of 33% third harmonic current to the fundamental, the addition of 100% third harmonic current in this context means that the amplitude of the 3rd harmonic current being added to the fundamental is of the same amplitude as the fundamental current as reflected in Figure 4.3(a).

As shown in the figure, the current waveform divides into two half cycles, which can be utilised to emulate the field and torque currents. But what should be noted from Figure 4.3(a) is that the current waveform is not symmetrical. The unsymmetrical current waveform results in an unsymmetrical current distribution as shown in Figure 4.3(b). Hence the field flux vector, φ_F, and the torque flux vector, φ_T, will not be orthogonal and thus will not conform to the DC machine principle. The current distribution is derived with an assumption that the current angle is 45 degrees. Noticeable from the figure is the current distribution as compared to that of the sinusoidal (refer to Figure 3.3(c)) and the sinusoidal with an addition of third harmonic current (refer to Figure 3.4) that was discussed from the previous chapter.

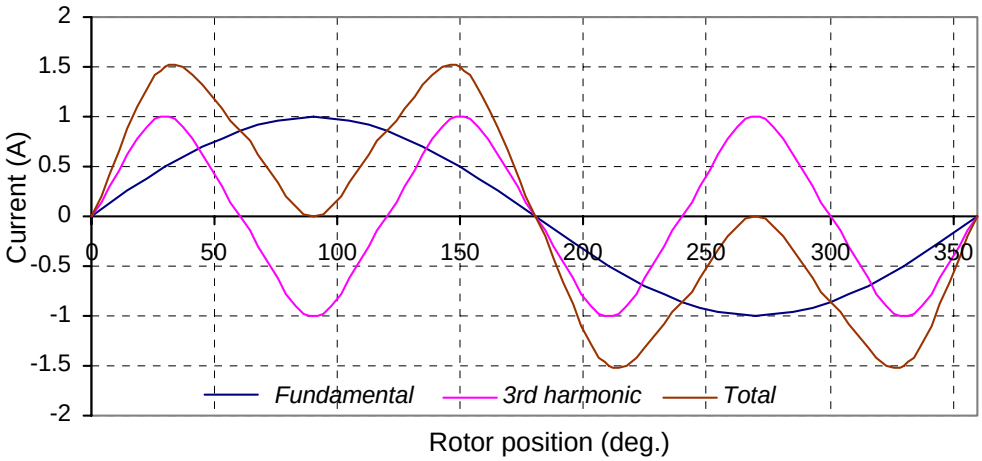

Figure 4.3(a): Fundamental current with the addition of 100 % 3rd harmonic current versus rotor position.

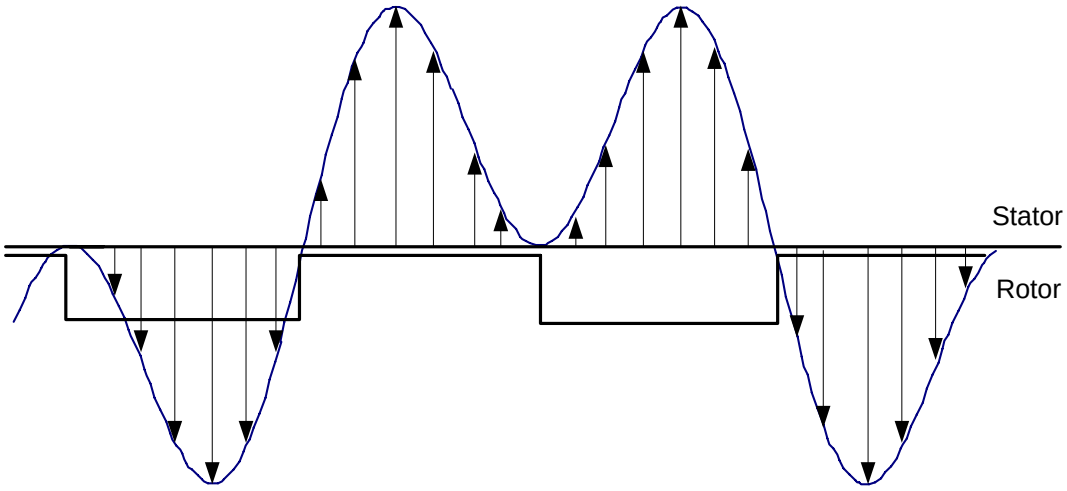

Figure 4.3(b): Current distribution with respect to rotor position of the RSM with fundamental current and the addition of 100% 3rd harmonic current.

The above current distribution can be improved so as to make it symmetrical as shown in Figure 4.3(c) resulting in a symmetrical half-sinusoidal current waveform. The improvement of the current distribution by the use of the half-sinusoidal current waveform is as shown in Figure 4.3(d). It can be observed from the current distribution that the torque current is uniformly distributed on top of the salient poles, while the field current is distributed in between the poles.

Just like in brush dc machines, the field and the torque currents should be able to be controlled separately as shown in Figure 4.3(e). Figure 4.3(e) shows the half-sinusoidal current waveform with field and torque currents of different amplitudes. The amplitudes of the field and torque currents are dictated by the flux and the load of the machine respectively. Hence, there is an amplitude-ratio defined by:

$$\gamma = \frac{I_F}{I_T} \tag{4.1}$$

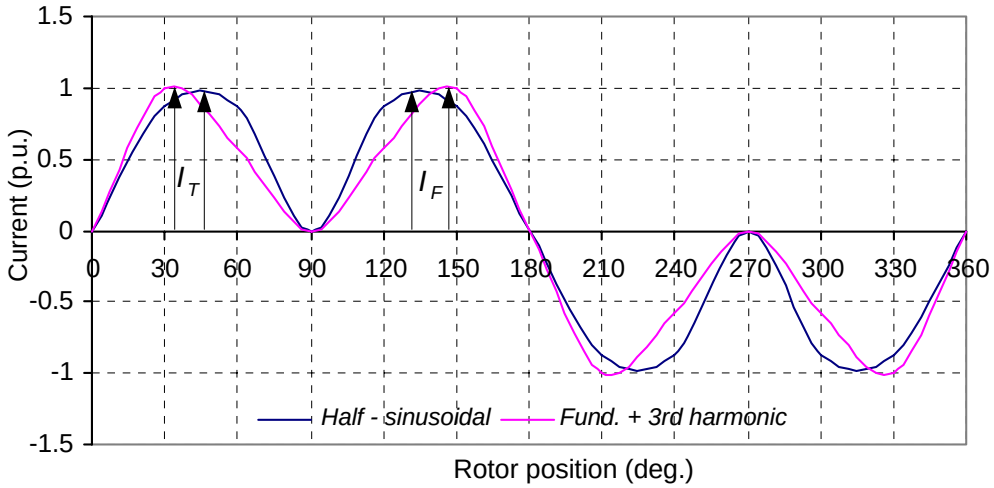

Figure 4.3 (c): Fundamental with an addition of 100 % 3rd harmonic and the half-sinusoidal current versus rotor position.

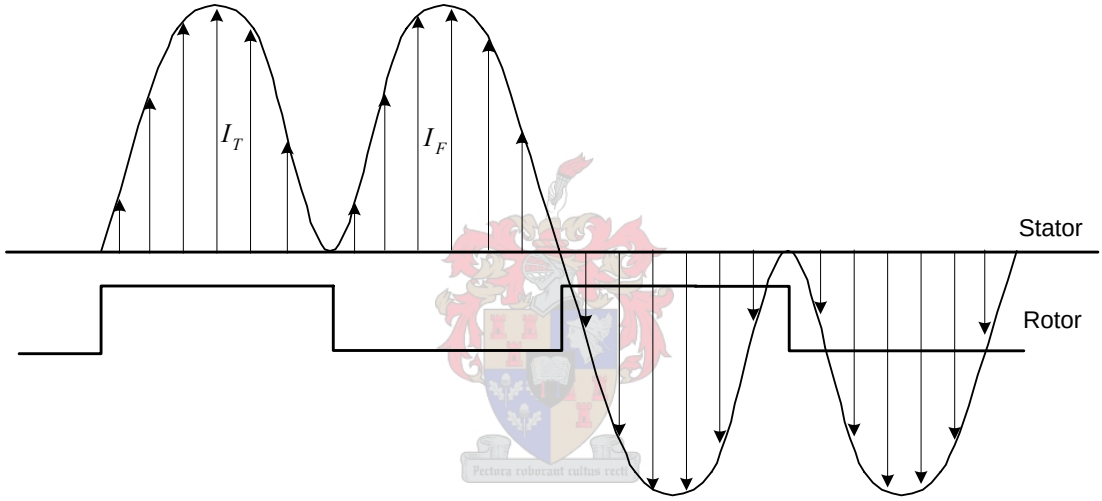

Figure 4.3(d): Current distribution in the RSM with half-sinusoidal current waveform.

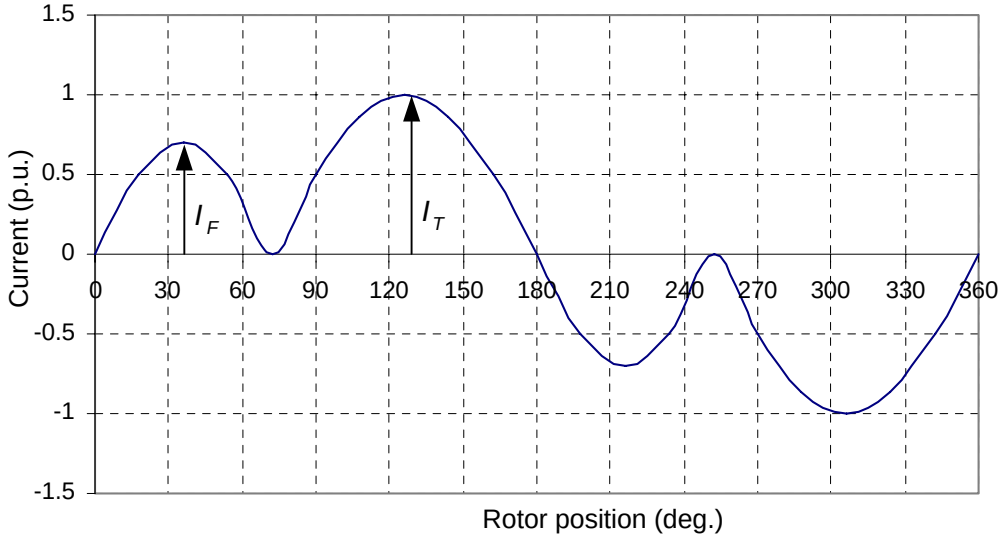

Figure 4.3 (e): Half- sinusoidal current waveform with field and torque currents of different amplitudes.

Furthermore, depending on the phase number, the angle-ratio of the field to torque current angles can be adjusted. The ratio of the field to torque current conducting angles is defined as follows:

$$\vartheta = \frac{\theta_F}{\theta_T}, \tag{4.2}$$

where θ_F and θ_T are the field and torque current angles respectively. For example $\vartheta = 2/3$ for the waveform of Figure 4.3(e). Hence, the ratio of the field to torque current conducting angles dictates the pole-angle geometry of the rotor. The pole-angle geometry in this context is defined as follows [Boldea (1996)]:

$$\theta_p / \theta_\tau = m_T / (m_F + m_T), \tag{4.3}$$

where m_T and m_F are the number of torque phases and the number of field phases respectively. As can be seen in Figure 4.3(e), the current waveform is formulated to have an angle-ratio of 2/3 resulting in a rotor pole-angle geometry of 3/5. This pole-angle geometry ratio can best be explained by the 5-phase machine of Figure 4.3(f), where the number of torque phases, m_T, is 3 while the number of field phases, m_F, is 2. From the figure and equation (4.3), the ratio of the pole-angle geometry is 3:5.

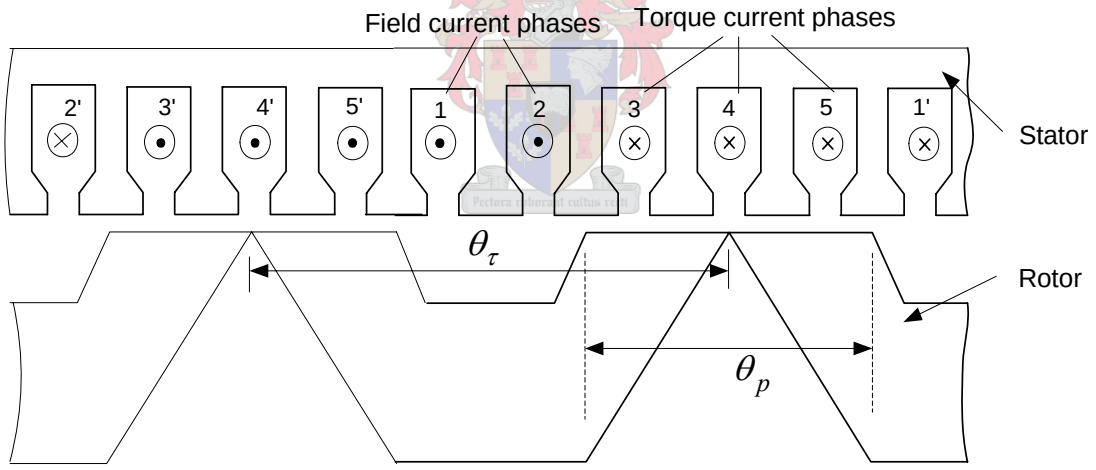

Figure 4.3(f): 5-phase RSM with pole-angle geometry ratio of 3:5.

4.3 Analysis of the current waveforms for the RDCM

The next step in developing a suitable current waveform for the RDCM is to further modify the above-described half-sinusoidal current waveform. The modified current waveforms together with the half-sinusoidal current waveforms are to be analysed in terms of the rotating MMF, so as to select the best current waveform based on the smoothness of the rotating MMF.

The modified current waveforms to be considered in this section apart from the half-sinusoidal current waveform are the trapezoidal and the square current waveforms. The square current waveform was long ago proposed by Weh (1984) {refer to Figure 4.2(b)} and further applied by Boldea (1991) and Law (1994, 1996). The current waveforms are as shown in Figure 4.4. It can be observed that for the trapezoidal current waveform the field part is triangular while the torque part is trapezoidal in shape. For the square current waveform both the field and the torque currents are of the square shape. In addition to the shape of the current waveforms, it can be seen that the proposed phase current waveforms for the 5-phase RDCM have a field to torque current angle ratio of 2:3.

In the context of this chapter, the best current waveform is selected based on rotating smoothness and amplitude variation of the generated airgap MMF. The analysis of the rotating MMF for the different current waveforms is carried out with field currents only, that is, the torque current is taken to be zero. This is done under ideal conditions as only the field current MMF is contributing to the flux production in the machine. However, in the real sense the torque current MMF does also contribute negatively to the magnetic flux in the machine through the cross-coupling or armature reaction effect.

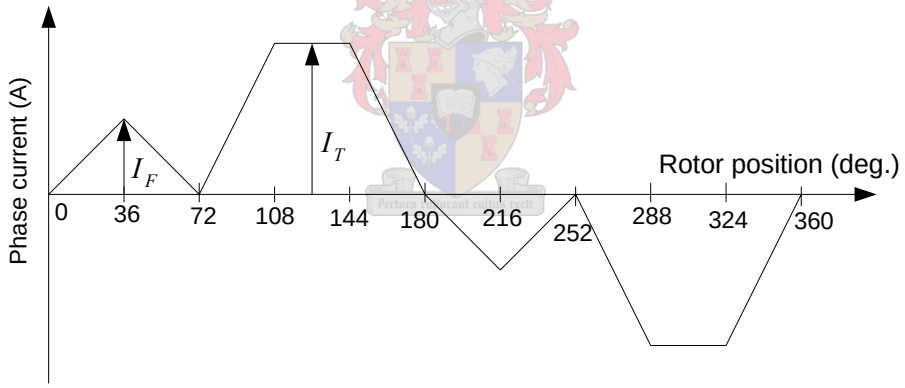

Figure 4.4(a): Trapezoidal phase current waveform for the 5-phase RDCM

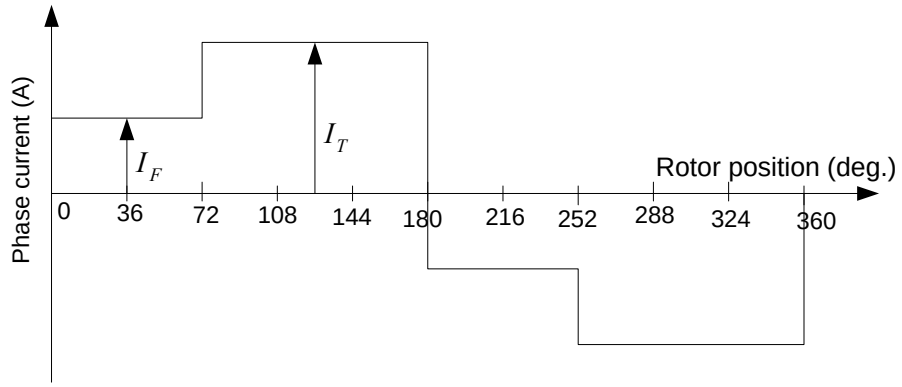

Figure 4.4(b): Square phase current waveform for the 5-phase RDCM [Weh [1984]]

4.3.1 Analysis of the rotating magnetic field

This section focuses on the rotating airgap MMF with the different current waveforms in a 5-phase RDCM. For the analysis of the rotating MMF a two pole 5-phase machine with a salient pole rotor is considered as shown in Figure 4.5. It is worth mentioning that in this analysis, concentrated, full pitch phase windings are assumed. The five phase windings are displaced in space from each other by 72 degrees. Noticeable from the Figure is the winding layout of the 5-phase RDCMs. This winding layout is adopted for the 5-phase RDCMs.

When current flows through a phase coil, it results in an airgap MMF centred on the axis of the phase coil. The magnitude and the direction of the MMF is a function of the instantaneous value of the current flowing through that particular phase coil, so the arrows in Figure 4.5 indicate the magnitude and direction of the different phase coil MMFs. The direction of the MMF is determined by the right hand rule. The airgap MMF of the different phase coils are given by $\vec{F}_i$ where $i = a,b,c,d,e$ as shown from the figure.

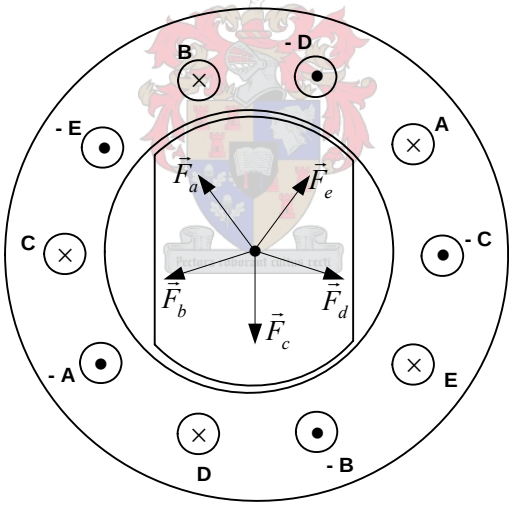

Figure 4.5: 5-phase RDCM showing the magnitude and direction of peak phase resultant MMF.

The analysis of the rotating MMF of the distributed winding can be approached by studying the magnetic field of a single N-turn coil that spans for a full-pitch as shown in Figure 4.6(a). On the assumption of a uniform airgap, the MMF for the single coil, taking coil C as an example, is shown in Figure 4.6(b). It can be observed from the figure that the MMF distribution is shown to have a steplike distribution of amplitude $\pm Ni/2$. The rectangular MMF wave can then be resolved into fourier series comprising of the fundamental component and a

series of odd harmonics [Fitzgerald (1990)]. In the analysis that follows, the series of odd harmonics is ignored, only the fundamental is considered as shown in Figure 4.6(b).

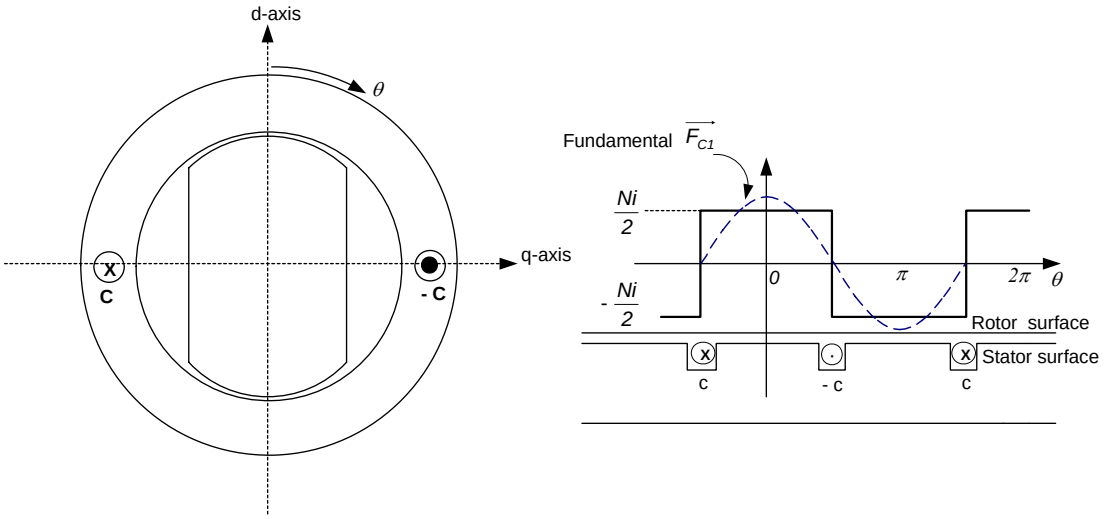

(a) (b)

Figure 4.6: The MMF of a concentrated full-pitch N-turn coil.

The fundamental component of the rectangular MMF wave as derived from fourier series is a cosine function given by the following equation:

$$F_{c1} = F_{c1peak}\cos\theta, \tag{4.4}$$

where $F_{c1peak} = \frac{4}{\pi}\frac{Ni_c}{2}$.

θ is measured from the magnetic axis of the stator coil, as shown by the dotted sinusoid in Figure 4.6(b). It is a sinusoidal space wave of amplitude F_{1peak} and with its peak aligned with the magnetic axis of the coil. In a similar manner as for phase C, the fundamental MMFs of the other phases are given in general form by equation (4.5). It should be noted that the other phase MMFs are derived with the phase C magnetic axis taken as the reference and also following the winding layout of Figure 4.5.

$$F_{j1} = F_{j1peak}\cos(\theta - n36) \tag{4.5}$$

with $j = a,b,c,d,e$ and corresponding $n = 0,1,2,3,4$ and

$$F_{j1peak}(\theta) = \frac{4}{\pi}\frac{N}{2}i_j(\theta). \tag{4.6}$$

It should be noted that $F_{j1peak}(\theta)$ is a function of position as i_j of equation (4.6) is a function of θ, i.e. $i_j(\theta)$. Therefore $\vec{F}_{j1}$ is a function of θ, i.e. $\vec{F}_{j1}(\theta)$, as the magnitude is a function of θ. Equation (4.5) can be expressed in phasor notation as follows:

$$\vec{F}_{j1}(\theta) = F_{j1peak}(\theta)\angle - n\zeta \tag{4.7}$$

where $\zeta = 180/m$ and m is the number of phases.

In the next section the analysis will be extended to the 5-phase RDCM with the square current waveform, the trapezoidal current waveform and the half-sinusoidal current waveform.

(a) Square current waveform

Considering first the square current waveform of Figure 4.4(b) in the analysis, with only field current ($I_T = 0$), the phase current waveforms are as shown in Figure 4.7. The phase current waveforms are active depending on the rotor position. Bearing in mind that only the fundamental MMF is considered, the resultant MMF at any particular rotor position is the net effect of the MMF of the active phases, which can be computed either graphically or analytically.

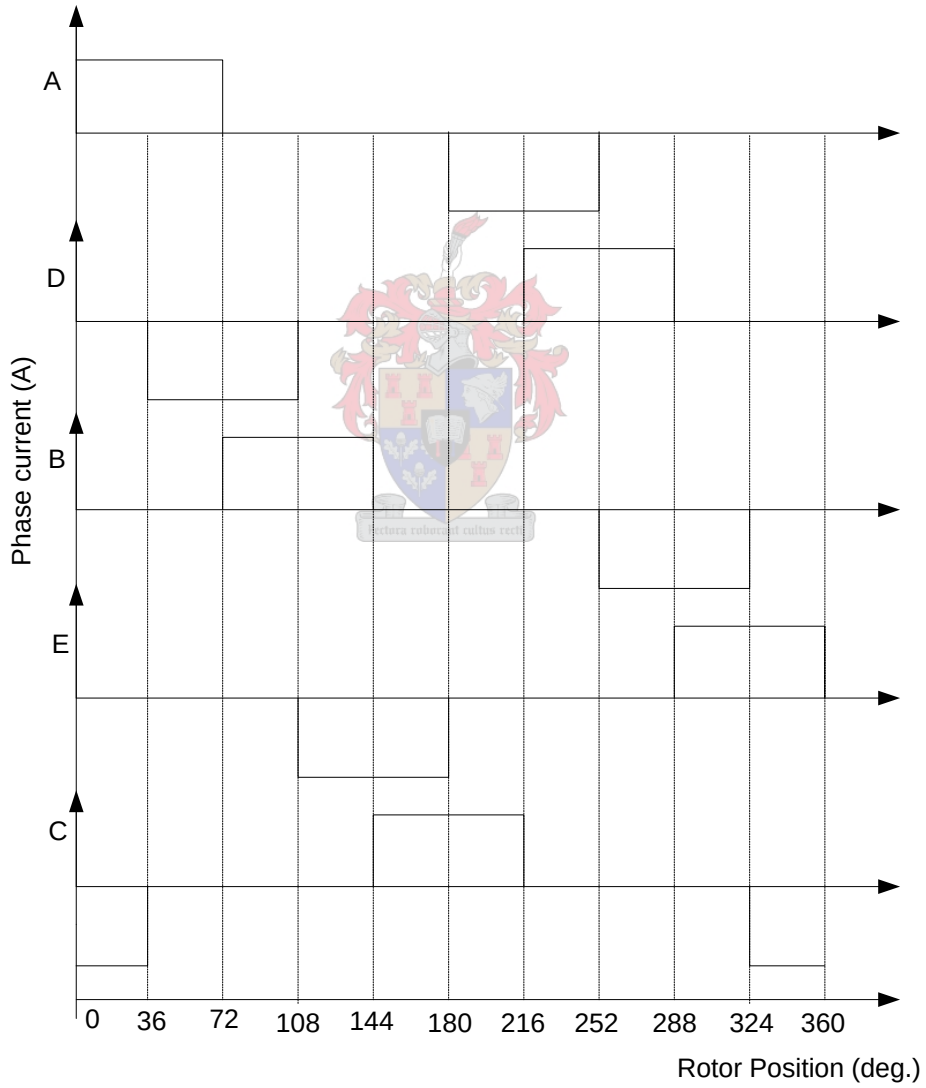

Figure 4.7: 5- phase square current waveform with field current only for the 5-phase RDCM.

(i) Graphical method

From Figures 4.5 and 4.7, the resultant MMF with rotor movement can be determined graphically. The resultant MMF is determined for three instants as shown in the Figure 4.8. For example, at position zero, two phases are active (phases A and C) implying that the resultant MMF is the phasor addition of the two phasors. The method is repeated for two other positions namely at 36 and 72 degrees as shown in the figure.

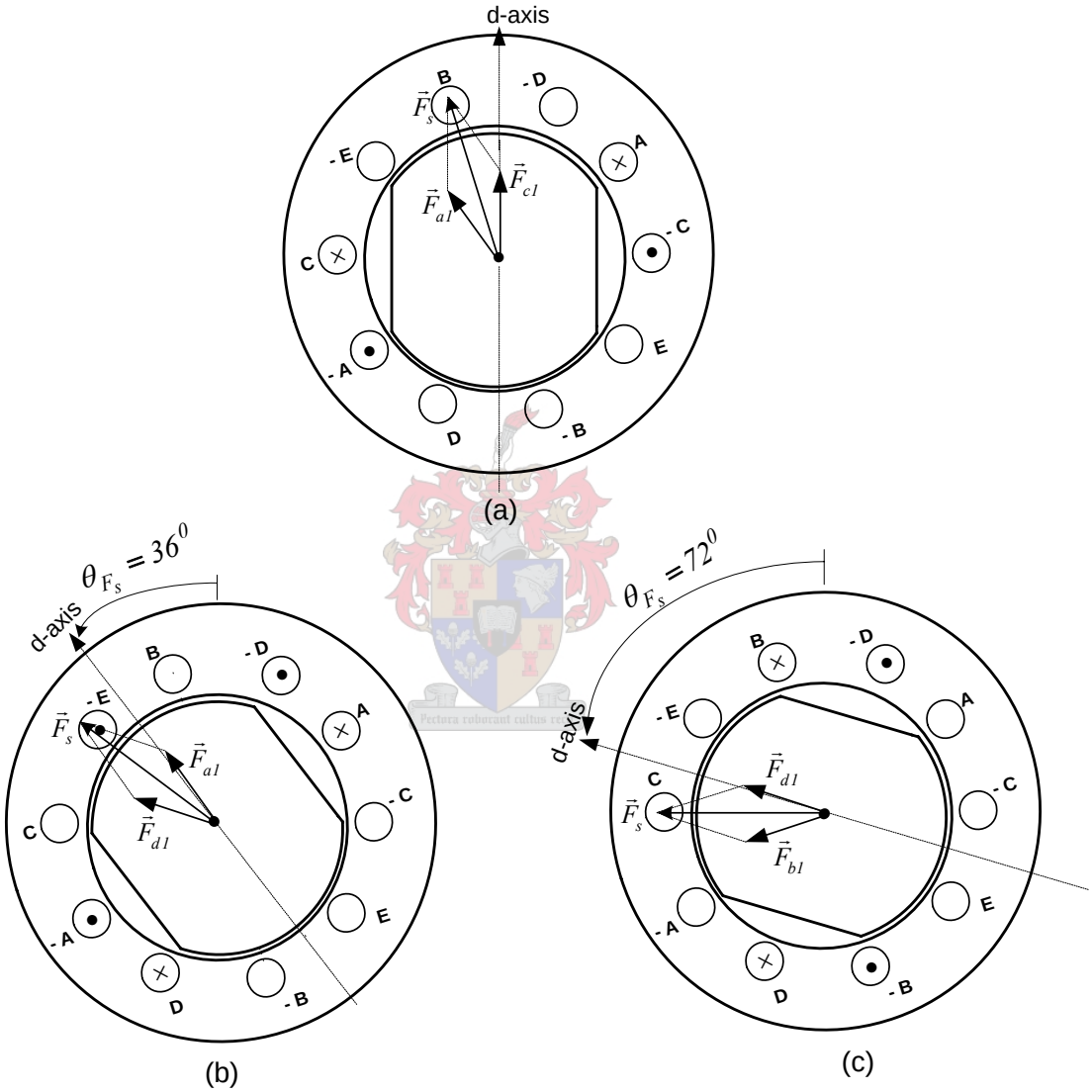

Figure 4.8: Graphical representation of rotating MMF at three rotor positions namely: (a) 0^0, (b) 36^0 and (c) 72^0 with the square field current waveform.

It is noticeable from Figure 4.8 that the resultant MMF, $\vec{F}_s$, does not rotate smoothly with the rotor, i.e. the resultant phasor is not always in phase with the rotor d-axis. For instance at rotor positions 0-36^0, the resultant MMF is fixed at position 18^0. Then at rotor position of 36^0 the resultant MMF jumps to 54^0 and remains fixed at that position for all rotor positions up to 72^0.

(ii) Analytical Method

Just like for the graphical method, the same two-pole machine with five phase windings on the stator is considered analytically. Bearing in mind, that the MMF is a function of current, it is therefore worth considering which phase winding contribute to the airgap MMF at a particular position. An analytical expression of the resultant MMF at any point in the airgap can be derived. Based on the five-phase field current waveform of Figure 4.7 it is clear that, at any instant of time, two phases contribute to the airgap MMF. The stator MMF phasor, $\vec{F}_s(\theta)$, in the airgap at different rotor positions is given by equations (4.8) – (4.12). Note that the contribution of the phases to the resultant MMF varies with rotor position. As explained in the previous section, the MMF analysis is based on the peak fundamental component of the MMF.

$$\overrightarrow{F_s}(\theta) = \overrightarrow{F_{a1}}(\theta) + \overrightarrow{F_{c1}}(\theta) \qquad 0 \le \theta \le 36 \qquad (4.8)$$

$$\overrightarrow{F_s}(\theta) = \overrightarrow{F_{a1}}(\theta) + \overrightarrow{F_{d1}}(\theta) \qquad 36 \le \theta \le 72 \qquad (4.9)$$

$$\overrightarrow{F_s}(\theta) = \overrightarrow{F_{d1}}(\theta) + \overrightarrow{F_{b1}}(\theta) \qquad 72 \le \theta \le 108 \qquad (4.10)$$

$$\overrightarrow{F_s}(\theta) = \overrightarrow{F_{b1}}(\theta) + \overrightarrow{F_{e1}}(\theta) \qquad 108 \le \theta \le 144 \qquad (4.11)$$

$$\overrightarrow{F_s}(\theta) = \overrightarrow{F_{e1}}(\theta) + \overrightarrow{F_{c1}}(\theta) \qquad 144 \le \theta \le 180 \qquad (4.12)$$

Knowing the fundamental phase MMFs from equation (4.7), the stator MMF is calculated by substituting equation (4.7) into equations (4.8) – (4.12) as

$$\overrightarrow{F_s}(\theta) = F_{a1,peak}(\theta)\angle -36^0 + F_{c1,peak}(\theta)\angle 0^0 \qquad 0 \le \theta \le 36 \qquad (4.13)$$

$$\overrightarrow{F_s}(\theta) = F_{a1,peak}(\theta)\angle -36^0 + F_{d1,peak}(\theta)\angle -72^0 \qquad 36 \le \theta \le 72 \qquad (4.14)$$

$$\overrightarrow{F_s}(\theta) = F_{d1,peak}(\theta)\angle -72^0 + F_{b1,peak}(\theta)\angle -108^0 \qquad 72 \le \theta \le 108 \qquad (4.15)$$

$$\overrightarrow{F_s}(\theta) = F_{b1,peak}(\theta)\angle -108^0 + F_{e1,peak}(\theta)\angle -144^0 \qquad 108 \le \theta \le 144 \qquad (4.16)$$

$$\overrightarrow{F_s}(\theta) = F_{e1,peak}(\theta)\angle -144^0 + F_{c1,peak}(\theta)\angle 0^0 \qquad 144 \le \theta \le 180 \qquad (4.17)$$

The resultant stator MMF of equations (4.13) – (4.17) can be represented by a resultant space phasor as follows [Mohan (2001)]:

$$\overrightarrow{F_s} = F_s\angle\theta_{F_s}, \qquad (4.18)$$

where F_s is the space phasor magnitude and θ_{F_s} is the orientation of the space phasor. The space phasor $\vec{F}_S(\theta)$ represents the MMF distribution in the air gap according to rotor position θ due to all the currents in the five phase windings.

Based on equation (4.18), the amplitude and angular position of the resultant space phasor with the square field current waveform is as shown in Figure 4.9. In this case F_{j1peak} of equation (4.5) is taken as F_{j1peak} = 39. There is no special reason for choosing the 39, as the focus of this section is more on the smoothness of the rotating MMF than on the magnitude of the rotating MMF. Note from the figure that the MMF plot with square field current only does not give a continuous smooth rotating MMF, instead it gives a discontinuous (discrete) rotating MMF.

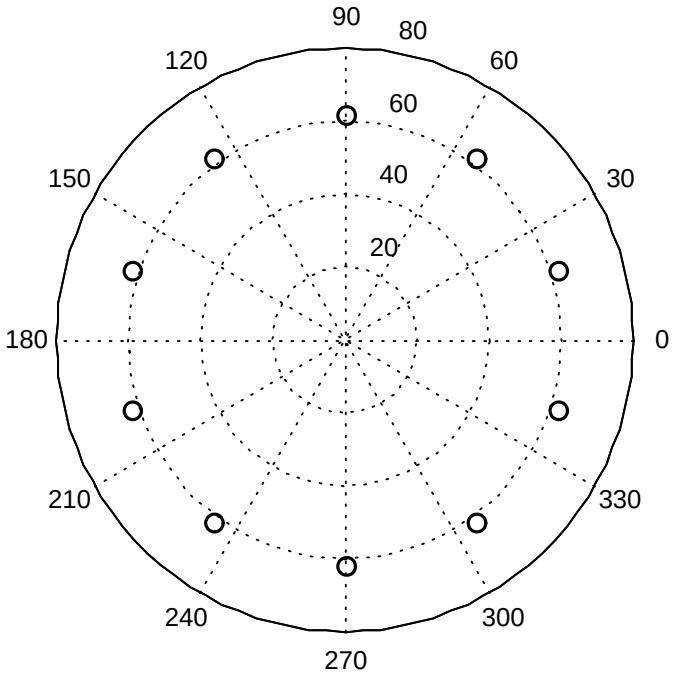

Figure 4.9: Magnitude and angular position of the resultant space phasor MMF with square field current waveform and continuous rotor movement.

(b) Trapezoidal current waveform

Just like for the square current waveform, the trapezoidal current waveforms with field current only are as shown in the Figure 4.10. Unlike the square field current waveform, the trapezoidal field current is not constant with rotor movement but is of the triangular shape as shown in the figure. Noticeable from the current waveforms is that unlike in the square current waveform where two phases are always active, at certain rotor positions only one phase is active; for instance at position zero only phase C is active. The MMF analysis for the

trapezoidal field current waveform is also carried out both graphically and analytically as described in the next sections.

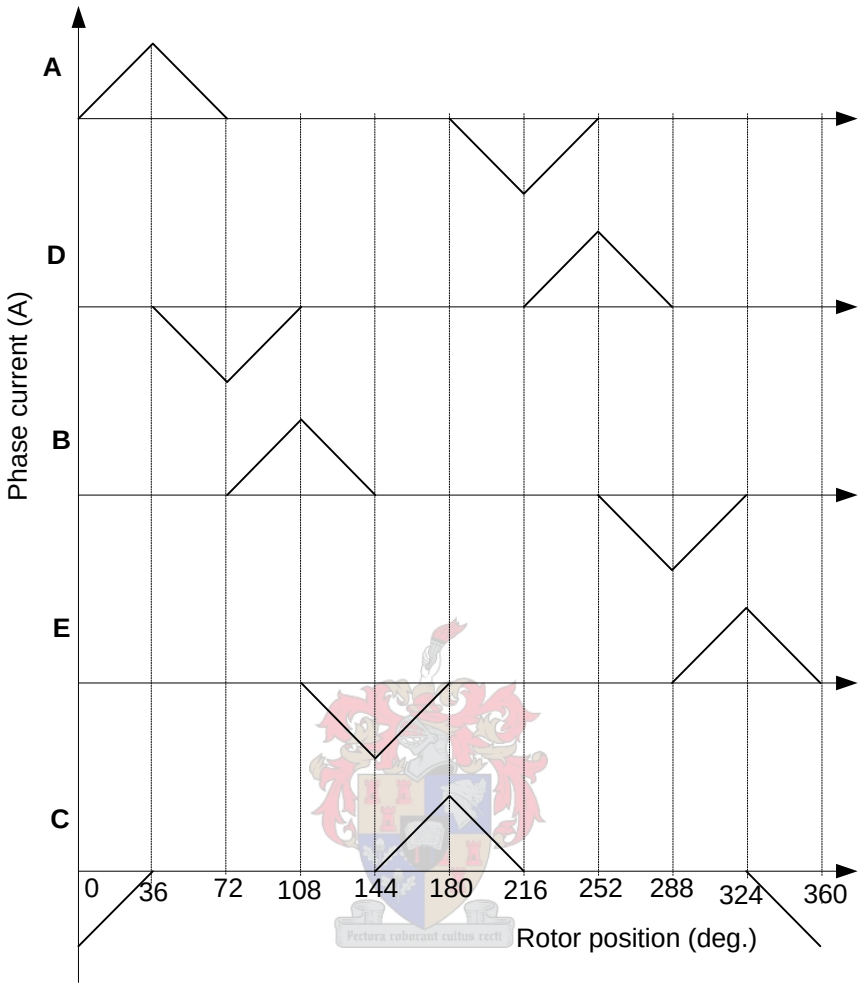

Figure 4.10: 5-phase trapezoidal current waveforms with field current only.

(i) Graphical Method

The same procedure as for the square current waveform is applied to determine graphically the resultant MMF with the trapezoidal field current. The results for three different rotor positions are as shown in the Figure 4.11. It is clear that unlike with the square field current waveform, the angular position of the resultant MMF follows the rotor d-axis, i.e. the MMF space phasor is always in phase with the rotor d-axis.

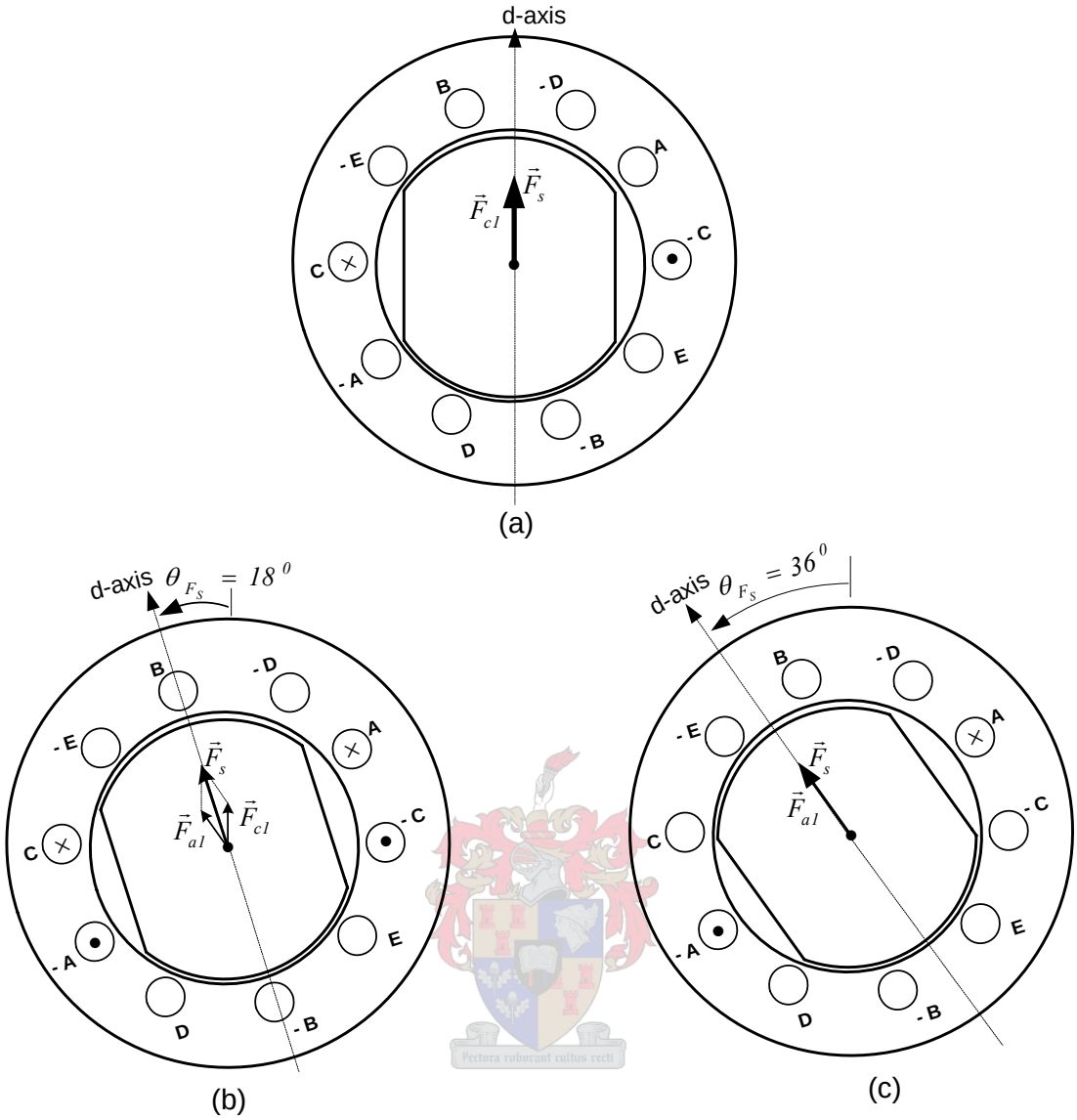

Figure 4.11: Graphical representation of rotating MMF at three rotor positions namely: (a) 0^0, (b) 18^0 and (c) 36^0 with the trapezoidal field current waveform.

(ii) Analytical Method

The same procedure as for the square current waveform is applied to determine the resultant space phasor MMF analytically. The stator space phasor MMF, $\overrightarrow{F_s(\theta)}$, in the airgap at different rotor positions with the trapezoidal field current waveform is described by the same equations (equations (4.8)- (4.18)) as with the square current waveform. The only difference is that F_{j1peak} of equation (4.5) is no longer a constant but varies with rotor position θ as the current i_j varies. The magnitude and angular position of the resultant space phasor MMF with continuous rotor movement is as shown in Figure 4.12. It can be observed that the rotating

MMF with the trapezoidal field current waveform is smooth and continuous but the amplitude varies slightly.

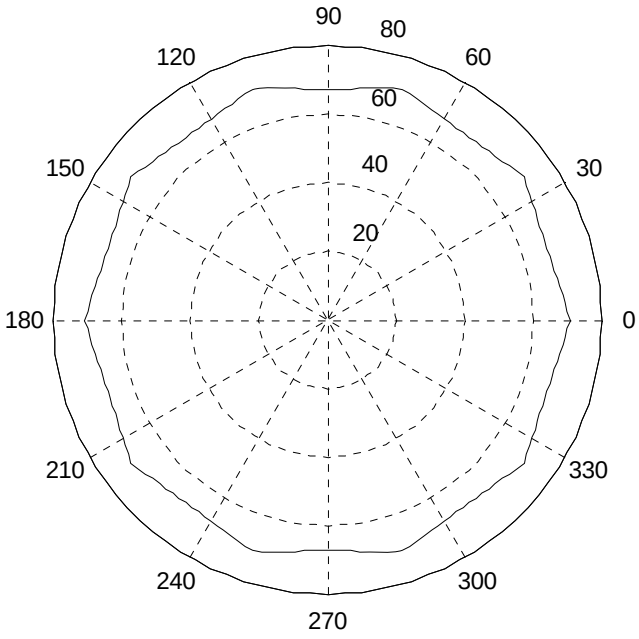

Figure 4.12: Magnitude and angular position of the resultant space phasor MMF with trapezoidal field current waveform and continuous rotor movement.

(c) Half – sinusoidal current waveform

The same analysis as for the square and trapezoidal field current waveforms is carried out for the half sinusoidal current waveform, but for the latter, the analysis is done only analytically. The 5-phase field current waveforms for the half-sinusoidal current waveforms are as shown in Figure 4.13.

The resultant space phasor MMF plot for the half-sinusoidal field current waveform is as shown in Figure 4.14. It is noticeable from the figure that the space phasor MMF plot is continuous with rotor movement but there is a fairly large ripple in the amplitude as compared to that with the trapezoidal field current waveform.

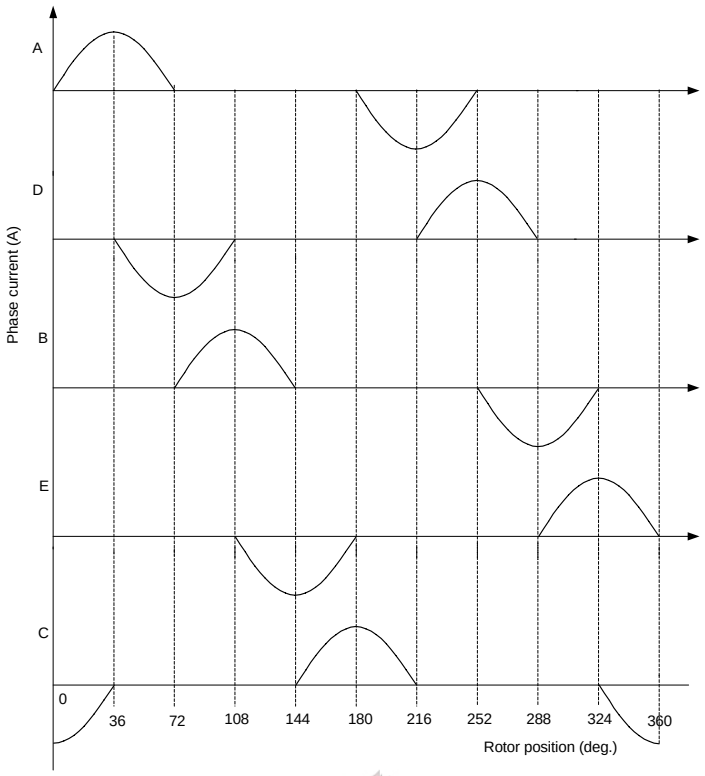

Figure 4.13: 5-phase half-sinusoidal current waveforms with field current only.

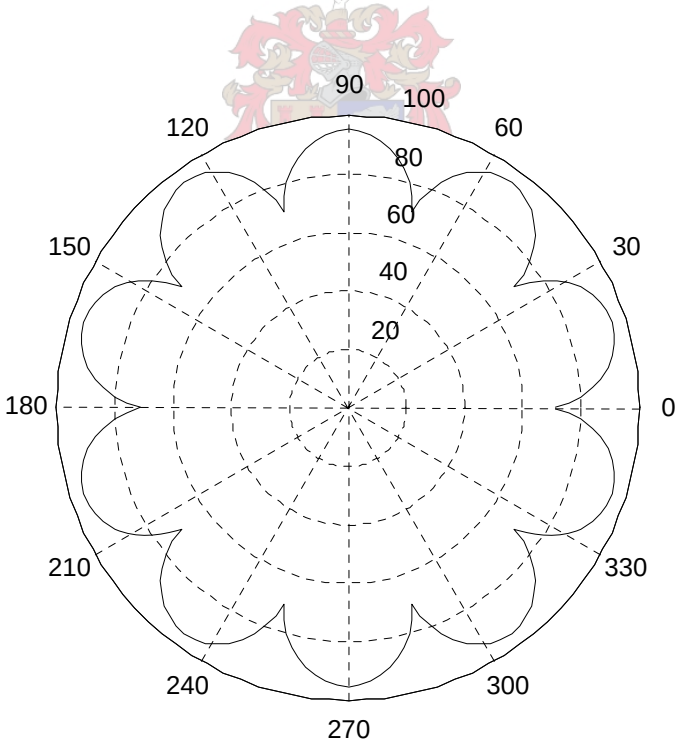

Figure 4.14: Magnitude and angular position of the resultant space phasor MMF with half-sinusoidal field current waveform and continuous rotor movement.

4.4 Derivation of torque equation for RDCM

As the study of this thesis is mainly focussed on the torque performance of the RDCM, it is worth formulating an equation that can be used to calculate the torque of the RDCM. This analytical calculation of torque can then be compared to or used to verify the torque calculated from finite element analysis by the Maxwell stress tensor method.

As in classical brush dc machine analysis the torque of the RDCM can be expressed by using Lorentz's law as follows:

$$T = B_g \, l \, I \, r_g, \tag{4.19}$$

where B_g is the airgap flux density, l is the stack length of the machine, I, is the total conductor current and r_g is the radius in the middle of the airgap between the salient pole and the stator. In deriving the torque equation of the RDCM, the airgap flux density is assumed to be a maximum above the salient pole and zero in between the salient pole poles as shown in Figure 4.15. The airgap flux density shown in Figure 4.15(b) ignores the armature reaction effect. This effect can only be ignored with good rotor design where the torque current does not affect the flux density waveform in the airgap between the salient pole and the stator.

The total conductor current, I, of equation (4.19) can be expressed as follows:

$$I = \frac{I_T}{n_a} z \, q \, m_T \, 2p, \tag{4.20}$$

where q is the number of slots per pole per phase, z is the number of the conductors per slot, m_T is the number of active torque phases and n_a is the number of parallel paths. With the airgap flux density over the salient rotor pole, the flux per pole, φ_p, can then be expressed as follows:

$$\begin{aligned} \varphi_p &= B_g \, Area \\ &= B_g \, l \, r_g \, \theta_p, \end{aligned} \tag{4.21}$$

where θ_p is the rotor pole arc angle in mechanical degrees. With B_g from equation (4.21) and I from equation (4.20), the torque equation (4.19) can be expressed as follows:

$$\begin{aligned} T &= \left(\frac{\varphi_p}{l \, r_g \, \theta_p} \right) l \left(\frac{I_T}{n_a} z \, q \, m_T \, 2p \right) r_g \\ &= k \, m_T \, \varphi_p \, I_T, \end{aligned} \tag{4.22}$$

where k is the machine constant and is given by

$$k = \frac{2\,z\,q\,p}{\theta_p\,n_a}. \tag{4.23}$$

It is noticeable from equation (4.22) that just like for a brush DC machine the torque equation of the RDCM is the product of the flux per pole and the torque current. Similarly, just like in a brush DC machine the induced voltage in the torque producing coils can be expressed as follows:

$$e_n = k\,\varphi_p\,\omega_r \tag{4.24}$$

It is also worth mentioning that the above proposed torque equation of the RDCM is only valid when the torque producing phases are beneath the salient pole.

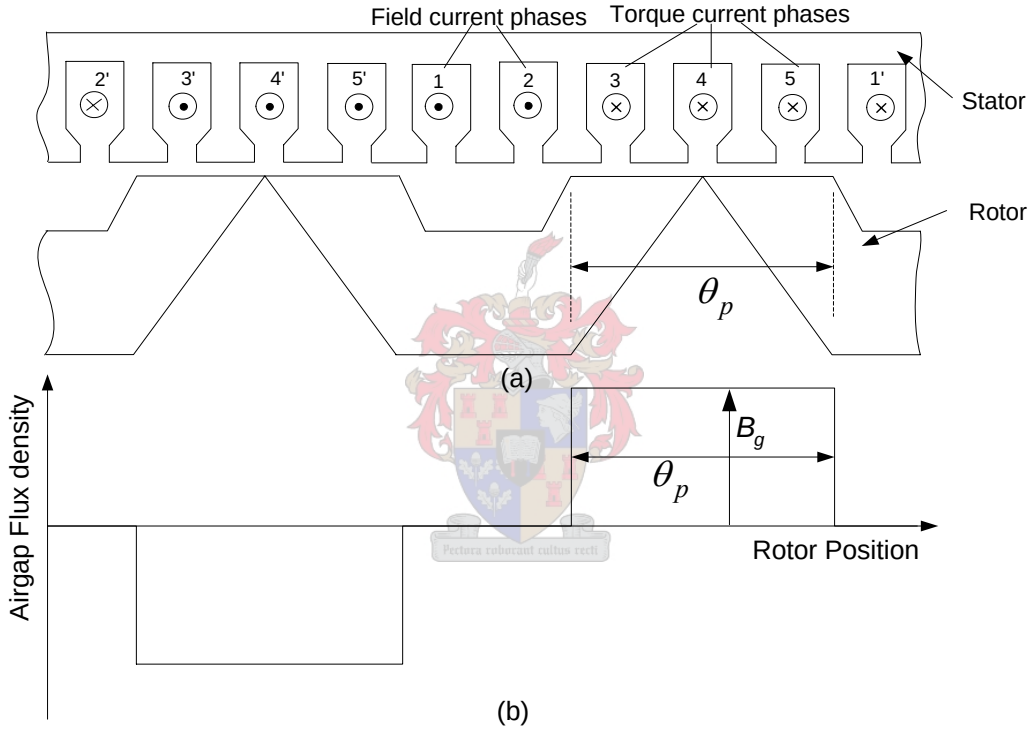

Figure 4.15:(a) 5-phase RDCM structure with (b) ideal airgap flux density waveform.

For a given torque current, I_T, given number of torque producing phases, m_T, and the machine constant, k, the torque of an RDCM can be determined from equation (4.22) provided the flux per pole is known. The flux per pole, φ_p, can be determined from the product of the average flux density per pole, B_g, and the area of the salient pole as given by equation (4.21). However, the average flux density is unknown, but it can be determined directly from the finite element analysis as described in appendix A.3. Because for this thesis only skewed machines are considered, the average flux density with skew taken into account has to be calculated. This is done by averaging the flux densities of n-sub-machines (where n = 5 from the previous chapter) as given by

$$B_g(\theta) = \frac{1}{5}\sum_{n=1}^{5} B_{gn}(\theta), \tag{4.25}$$

where $B_{gn}(\theta)$ is the radial component of the airgap flux density of the *n-th* unskewed machine and is determined by equation (A.6). The ideal average flux density across a pole with skew taken into account over the axial length of the machine, l, is shown in Figure 4.16. The average flux density as compared to the ideal flux density shown in Figure 4.15(b) has a width that is greater than the rotor pole arc; this is due to the combined effect of skewing and fringing. The rotor pole arc angle with skew taken into account, θ_{ps}, can be expressed as follows:

$$\theta_{ps} = \theta_p + \beta, \tag{4.26}$$

where β is the slot-pitch angle.

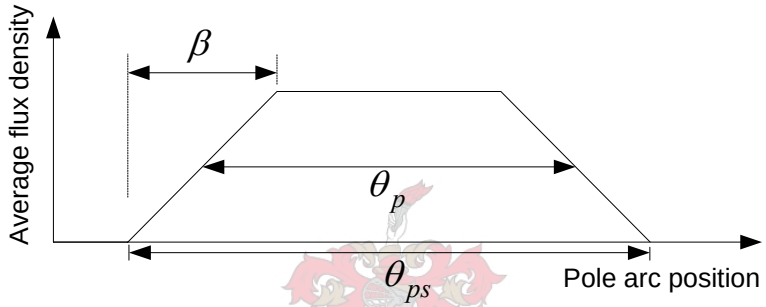

Figure 4.16: Ideal average flux density across a rotor pole with skew taken into account [Hendershot (1994)].

It is worth mentioning that the average flux density used in the torque calculation is calculated under load conditions, i.e., with both field and torque currents active, so as to cater for the cross-coupling effect. The method proposed above is used in the next chapter to calculate the torque performance of the RDCMs.

4.5 Summary

In this chapter, the operation principle of the reluctance DC machine was developed based on the working principle of the permanent magnet DC machine. Two special current waveforms namely: half-sinusoidal and trapezoidal current waveform, were developed for the RDCM in addition to the well-known square current waveform. As criteria for selecting the best current waveform for the RDCM, the analysis of the rotating airgap MMF for the three current waveforms was performed both graphically and analytically. Based on this criterion, it was shown that the trapezoidal current waveform was the best for the RDCM drive in the sense that it resulted in a continuous smooth rotating MMF with continuous rotor movement. The

torque equation of the RDCM was derived based on the Lorentz law; this equation turned out to be similar to that of brush dc machine. This torque equation will be used in the next chapter to calculate the torque of the RDCMs so as to verify the FE Maxwell stress tensor calculated torque.

CHAPTER 5 Torque performance of Reluctance DC machines

The main goal of this chapter is to determine the torque performance of the optimally designed RDCMs by the use of finite element analysis. Just like for the sinusoidal RSMs described from chapter 3, RDCMs are also optimally designed for maximum torque at the same copper losses and volume so that it is possible to make a fair comparison between the sinusoidal RSMs and RDCMs. The torque performance of the optimally designed 5-phase RDCM with the square current waveform is compared to that of the machine with the trapezoidal current waveform so as to validate the selection of the trapezoidal current waveform. The torque performance of RDCMs with the trapezoidal current waveform is also extended to the 6-phase RDCM with different rotor structures. The 6-phase RDCM is analysed with different rotor structures so as to study effect of the rotor structure on the armature reaction effect of the machine. In addition to the above, torque performance of the machines are calculated by the use of the derived analytical torque equations from the previous chapter. The torque calculated by the analytical torque equations is then compared with the FE calculated torque.

5.1 Design Optimisation of the 5 – phase RDCM

This section describes the design optimisation of the 5-phase CR-rotor RDCM with two current waveforms. The current waveforms are the square current waveform and the trapezoidal current waveform. Most importantly, the torque performance of the optimum RDCMs is obtained and compared with that of the 5-phase + 3rd RSM. Furthermore, the investigation of the current waveforms is carried out by the analysis of the average airgap flux density with rotor position.

5.1.1 Optimisation variables

The aim of the design optimisation of the RDCMs, just like for the sinusoidal machines, was to maximise without any constraints the torque per copper losses per given stack volume. Also what should be noted is that the same optimisation algorithm was used, that is the Powell method, which is described in the previous chapters. The expression for the copper losses of a 5-phase machine is given by

$$P_{cu} = 5\, I_{rms}^2\, r_s \tag{5.1}$$

where the *rms*-currents for the square and the trapezoidal current waveforms are given by equations (5.2) and (5.3) respectively.

$$I_{rms} = \frac{1}{\sqrt{5}}\sqrt{(2I_F^2 + 3I_T^2)} \tag{5.2}$$

$$I_{rms} = \frac{1}{\sqrt{15}}\sqrt{(2I_F^2 + 5I_T^2)} \tag{5.3}$$

To be able to optimise the RDCMs under the same copper losses, the torque current, I_T, is expressed in terms of field current and copper losses. The torque currents for the square and the trapezoidal current waveform are given by equations (5.4) and (5.5) respectively. The torque currents for the square and trapezoidal current waveform are derived by substituting the corresponding equations (5.2) or (5.3) into equation (5.1).

$$I_T = \sqrt{\frac{P_{cu} - 2I_F^2 r_s}{3r_s}} \tag{5.4}$$

$$I_T = \sqrt{\frac{P_{cu} - 2/3 I_F^2 r_s}{5/3 r_s}} \tag{5.5}$$

In equations (5.4) and (5.5), P_{cu} is the constant copper losses in the optimisation and r_s is the per phase stator resistance calculated according to, amongst other things, the slot dimensions and conductor insulations. The field current is included as one of the optimisation variables for the machine. In addition to the field current, the following machine dimensions are also included as optimisation variables; tooth width, t_w, stator yoke height, s_{yh}, stator inner diameter, d_i, rotor cut-out depth, r_c, and rotor cut-out angle, σ. The cross sections of a quarter of the rotor and the stator of the 5-phase RDCM under investigation, with the optimisation dimensions are as shown in Figures 5.1(a) and (b) respectively.

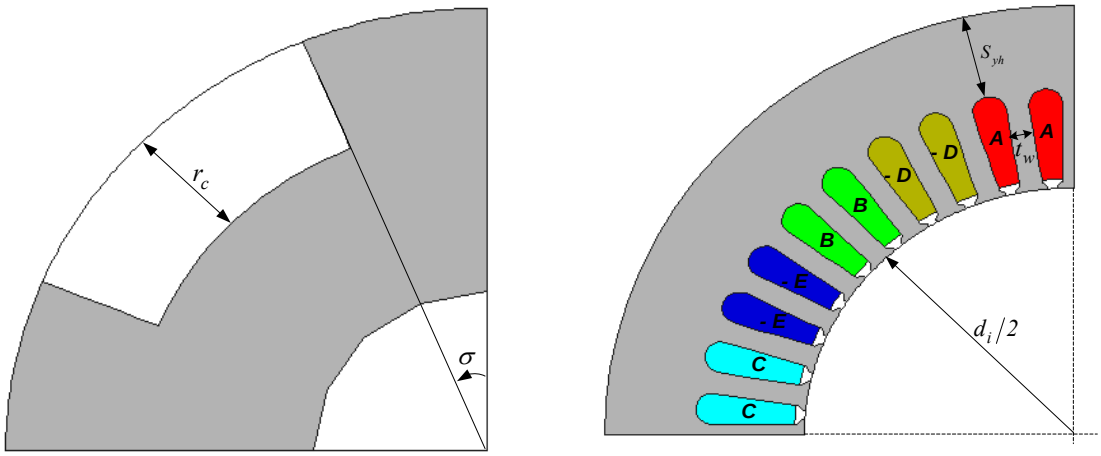

(a) (b)

Figure 5.1:(a) Structure (quarter section) of the rotor and (b) structure (quarter section) of the stator for the 5-phase RDCM.

As was discussed under sinusoidal machines, average (fundamental) torque is maximised in the design optimisation at 2.5 per unit load. For this study, the optimisation is carried out at a certain rotor position for both the RDCM with the square current waveform and the one with the trapezoidal current waveform. With the optimisation algorithm, the FE then calculates the torque with skew taken into account. With the field current and the machine dimensions as optimisation variables, the FE calculates the torque current, I_T, from equations (5.4) and (5.5) depending on the current waveform. From the field and torque currents together with the machine dimensions, the FE analysis then calculates torque. By the use of the Powell optimisation algorithm, the optimisation variables are varied till the maximum torque is reached. With the optimum field and torque current for the particular machine, the ratio of field to torque current (I_F/I_T) is then calculated.

5.1.2 Optimisation results

The optimisation results of the 5-phase RDCMs with the different current waveforms are as shown in Table 5.1. The optimisation results of the 5-phase +3rd RSM with CR-rotor by Rakgati (2006) from chapter 3 are also included for comparison purposes.

Table 5.1: Optimisation results for the 5-phase RDCM with different current waveforms and 5-phase + 3rd RSM.

Parameter	Square	Trapezoidal	5-phase+3rd RSM [Rakgati (2006)]
t_w (mm)	8.2	8.4	8.2
s_{yh} (mm)	32.6	30.6	32.9
d_i (mm)	195.5	196.0	194.3
r_c (mm)	25.3	24.4	25.1
$\sigma = \theta_p / 2$ (°)	15.4	14.7	15.6
α (°)	-	-	56.7
I_F/I_T	0.67	1.42	-

It is noticeable from the optimisation results of Table 5.1 that the optimum dimensions of both the machines are almost the same. One more thing that stands out from the optimum dimensions is the relatively small rotor pole angle, σ, so as to reduce the armature reaction effect. The effect of the pole arc angle on the cross-coupling effect has been shown for the sinusoidal machines in chapter 3. If it were not for the armature reaction effect of the machine

that is dealt at a later stage in the chapter, one would expect the rotor pole arc angle of the 5-phase RDCMs as from equation (4.3) to be as follows:

$$\begin{aligned}\theta_p &= \theta_\tau \left(m_T / \left(m_F + m_T\right)\right) \\ &= 90 * \left(3/5\right) \\ &= 54^0\end{aligned}$$

This then corresponds to a rotor pole cut-out angle, σ, of 27^0. When comparing the optimum rotor pole cut-out angles for the 5-phase RDCMs, it can be seen that the machines have a severe armature reaction effect.

As verification of the design optimisation for the RDCMs, the effect of the amplitude ratio of field to torque current on the torque performance of the machine with the trapezoidal current waveform was investigated at 1 per unit load and the results are shown in Figure 5.2. The amplitude ratio of field to torque current in RDCMs is analogous to current angle in sinusoidal machines. The torque for the RDCM increases with an increase in the amplitude ratio of field to torque current upto optimum amplitude ratio and drops again. It is also noticeable from the figure that the amplitude ratio at 1 per unit copper losses is almost equal to the optimum amplitude ratio of field to torque current from the design optimisation, i.e., at 2.5 per unit load.

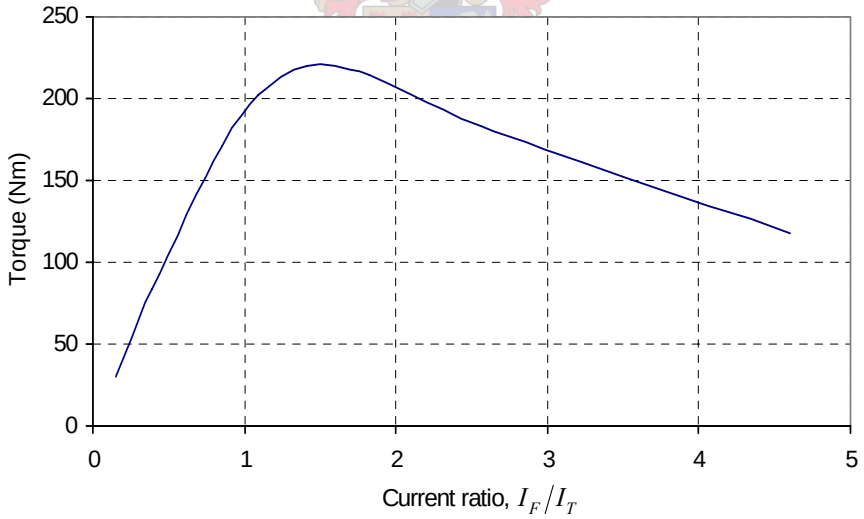

Figure 5.2: Torque versus current ratio for the 5-phase RDCM at 1.0 per unit copper losses.

5.1.3 Torque performance

The torque performance at 1 per unit copper losses of the skewed optimum designed 5-phase RDCMs with the square and the trapezoidal current waveforms in comparison with the 5-phase + 3rd RSM are as shown in Figure 5.3. A summary of the average torque performance and the torque ripple of the machines are given in Table 5.2. It is noticeable from Table 5.3

that the optimum designed 5-phase RDCM with the trapezoidal current waveform yields a higher average torque and less torque ripple than the 5-phase RDCM with square current waveform. The optimum designed RDCM with the trapezoidal current waveform results in an average torque, which is 3% higher than that of the optimum machine with the square current waveform. Even though the optimum designed 5-phase RDCM with the trapezoidal current waveform outperforms the one with the square current waveform, the optimum designed 5-phase +3rd RSM still outperforms the optimum designed 5-phase RDCM with the trapezoidal current waveform by 4%. More importantly, as from Table 5.2, the torque ripple of the optimum designed 5-phase RDCM with the trapezoidal current waveform is 16% lower than that of the optimum machine with the square current waveform. The torque performance in terms of average torque and torque ripple of the optimum designed 5-phase RDCM with the trapezoidal current waveform in comparison with the machine with the square current waveform further validates the selection of the trapezoidal current waveform for the RDCMs.

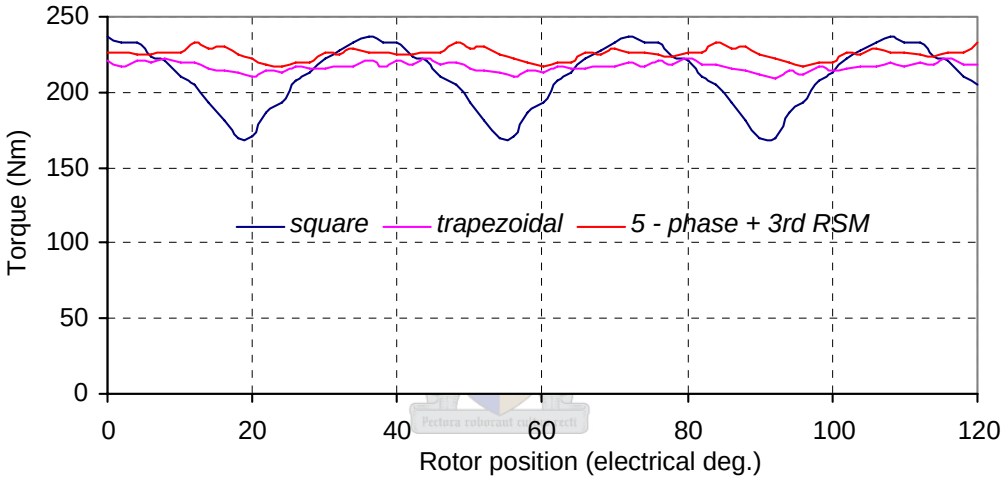

Figure 5.3: Torque versus rotor position for the skewed optimum designed 5-phase RDCM with two different current waveforms and that of the optimum designed 5-phase + 3rd RSM.

Table 5.2: Average torque for the optimum designed 5-phase RDCMs with different current waveforms and 5-phase + 3rd RSM.

	Square	Trapezoidal	5-phase +3rd RSM
Torque (Nm)	209	215.7	224.8
Torque (p.u.)	0.930	0.959	1.0
Torque ripple (%)	19	3	3.3

5.1.4 Remarks on optimum current waveform

Even though the trapezoidal current waveform has been shown to be far much better than the square current waveform for the 5-phase RDCMs, the major hindrance of the optimum phase current waveform as observed from Figure 5.4 is the high peaks of the current waveform. The disadvantage of the high peaks is that the converter modules that have to be used to drive the machine have to be able to handle high peaks. The higher peaks would then result in a more expensive converter. In addition to the high peaks of the current waveform, it can also be observed that comparing the optimum active part of the rotor (rotor pole arc angle, θ_p) and the torque current conducting angle, θ_T, shows a greater reduction in the active part of the rotor. Assuming three torque coils active, the ratio (θ_p/θ_T) of the optimum rotor pole arc angle to the torque current conducting angle for this particular optimum 5-phase RDCM is given by

$$\frac{\theta_p}{\theta_T} = \frac{29.4}{54} = 0.54 \tag{5.6}$$

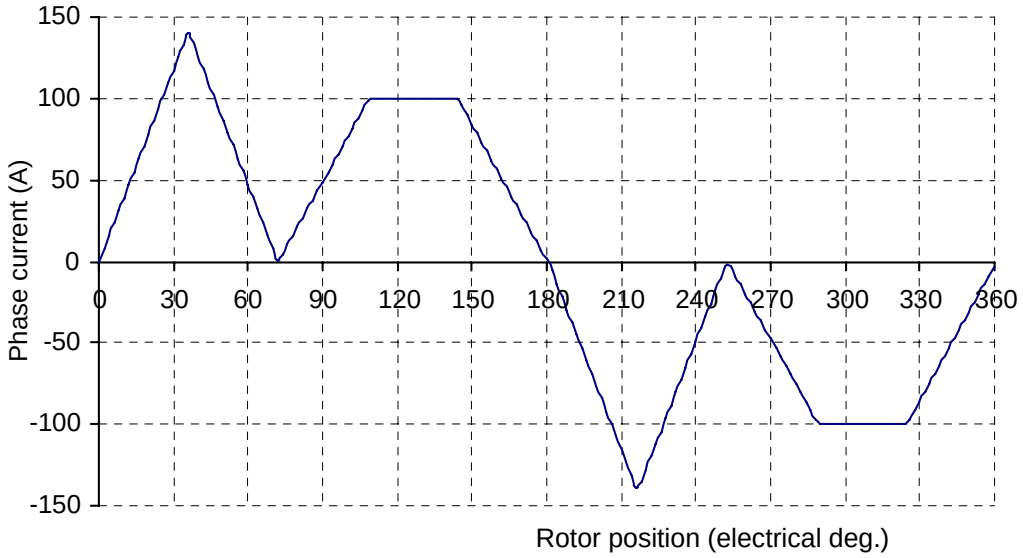

Figure 5.4: Optimum trapezoidal phase current for the 5-phase RDCM at 1 per unit copper losses.

In order to arrest the above problems posed by the optimum designed 5-phase RDCM, the investigation is extended to a 6-phase RDCM, which will be discussed later in the chapter. For the 6-phase RDCM the active optimum part of the rotor can be increased by modifying the ratio of the field to torque current conducting angle from 2/3 for the 5-phase RDCM to 3/3 for the 6-phase RDCM.

5.1.5 Flux density Analysis

In order to further investigate the effects of the current waveforms the average flux density as a function of airgap position with rotor movement was investigated. The investigation was carried out for both the square current waveform and the trapezoidal current waveform. Just like for the rotating MMF analysis in the previous chapter, the average flux density analysis was also carried out with only rated field current. The flux density in the air gap of the machine was determined by the use of finite element analysis. The finite element analytical method for determining the air gap flux density is described in appendix A.3.

Filtered average flux density and the unfiltered flux density as a function of airgap position is shown in Figure 5.5. The filtering is done by the use of matlab filtering tools [Butter – low pass filter]. As shown in the Figure, the filtering filters out the higher slot harmonics in the airgap flux density waveform.

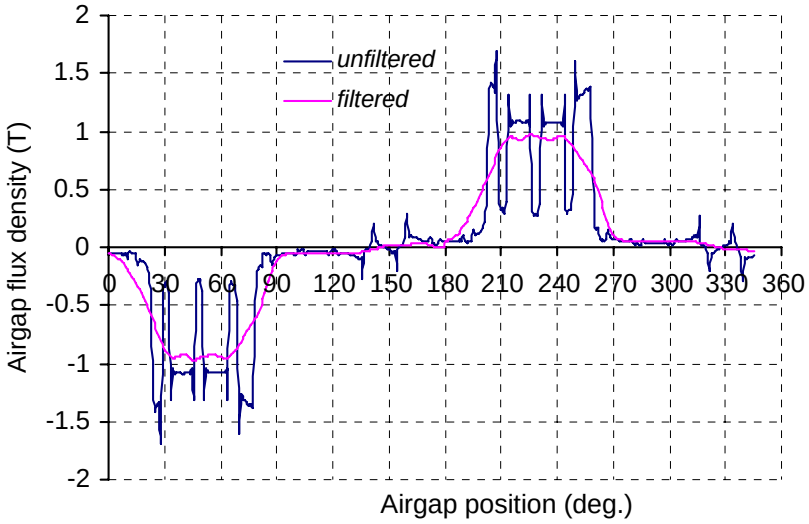

Figure 5.5: Filtered and unfiltered airgap flux density versus airgap position.

The overall averaged flux density versus airgap position of the machine with skew taken into account can be calculated by first determining the average airgap flux densities waveform of the 5-sub-machines and these are shown in Figure 5.6. The overall averaged flux density with skew can then be determined by averaging the flux densities of the 5 sub-machines as given by equation (4.25). From now onwards and for the rest of the thesis, only the averaged airgap flux density with skew taken into account will be considered.

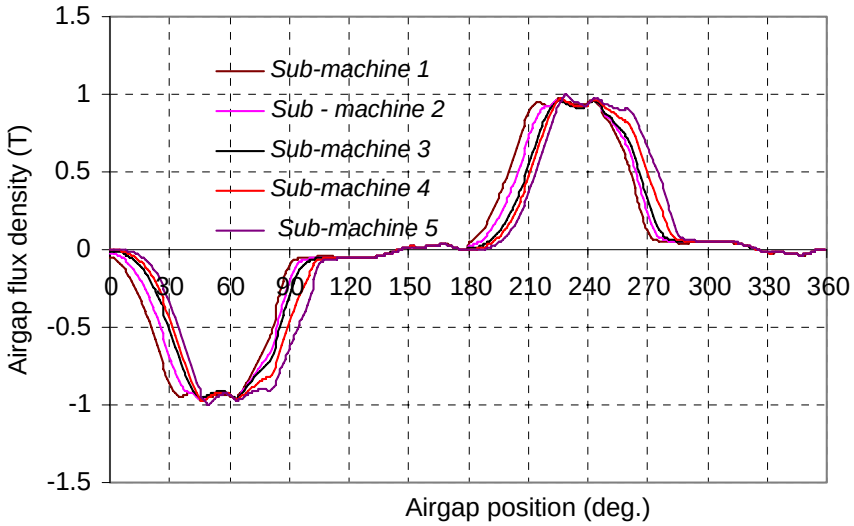

Figure 5.6: Averaged airgap flux density versus airgap position for the 5 sub-machines.

(a) Square current waveform

The airgap flux density waveform with rated square field current in the machine is as shown in Figure 5.7. With the average flux density taken to be the average of the plateau of the flux density waveform and the flux density position as the airgap position that coincides with the centre of the plateau, the average flux density as a function of flux density position can be as shown in Figure 5.8.

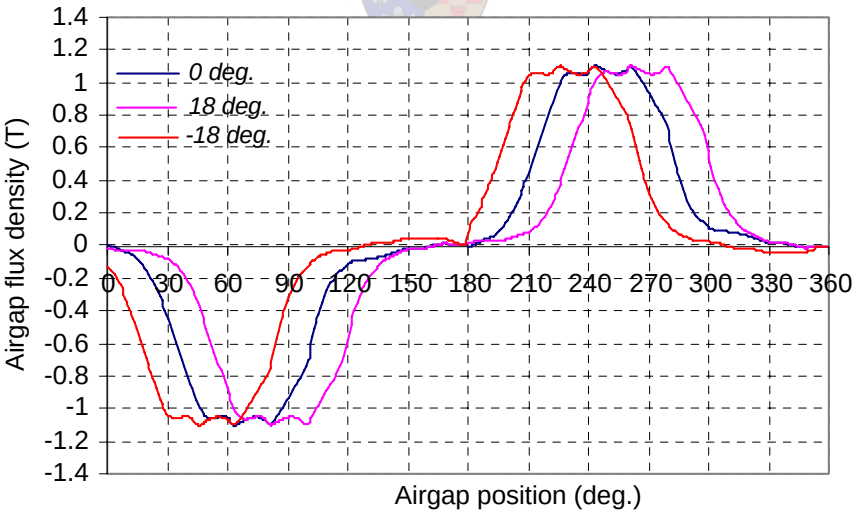

Figure 5.7: Flux density versus airgap position for different rotor positions with square field current.

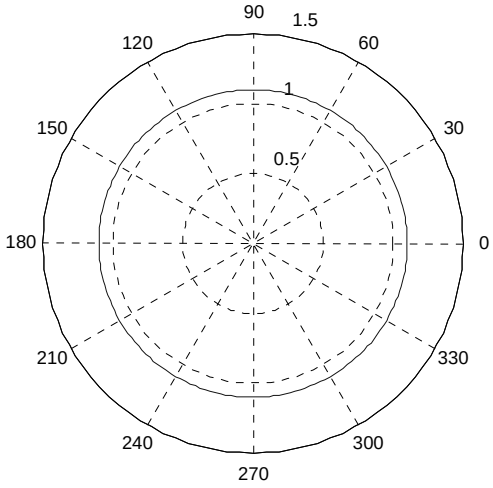

Figure 5.8: Flux density amplitude (average) versus flux density position with rotor movement and zero torque current for the square current waveform.

It is noticeable from Figure 5.8 that the average flux density as a function of flux density position for the square current waveform is smooth and continuous unlike for the rotating MMF for the square current waveform from the previous chapter. But with torque current (i.e. with both field and torque currents) has huge effect as shown in Figure 5.3. This is due to the fact that the optimum machine has a narrow rotor pole arc. The narrow pole arc results in a uniform field pattern as a function of rotor position as opposed to a bigger rotor pole arc.

(b) Trapezoidal current waveform

Just like for the square current waveform, the air gap flux density waveform as a function of airgap position for different rotor positions for the trapezoidal current waveform is as shown in Figure 5.9. With the flux density waveform for different rotor positions, the average flux density as a function of its position is as shown in Figure 5.10.

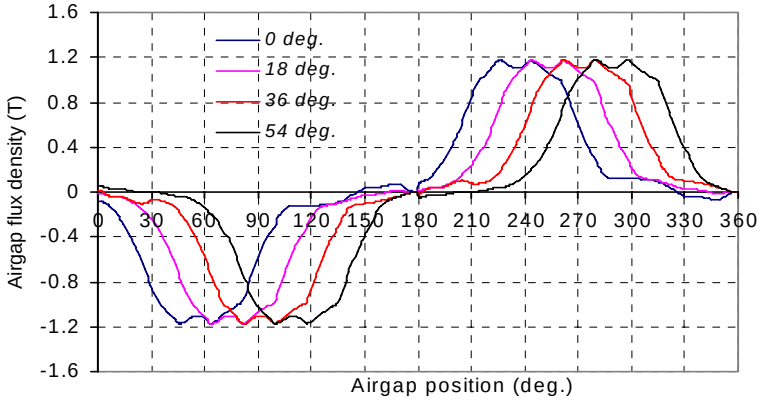

Figure 5.9: Flux density versus airgap position for different rotor positions with rated trapezoidal field current.

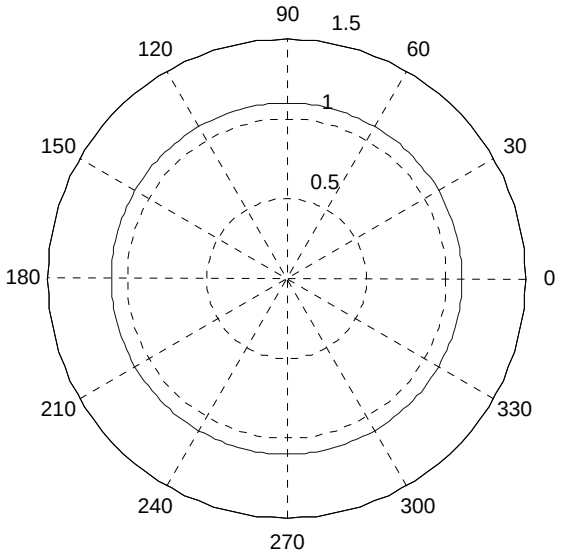

Figure 5.10: Flux density amplitude (average) versus flux density position with rotor movement and zero torque current for the trapezoidal current waveform.

The 5-phase RDCM with the trapezoidal current waveform just like for the one with the square current waveform results in a smooth and continuous average flux density with rotor movement. The smoothness and the continuity of the average flux density unlike that of the square current waveform tend to follow the shape of the rotating MMF for the machine as described in the previous chapter.

5.2 Six- Phase RDCM

As a detailed analysis of the flux density and the torque performance of the 5-phase RDCM with both the square and the trapezoidal current waveform was given in the previous section, these will not be repeated for the 6-phase RDCM. With the 5-phase RDCM, it has been shown that the machine with the trapezoidal current waveform is better than the square current waveform. The section focuses directly on the torque performance of the optimum 6-phase RDCM with the trapezoidal current waveforms and three different rotor structures.

5.2.1 Current waveforms of the 6-phase RDCM.

With the already proven trapezoidal current waveform for the RDCMs, the current waveform is extended to a 6-phase RDCM so as to arrest the problems posed by the optimum 5-phase RDCM which are the high peak currents and the less active area of the rotor. In addressing the problems, the 5-phase RDCM is modified to a 6-phase RDCM allowing for the ratio of the field to torque current conducting angles to be modified from 2/3 for a 5-phase RDCM to

3/3 for the 6-phase RDCM. The trapezoidal current waveform for the 6-phase RDCM is as shown in Figure 5.11. Based on the current waveform, the *rms*-current of the phase current is as follows:

$$I_{rms} = \sqrt{5/18\left(I_F^2 + I_T^2\right)}, \tag{5.7}$$

where I_T can be expressed in terms of copper losses just like for the 5-phase RDCM as given by

$$I_T = \sqrt{\frac{3P_{cu} - 5I_F^2 r_s}{5r_s}} \tag{5.8}$$

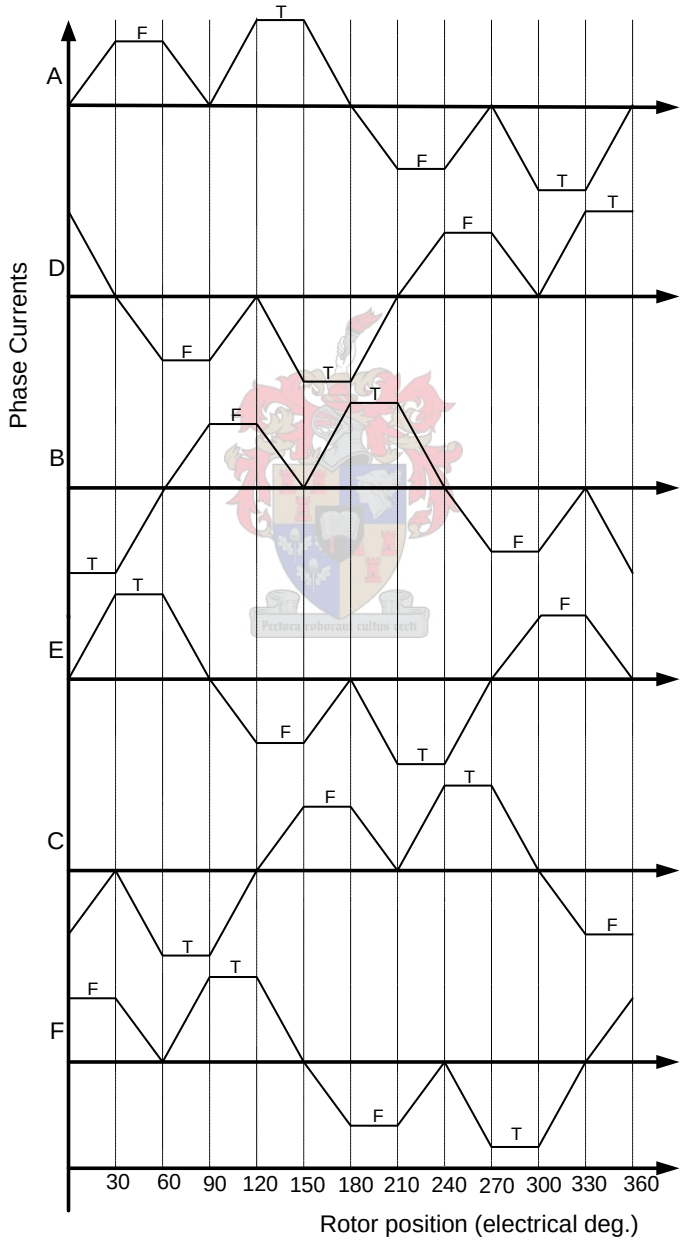

Figure 5.11: Trapezoidal current waveforms for the 6-phase RDCM.

5.2.2 Machine structure

For the 6-phase RDCM, three machines with the same stator structure and three different rotor structures are investigated. The quarter section of the stator structure showing the optimisation parameters and the winding layout of the machine is as shown in Figure 5.12. It is noticeable from the figure that the stator structure of the 6-phase RDCM under consideration is of the distributed type. The distributed type stator is preferred to the concentrated type because it is more suited for the rectangular pre-formed coils that are mostly used in the industry. The use of concentrated type winding as opposed to that of distributed type calls for a larger slot opening if rectangular preformed coils are to be used. The large slot openings result in much more torque ripple. Further investigation of torque ripple is beyond the scope of this thesis.

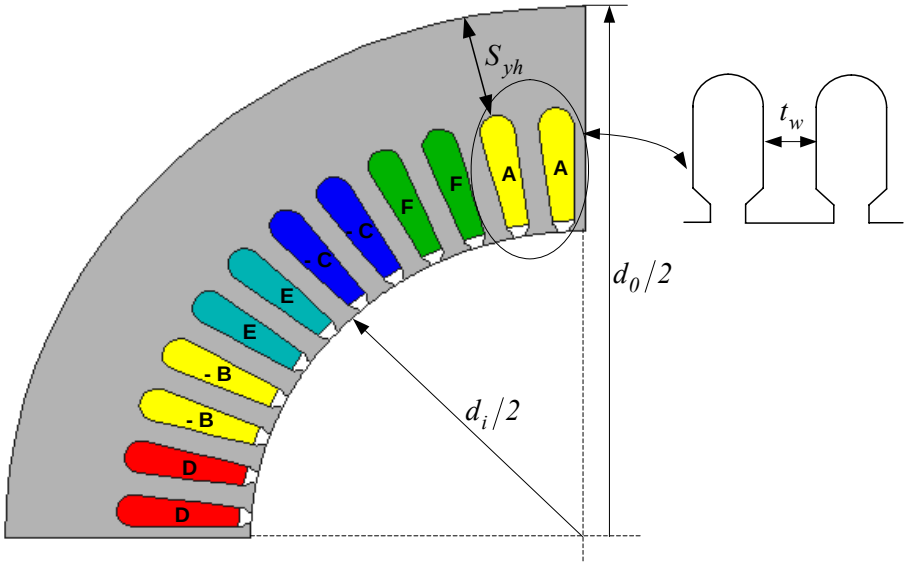

Figure 5.12: Structure (quarter section) of the 6-phase RDCM.

The rotor structures under investigation for the 6-phase RDCM are as follows: the salient pole rotor without slits, the salient pole rotor with straight pole arc and pole arc slits and the salient pole rotor with chamfered pole tips. For the rest of this chapter, the following convention is used to represent the three different rotor structures:

- Rotor 1 – salient pole rotor without slits.
- Rotor 2 - salient pole rotor with straight pole arc and pole arc slits.
- Rotor 3 – salient pole rotor with chamfered pole tips.

The rotor structures 2 and 3 are as shown in Figures 5.13 (a) and (b) respectively while rotor structure 1 is as shown in the previous section. Just like for the stator structure, the rotor structures are shown with their optimisation dimensions.

The design requirement for rotor 2 is to keep the rotor barrier pitch, b_p, larger than the stator slot pitch [Bomela (2002)]. This is to avoid high flux pulsations in the rotor iron segments. The idea of using slitted field poles to reduce the armature reaction effect is not new and was already proposed by Thompson (1904). For this particular 6-phase RDCM, ideally the rotor pole arc corresponds to three torque coils which translates to six slots so the number of rotor flux barriers is chosen to be greater than 6. In this particular case as shown in Figure 5.13(a), the number of rotor flux barriers were chosen to be 9.

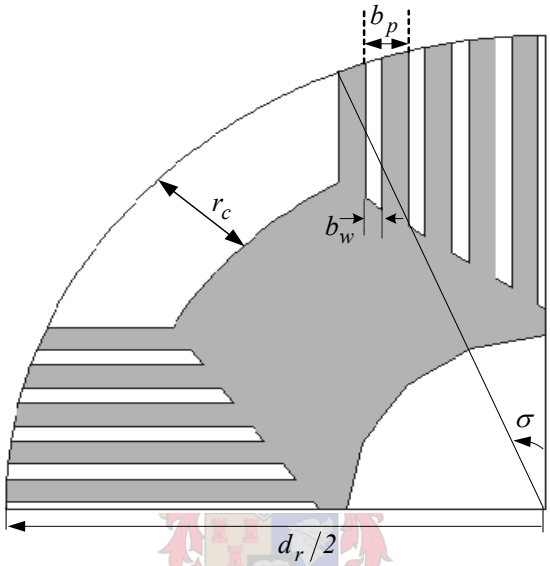

Figure 5.13(a): Rotor 2 structure (quarter section) for the 6-phase RDCM.

Just like for the rotor 2, the rotor 3 structure shows the important dimensions of the rotor that are referred in the design optimisation section. It was mentioned by Hindmarsh (1984) that salient pole rotor with chamfered pole tips can improve on the armature reaction effects in brush dc machines. The chamfering of the pole tips as shown in the figure, means that the pole tips of the pole face are spaced slightly further from the stator surface than the centre of the pole face. The chamfering of the pole tips of a pole face of the salient pole rotor DC machines increases the reluctance at the tips of the pole face and as such reduces the flux-bunching effect of armature reaction on the machine [Chapman (1991)].

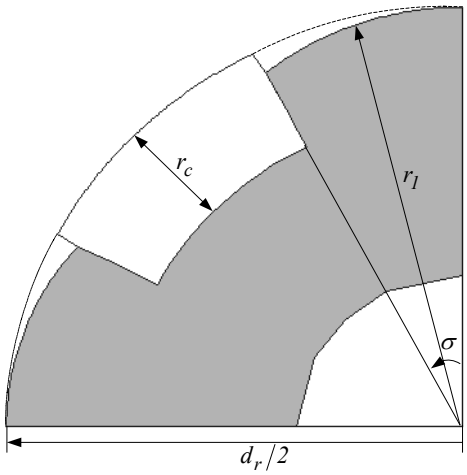

Figure 5.13(b): Rotor 3 structure (quarter section) of the 6-phase RDCM.

5.2.3 Design optimisation of the 6-phase RDCM

The above-mentioned 6-phase RDCMs with different rotor structures are optimised for maximum torque without constraints per copper losses per given stack volume just like for the 5-phase RDCMs. The only major difference is the optimisation dimensions. The optimisation dimensions of the stator are the same as for the stator of the 5-phase RDCM, while the optimisation dimensions of the rotor structures vary depending on the rotor structure. For instance for rotor 1, the rotor optimisation dimensions are the same as those for the 5-phase RDCM. For rotor 2, the optimisation dimensions of the rotor are as shown in Figure 5.13(a) and are the same as those of rotor 1 except for the barrier width and the barrier pitch. Hence, the ratio of the barrier width, b_w, to the barrier pitch, b_p, is used as an extra optimisation dimension for rotor 2. The ratio of the barrier width to the barrier pitch is defined as follows:

$$\psi = \frac{b_w}{b_p} \tag{5.9}$$

The ratio of the barrier width to the barrier pitch was investigated for axially laminated rotors by Miller (1991) and Matsuo (1994) and they found that an optimum ratio of 0.5 must be used. But in this thesis, the ratio will be optimised among other machine dimensions for normal (transverse) laminated machines. For rotor 3, as shown in Figure 5.13(b), the optimisation dimensions are the same as those of rotor 1 except for the pole tip radius, r_1. Hence, the pole tip radius is added as an extra optimisation dimension for the rotor 3. The rotor 2 shaft material is defined as non magnetic stainless steel. Just like for the optimisation of the 5-phase RDCMs, field current, I_F, was used as an extra optimisation parameter in addition to the machine dimensions for the 6-phase RDCMs. With the field current the torque current, I_T, follows from equation (5.8).

5.2.4 Optimisation Results

The optimisation results of the 6-phase RDCMs with three rotor structures are as given in Table 5.3. It can be observed from the optimum dimensions of Table 5.3 that the ratio of field to torque current (I_F/I_T) of the 6-phase RDCMs with different rotor structures is close to 1. This then implies that as anticipated, the optimum 6-phase RDCM has no high current peaks as compared to the optimum 5-phase RDCM. For instance, comparing the optimum 5-phase RDCM with salient pole rotor and the optimum 6-phase RDCM with the same rotor structure (rotor 1), as predicted the ratio of field to torque current (I_F/I_T) has improved from 1.42 to 0.87. It can also be further observed from Table 5.3 that even though the rotor cut out angle hasn't improved much from the optimum 5-phase RDCM to the optimum 6-phase RDCM, the active part of the rotor has improved. The active part of the rotor taking the example of rotor 1, as defined by the ratio (θ_p/θ_T) for the 6-phase RDCM is given by

$$\frac{\theta_p}{\theta_T} = \frac{32.4}{45} = 0.72 \tag{5.10}$$

Comparing the ratio (θ_p/θ_T) for the optimum 5-phase RDCM (from equation (5.6)) and that of the optimum 6-phase RDCM (from equation (5.10)), an improvement from 0.54 for the 5-phase RDCM to 0.72 for the 6-phase RDCM can be seen. Even though the rotor pole arc angle, θ_p, has not increased much from the 5-phase RDCM to the 6-phase RDCM, the active part of the pole arc has increased by 33%.

Table 5.3: Optimisation results of the 6-phase RDCMs with different rotor structures.

Parameter	Rotor 1	Rotor 2	Rotor 3
t_w (mm)	6.9	7.4	7.5
s_{yh} (mm)	32.4	32.4	31.2
d_i (mm)	196.1	189.7	198.4
r_c (mm)	23.3	41.3	24.9
σ (°)	16.2	15.3	15.6
I_F (A)	39	39.5	36.8
I_T (A)	45	44.9	43.1
I_F/I_T	0.87	0.88	0.85
Ψ	-	0.13	-
r_1 (mm)			99.1

The optimum different rotor structures for the 6-phase RDCMs are as shown in Figure 5.14. From the optimisation dimensions for the 6-phase RDCM with rotor 2, just like for rotor 1, the ratio of the rotor pole arc angle to the pole arc angle is 0.72. An observation that can be made about the optimum 6-phase RDCM with rotor 2 is that the number of rotor slits per rotor pole arc outnumbers the number of stator slots per rotor pole arc. For the optimum 6-phase RDCM with rotor 3, the difference between the optimum rotor 1 and rotor 3 can hardly be noticed because the optimum pole tip radius is very close to the rotor outer radius. Unlike for the optimum 6-phase RDCMs with rotor structures 1 and 2, the ratio (θ_p/θ_T) for the optimum 6-phase RDCM with rotor 3 is 0.69.

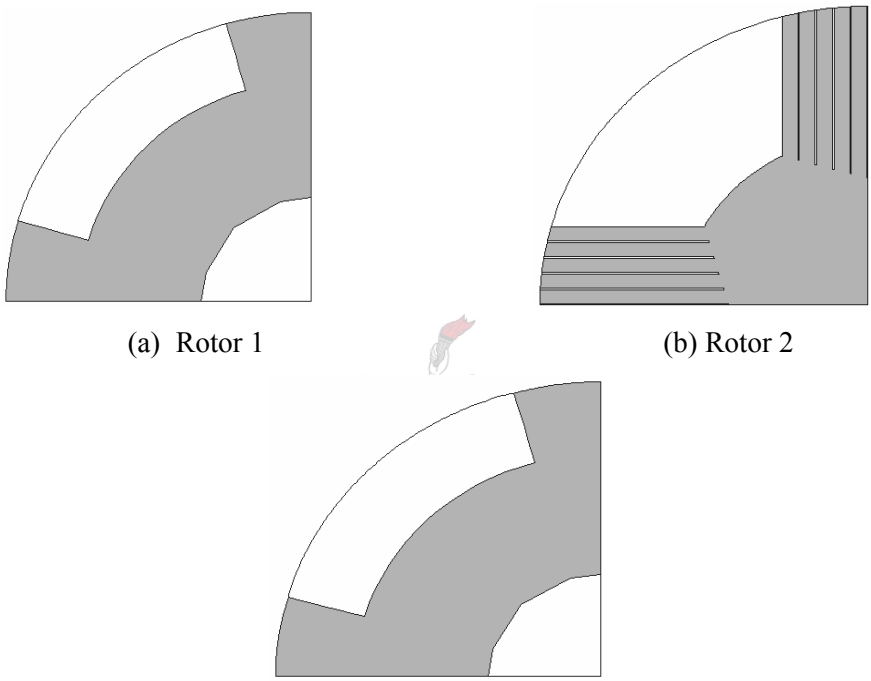

(a) Rotor 1 (b) Rotor 2

(c) Rotor 3

Figure 5.14: Optimum rotor structures for the 6-phase RDCM.

5.2.5 Torque performance

Under this section, the torque performances of the optimum 6-phase RDCMs are presented. The torque performances of the machines are presented by two torque calculation methods, both the FE Maxwell stress tensor calculation method and the analytical calculation method.

- *FE calculation method*

The FE torque profiles of the optimum 6-phase RDCM with three rotor structures is as shown in Figure 5.15. From the figure it can be observed that the average torque performance of the 6-phase RDCM with rotor 2 and the one with rotor 3 yields a higher torque when compared to

that of the machine with rotor 1. The summary of the average torque performances of the optimum designed 6-phase RDCMs at 1 per unit load with the different rotor structures is given in Table 5.4. It is noticeable from the table that the optimum designed 6-phase RDCMs with rotor 2 and the one with rotor 3 results in an increase of 6% in torque when compared to the optimum designed machine with rotor 1. This then probably indicates that the 6-phase RDCM with rotor 2 and the one with rotor 3 have a lower armature reaction effect when compared to the machine with rotor 1, and this will be verified in the next section.

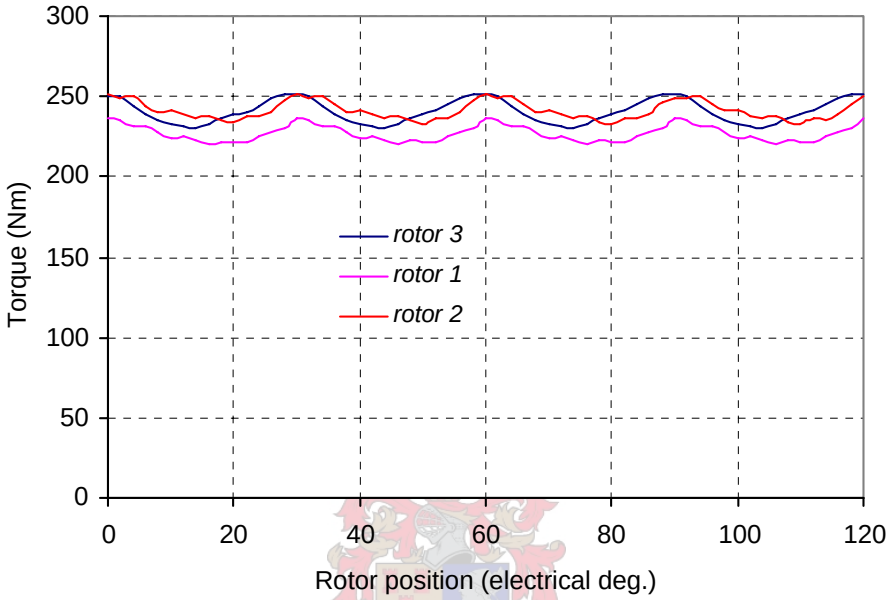

Figure 5.15: Torque versus rotor position for the optimum designed skewed 6-phase RDCM with different rotor structures for 1 per unit load.

Table 5.4. Average torque performance of the optimum designed 6-phase RDCMs with different rotor structures by the FE Maxwell stress tensor method.

	Rotor 1	Rotor 2	Rotor 3
Torque (Nm)	227	240.1	240.5
Torque (p.u.)	1.0	1.058	1.059

- *Analytical calculation method*

The analytical calculation method for the 6-phase RDCMs entails calculating the torque by the analytical torque equation of the RDCM derived in chapter 4. On an ideal case, the flux per rotor pole arc is due to the field current only but to allow for armature reaction effect in the calculations, the flux per rotor pole arc is taken with the machine excited with both field and torque currents [Hindmarsh (1984)]. The armature reaction effects of the 6-phase RDCMs are illustrated further in the next section.

The 6-phase trapezoidal current waveforms described earlier in the chapter show that the number of field and torque phase windings active alternates from two to three depending on the rotor position. But as clearly mentioned from the previous chapter, the proposed analytical torque equation is only valid when the rotor pole arc covers the active torque phase windings. In this particular case because of the optimum narrow rotor pole arc, this is only so when two torque phase windings are active. But when three torque phase windings are active, the optimum rotor pole arc does not cover all the torque phase windings. Based on the above facts about the 6-phase RDCM with the trapezoidal current waveform, the torque equation (4.22) can then be modified to cater for both the case when two torque phase windings are active and also for when three torque phase windings are active as follows:

$$T = \xi k I_T \varphi_p \tag{5.11}$$

where $\xi = 2$ when two torque phase windings are active and $\xi = 1+(\theta_p+\beta-30)/2\beta$ when three torque phase windings are active. The calculation of torque is for the skewed rotor RDCMs so the rotor pole angle, θ_p is replaced by the angle $(\theta_p+\beta)$. In accounting for the torque ripple, the average torque of the different RDCMs is then calculated by averaging the torque for the case when two torque phase windings and the one when three torque phase windings are active.

For example: The calculation of the average torque with the analytical calculation method for the 6-phase RDCM with rotor 1 is as follows:

The machine specifications of the 6-phase RDCM are given in Table 5.5.

Table 5.5: 6-phase RDCM specifications.

Number of slots/pole/phase (q)	2
Number of parallel paths (n_a)	2
Number of conductors per slot (z)	48
Number of pole pairs (p)	2
Slot-pitch angle (β)	7.5^0
Airgap length (l_g)	0.00062 m

When two torque phase windings are active, the average flux density with skew taken into account, B_g as determined from FE is 0.8 T. So the flux per rotor pole arc is

$$\begin{aligned}\varphi_p &= B_g r_g l \theta_{ps} \\ &= 0.80 * 0.09775 * 0.175 * 39.9 * \pi/180 \\ &= 0.009528 \ \mathbf{Wb}\end{aligned}$$

while the machine constant is as follows:

$$k = \frac{2\,z\,q\,p}{\theta_{ps} n_a}$$
$$= \frac{2*48*2*2}{(39.9*\pi/180)*2}$$
$$= 275.7$$

Therefore torque from equation (5.11) when two torque phase windings are active can be calculated as follows

$$T = \xi\, k\, \varphi_p\, I_T$$
$$= 2*275.7*0.009528*45$$
$$= 236.4\ \textbf{Nm}$$

The same method as above is then repeated for the case when three torque phase windings are active and the average flux density as from FE for this case is 0.92 T. Hence the flux per rotor pole arc is

$$\varphi_p = B_g r_g\, l\, \theta_{ps}$$
$$= 0.92*0.09775*0.175*39.9*\pi/180$$
$$= 0.01096\ \textbf{Wb}$$

Then torque for the case when three torque phase windings are active is

$$T = \xi\, k\, \varphi_p\, I_T$$
$$= (1+(32.4+7.5-30)/2*7.5)*275.7*0.01096*45$$
$$= 1.66*275.7*0.01096*45$$
$$= 225.7\ \textbf{Nm}$$

The average torque is taken as the average of the torque for the case when two torque phase windings are active and the one when three torque phase windings are active and is as follows (236.4 + 225.7)/2 = **231.1 Nm**.

The above procedure is then applied for the optimum 6-phase RDCMs with rotor 2 and with rotor 3, and a summary of the average torque with both the analytical calculation method and the FE Maxwell stress tensor method is given in Table 5.6. It is noticeable from the table that the average torque calculated by the proposed analytical torque equation gives very similar results as the FE calculated torque.

Table 5.6: Average torque for the skewed optimum 6-phase RDCMs with different rotor structures by both the analytical and the FE Maxwell stress tensor method.

	Rotor 1	Rotor 2	Rotor 3
Analytical Torque [Nm]	231.1	233.0	233.5
FE – torque (Nm)	227	240.1	240.5

5.2.6 Armature reaction effect

The torque of the RDCMs results from the interaction between the *d-axis* flux (i.e. field flux) and the torque current. This then implies that the armature reaction effect can be analysed by investigating the effect of the torque current on the *d-axis* flux per rotor pole arc. The flux per rotor pole arc is investigated by the analysis of the average airgap flux density with the machine excited with field current only and also with the machine excited with both field and torque currents. The armature reaction effect is analysed when two torque phase windings are active which represents the case when the rotor pole arc covers the active torque phase windings.

The armature reaction effect, as in brush dc machines, is investigated by studying the variation of the airgap flux density at different positions of the salient pole rotor. Figure 5.16 shows a layout of the skewed rotor pole represented by 5 unskewed and displaced rotor poles; the skew angle is β. Also shown is the expected average airgap flux density across the axial length of the rotor pole. To study the armature reaction effect the rotor pole is divided into three pole sections as shown in Figure 5.16. For each *i-th* pole section the flux per pole section is determined as

$$\varphi_i = B_{gi}\, r_g\, l\, \varsigma\,, \tag{5.12}$$

where B_{gi} is the average flux density of the *i-th* pole section obtained by averaging the flux density across the pole section angle $\varsigma = (\theta_p + \beta)/3$.

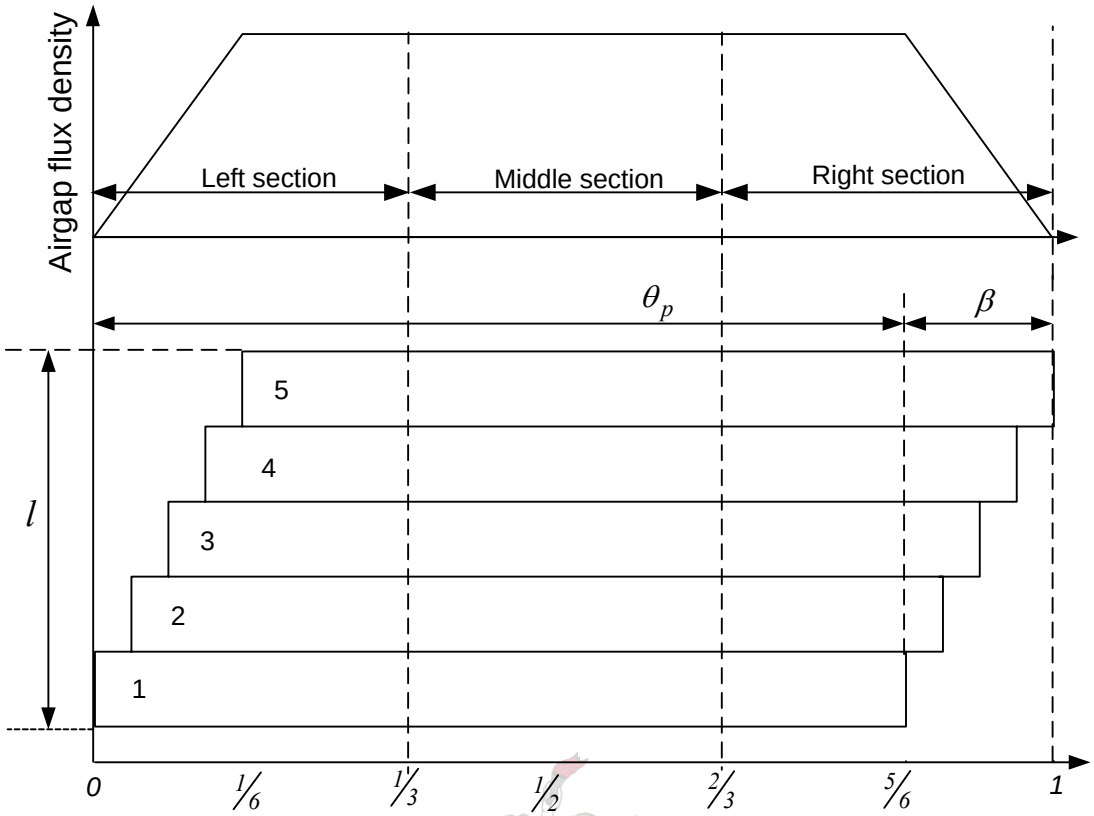

Figure 5.16: Ideal average airgap flux density across a rotor pole with skew taken into account showing the different pole sections.

The armature reaction effect of the 6-phase RDCMs with the different rotor structures is described in the sections that follow.

- *Rotor 1*

The airgap flux density waveform for the optimum 6-phase RDCM with rotor 1 and the machine excited with rated field current only and also with the machine excited with both rated field and torque currents are as shown in Figure 5.17(a). It is noticeable from the figure that the addition of the torque current tends to strengthen the airgap flux density on one side and weaken it at the other end of the rotor pole arc. This can be best shown by the flux per pole section as a function of the pole arc position.

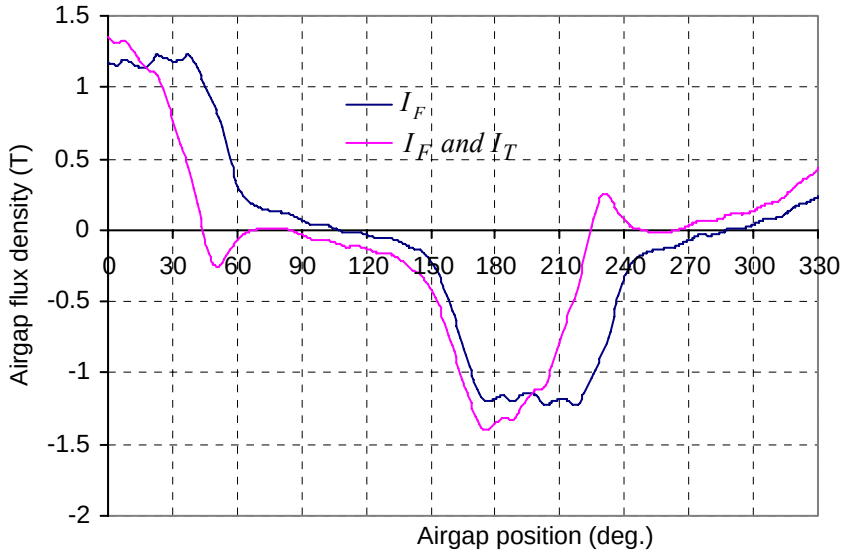

Figure 5.17(a): Airgap flux density versus airgap position with rated field current only and with both rated field and rated torque current for the 6-phase RDCM with rotor 1.

The flux per pole section as a function of the pole arc position for the machine with rotor 1 is as shown in Figure 5.17(b). The following observations can be made about the effect of the addition of the torque current on the flux per pole section.

- 19.8% increase in the flux per pole section in the left section.
- 3% decrease in the flux per pole section in the middle section
- 91% decrease in the flux per pole section in the right section.

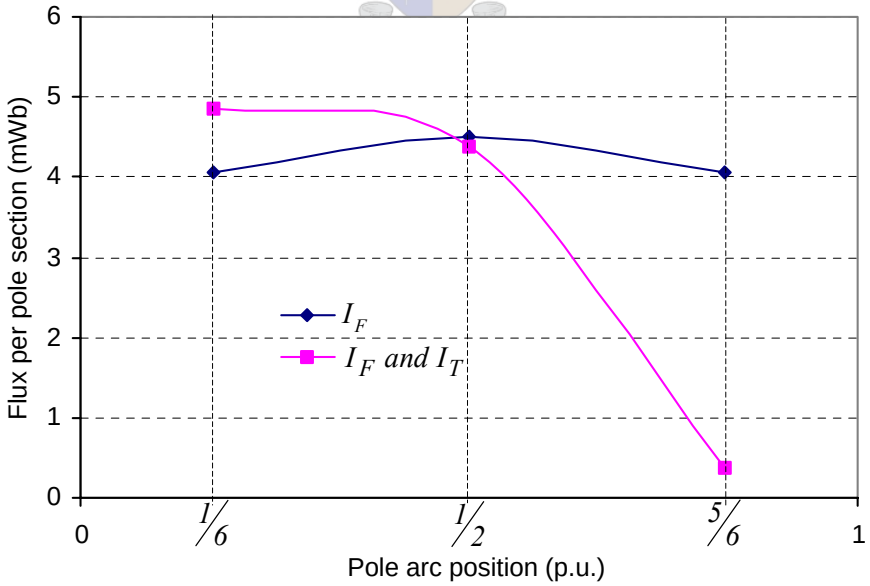

Figure 5.17(b): Flux per pole arc versus pole arc position with rated field current only and with both rated field and rated torque currents for the 6 – phase RDCM with rotor 1.

- *Rotor 2*

The same method as for the above 6-phase RDCM with rotor 1 is applied to the 6-phase RDCM with rotor 2 and the field and torque currents effect on the average flux density as a function of the airgap position is as given in Figure 5.18(a). The corresponding flux per pole section as a function of the pole arc position is shown in Figure 5.18(b).

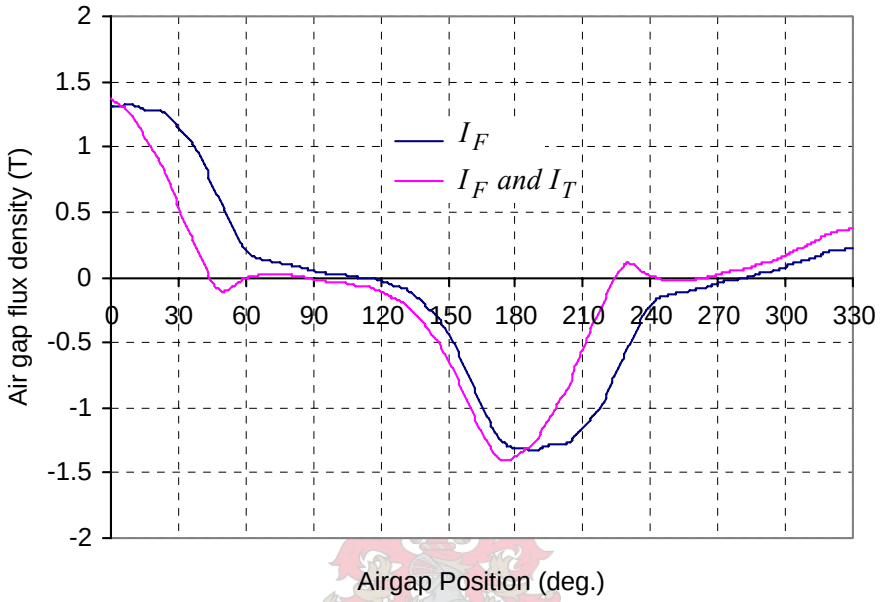

Figure 5.18(a): Average air gap flux density versus position with rated field current only and with both rated field and rated torque currents for the 6-phase RDCM with rotor 2.

It is noticeable from Figure 5.18(b) that the addition of torque current has different effects on the flux per pole section depending on the pole arc position and can be summarised as follows:

- 15% increase in the flux per pole section in the left section.
- 4.9% decrease in the flux per pole section in the middle section.
- 79% decrease in the flux per pole section in the right section.

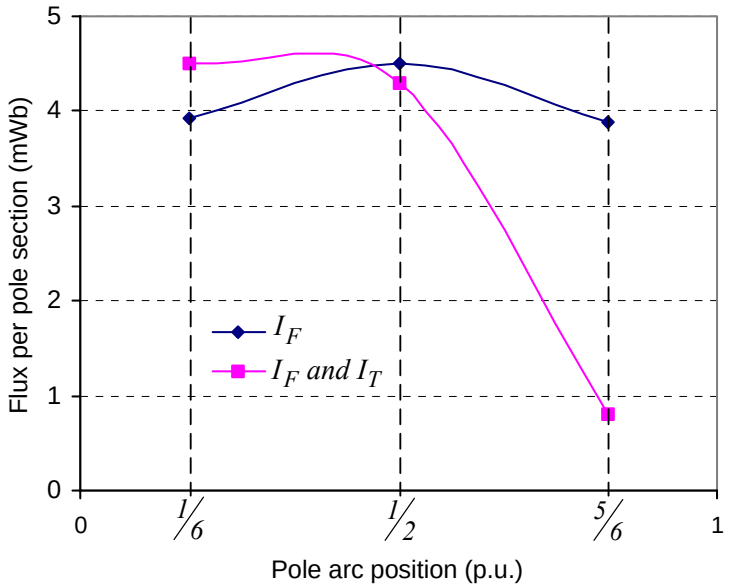

Figure 5.18(b): Flux per pole arc versus pole arc position with rated field current only and with both rated field and rated torque currents for the 6-phase RDCM with rotor 2.

- *Rotor 3*

Just as was done for the above-mentioned 6-phase RDCMs with rotor 1 and rotor 2, the average flux density with field current and with both field and torque currents, for the machine with rotor 3, is shown in Figure 5.19(a). With the average airgap flux density as a function of airgap position, the flux per pole section of the machine as a function of the pole arc position was derived and is as shown in Figure 5.19(b).

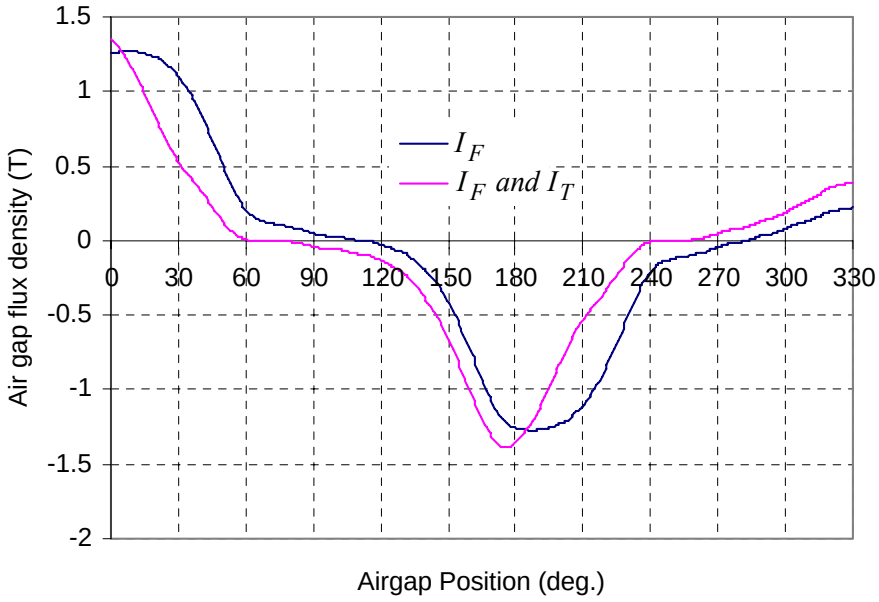

Figure 5.19(a): Average air gap flux density versus position with rated field current only and with both rated field and rated torque currents for the 6-phase RDCM with rotor 3.

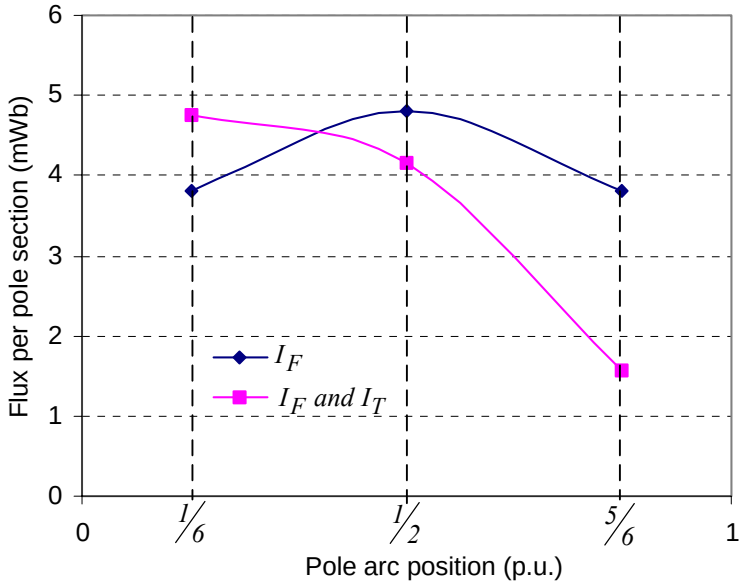

Figure 5.19(b): Flux per pole section arc versus pole arc position with rated field current and with rated field and torque currents for the 6-phase RDCM with rotor 3.

As was done for the previous machines, the effect of the addition of torque current on the flux per pole section for the machine with rotor 3 can be summarised as follows:

- 24.5% increase in the flux per pole section in the left section.
- 13% decrease in the flux per pole section in the middle section
- 59% decrease in the flux per pole section in the right section

5.2.7 Summary of the armature reaction effect

A summary of the armature reaction effects of the 6-phase RDCMs with the three different rotor structures is as shown in Figure 5.20. From Figure 5.20, it can be concluded that the machine with rotor 1 has a comparatively more severe armature reaction effect than to the machines with rotor 2 and rotor 3. This then implies that the chamfering of the rotor pole (rotor 3) and the addition of the slits (rotor 2) to the rotor pole can be considered to be a method of reducing the armature reaction effect of the RDCMs.

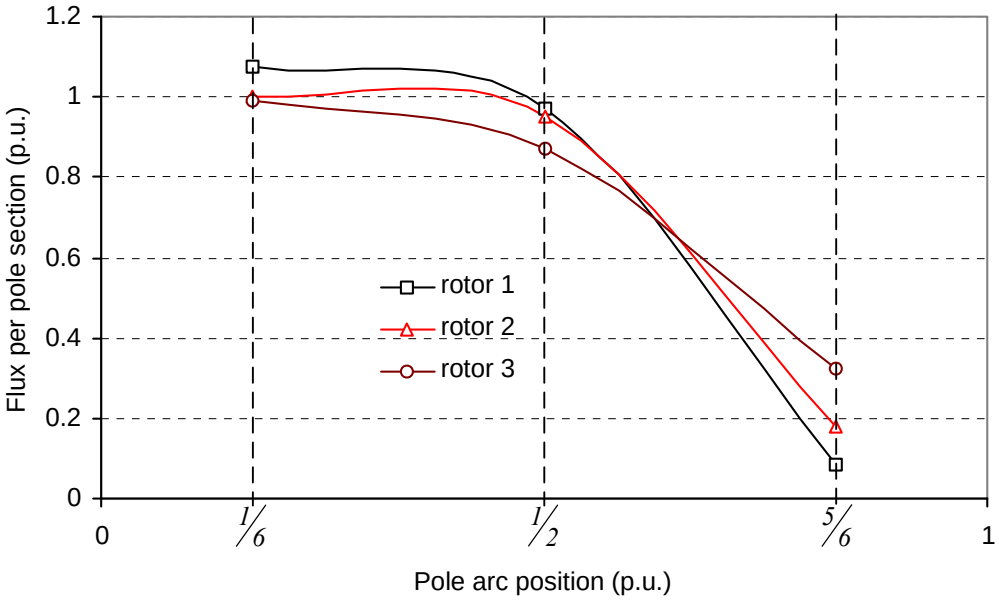

Figure 5.20: Flux per pole section of the 6-phase RDCM with different rotor structures with rated field and rated torque currents.

The armature reaction effects of the above-mentioned RDCMs can also be shown by the field plots of Figure 5.21. Just like for the previous analysis, the field plots are shown at a rotor position that corresponds to the case when two torque phase windings are active.

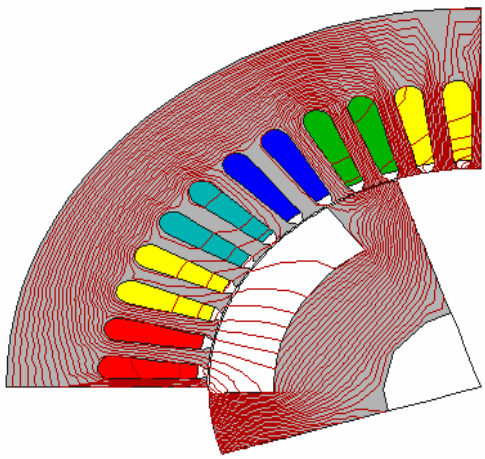

Figure 5.21(a): Field plot of 6-phase RDCM with rotor 1 with rated field and rated torque currents when two torque phase windings are active.

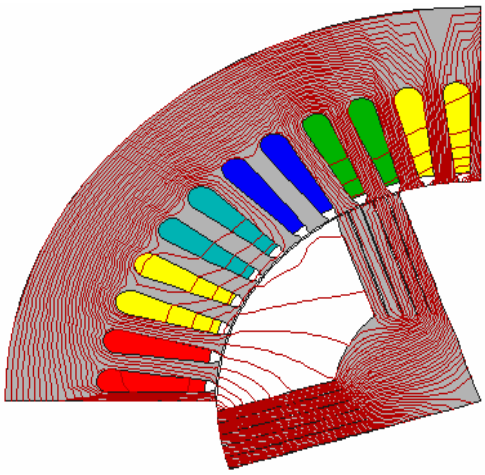

Figure 5.21(b): Field plot of 6-phase RDCM with rotor 2 with rated field and rated torque currents when two torque phase windings are active.

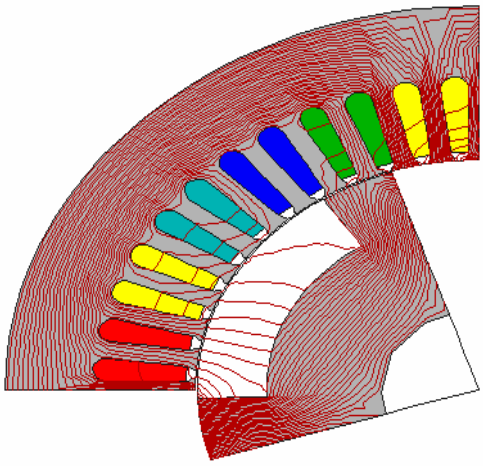

Figure 5.21(c): Field plot of 6-phase RDCM with rotor 3 with rated field and rated torque currents when two torque phase windings are active.

It is noticeable from Figures 5.21 that the field plots confirm the results of Figure 5.20 in the sense that they show that the 6-phase RDCM with rotor 1 has a severe armature reaction effect when compared to 6-phase RDCMs with rotor 2 and rotor 3.

5.3 Summary

The trapezoidal phase current waveform was further verified as the best current waveform when compared to the square current waveform in the sense that it yielded a lower torque ripple and higher torque per copper loss. It was shown that the optimum designed 5-phase RDCM with the trapezoidal current waveform developed a slightly higher torque than that of the optimum designed 5-phase RDCM with the square current waveform. But most importantly the torque ripple of the optimum designed skewed 5-phase RDCM with the

trapezoidal current waveform was found to be 16% lower than that of the optimum designed 5-phase RDCM with the square current waveform. In addition to the ripple torque of 5-phase RDCMs it was also found that the maximum torque with the same copper losses and stack volume for the machine with the trapezoidal current waveform is close (4% lower) to that of the optimum designed 5-phase RSM with the injection of third harmonic currents. The 6-phase RDCM drive is better to use than its 5-phase counterpart due to the fact that for maximum torque per copper loss, the optimum designed 6-phase machine resulted in an I_F/I_T ratio close to unity. This implies that the required current capability of the full-bridge inverter during field mode is thus close to the required current capability during torque mode.

It was further found that the torque per copper loss per stack volume of the optimum designed 6-phase RDCM is similar (1.3 % higher) to that of the optimum designed 5-phase RSM with third harmonic current injection. The optimum I_F/I_T ratio for maximum torque for the 6-phase RDCM with the following rotor structures; normal salient pole rotor, salient pole rotor with slitted poles and the salient pole rotor with chamfered pole tips is found to be between 0.85 – 0.88. It was also shown that the torque calculated based on Lorentz force law is in agreement with the FE Maxwell stress tensor method. Finally it was found that the optimum 6 - phase RDCM with a normal salient pole rotor has a severe armature reaction effect. It was shown that this armature reaction effect can be reduced by using slitted or chamfered salient pole rotors. This then improves the torque per copper loss output of the machine by 6%.

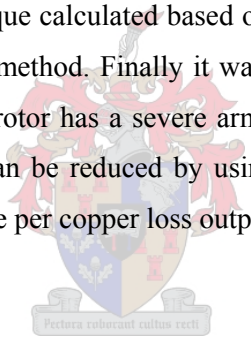

CHAPTER 6 Per phase equivalent circuit model of 6-phase RDCM

This chapter describes the per phase modelling of the 6-phase RDCM with the CR-rotor by the use of finite element analysis. The modelling of the RDCM in this particular case involves representing the RDCM as a per phase electrical equivalent circuit diagram. For completeness, the per phase equivalent circuit parameters of the RDCM are also determined in this chapter. The per phase equivalent circuit parameters of interest are resistance, self-inductance and the mutual inductances with other phases. In addition to the above, the back-EMF and the supply voltage on both no-load and on load conditions are determined in this chapter. The determined supply voltages can be used later in chapter 7 for comparison with the measured ones. In addition to the determination of the per phase equivalent circuit parameters, the model is also verified by calculating the torque based on the calculated instantaneous back EMF and phase currents.

6.1 Equivalent circuit

The RDCM considered in this study has a double three-phase stator (6-phase) and a salient pole rotor. The general stator voltage equation in the *abcdef* reference frame is

$$\mathbf{V}_s = r_s \mathbf{I}_s + \frac{d\boldsymbol{\lambda}_s}{dt}, \tag{6.1}$$

where $\mathbf{V}_s = \begin{bmatrix} v_a \\ v_b \\ v_c \\ v_d \\ v_e \\ v_f \end{bmatrix}$, $\mathbf{I}_s = \begin{bmatrix} i_a \\ i_b \\ i_c \\ i_d \\ i_e \\ i_f \end{bmatrix}$ and $\boldsymbol{\lambda}_s = \begin{bmatrix} \lambda_a \\ \lambda_b \\ \lambda_c \\ \lambda_d \\ \lambda_e \\ \lambda_f \end{bmatrix}$.

Flux linkage is a function of the six-phase currents and the rotor angle, therefore

$$\lambda_s = \mathrm{F}(i_a, i_b, i_c, i_d, i_e, i_f, \theta_r) \tag{6.2}$$

this then implies that

$$\frac{d\lambda_s}{dt} = \frac{\partial \lambda_s}{\partial i_a}\frac{di_a}{dt} + \frac{\partial \lambda_s}{\partial i_b}\frac{di_b}{dt} + \frac{\partial \lambda_s}{\partial i_c}\frac{di_c}{dt} + \frac{\partial \lambda_s}{\partial i_d}\frac{di_d}{dt} + \frac{\partial \lambda_s}{\partial i_e}\frac{di_e}{dt} + \frac{\partial \lambda_s}{\partial i_f}\frac{di_f}{dt} + \frac{\partial \lambda_s}{\partial \theta_r}\frac{d\theta_r}{dt} \tag{6.3}$$

When the *a*-phase is considered, equation (6.3) can be expressed as follows:

$$\frac{d\lambda_a}{dt} = L_a\frac{di_a}{dt} + L_{ab}\frac{di_b}{dt} + L_{ac}\frac{di_c}{dt} + L_{ad}\frac{di_d}{dt} + L_{ae}\frac{di_e}{dt} + L_{af}\frac{di_f}{dt} + \frac{\partial \lambda_a}{\partial \theta_r}\omega_r \tag{6.4}$$

With equations (6.4) and (6.1), the per phase voltage equation of the 6-phase RDCM can be written as

$$v_a = r_s \cdot i_a + L_a \frac{di_a}{dt} + L_{ab} \frac{di_b}{dt} + L_{ac} \frac{di_c}{dt} + L_{ad} \frac{di_d}{dt} + L_{ae} \frac{di_e}{dt} + L_{af} \frac{di_f}{dt} + e_a \ , \tag{6.5}$$

where e_a is the per-phase back EMF which is given by

$$e_a = \frac{\partial \lambda_a}{\partial \theta_r} \omega_r \, . \tag{6.6}$$

Based on equation (6.5), the per-phase equivalent circuit of a 6-phase RDCM can be shown as in Figure 6.1.

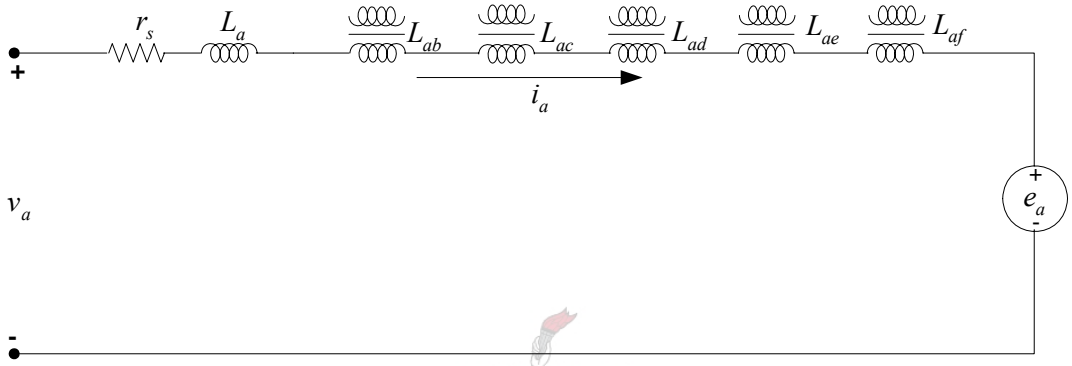

Figure 6.1: Per-phase equivalent circuit of a 6- phase RDCM.

The equivalent circuit diagram of Figure 6.1 is common to all AC machines with unexcited rotor structures. The unique part of this chapter is the determination of the equivalent circuit parameters of the 6-phase RDCM with the trapezoidal current waveforms by the use of finite element analysis. It is worth mentioning that the determination of the equivalent circuit parameters is based on the optimum 6-phase RDCM with the salient pole rotor without slits. The machine is built and tested as described in chapter 7. With the FE calculated parameters like supply voltage, a comparison can then be made between the calculated and the practically measured parameter.

6.2 Determination of the equivalent circuit parameters

The equivalent circuit parameters, which are to be determined are the phase resistance, the self- inductance, mutual inductance, supply voltage and the back EMF. The phase resistance as determined by equation (2.7) is 0.337 Ω.

All other parameters apart from the phase resistance are linked to flux linkage therefore to determine them the flux linkage must first be determined. The determination of flux linkage by FE is carried out in the same way as for the sinusoidal machines as described in the

previous chapters. As we know that the parameters of interest are functions of flux linkage, it is worth investigating the effect of the special current waveform on the flux linkage waveform. The flux linkage waveform with only field current is shown in Figure 6.2. It can be noted that the flux linkage tends to follow the current waveform.

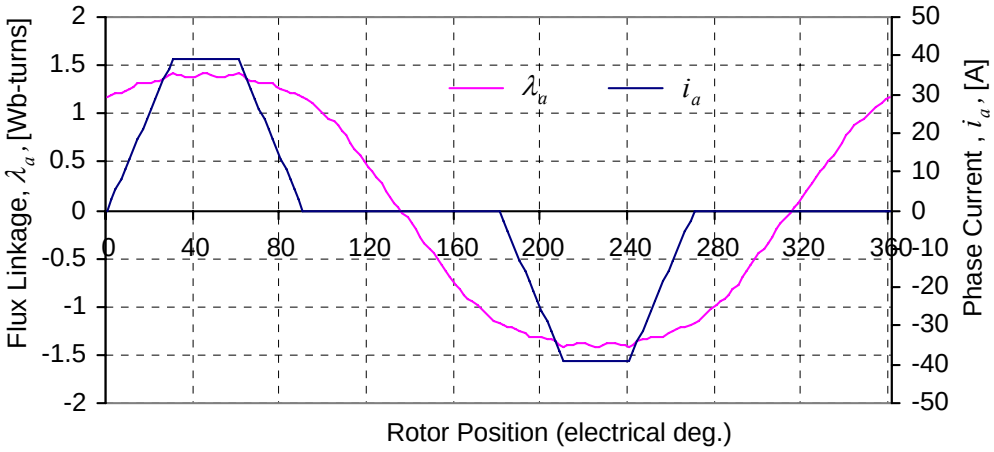

Figure 6.2: Phase flux linkage and phase current versus position with rated field current only.

The addition of the torque current (that is, field and torque current) has an effect on the flux linkage waveform as shown in Figure 6.3. As it can be observed from the figure, the addition of the torque current results in some ripples on the flux linkage waveform that are not affected by skewing of the rotor. The ripples as seen from the figure tend to correspond to the point of change in the current waveforms.

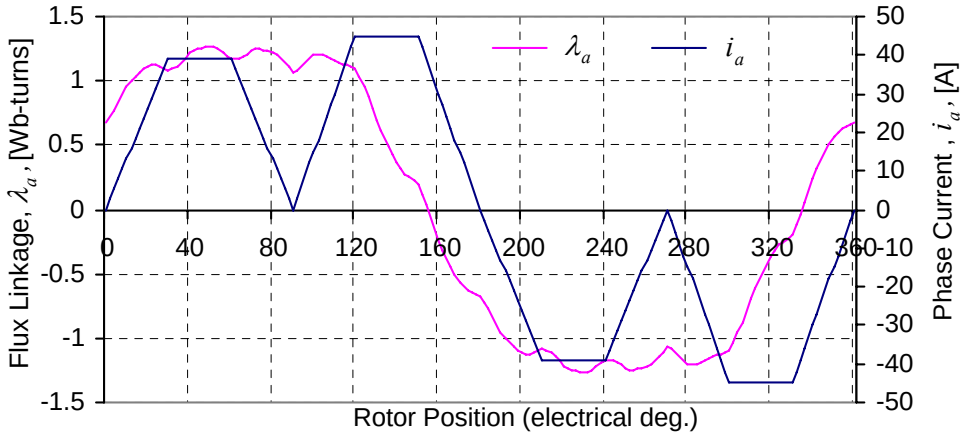

Figure 6.3: Phase flux linkage and phase current versus position with rated field and rated torque currents.

One more thing that can be observed from the flux linkage waveforms of Figures 6.2 and 6.3 is that there is a phase shift between the two flux linkage waveforms. The phase shift as

shown in Figure 6.4, between the flux linkage with rated field and rated torque current and the flux linkage with rated field current only, is due to the vector addition of field flux linkage and torque flux linkages. It is also noticeable from the waveforms that the magnitude of the flux linkage with field current only is higher than that with both field and torque currents. This is due to the strong cross-coupling effect of the machine, as discussed in the previous chapter.

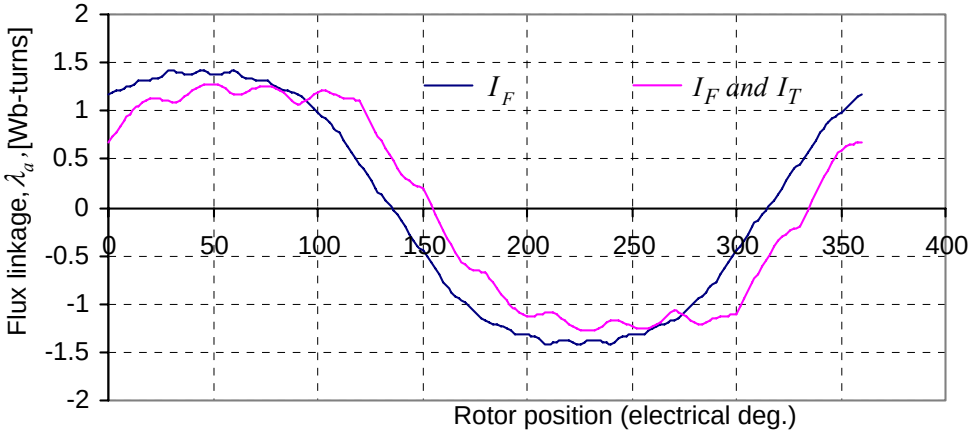

Figure 6.4: Phase *a* flux linkage as a function of position with rated field current only and with rated field current and rated torque current.

6.2.1 Inductance

As shown in the per phase equivalent circuit diagram, there are two kinds of inductances namely self-inductance and mutual inductance. The mutual inductances are due to the coupling between phases. This thesis is based on skewed machines, it therefore follows that the FE calculated flux linkages are with skew taken into account. With the flux linkages, the inductances can be determined as in equations (6.3) and (6.4) as follows:

$$L = \frac{\partial \lambda}{\partial i} \tag{6.7}$$

The calculation of the inductance from FE can be done with the knowledge that the flux linkage is a function of the 6-phase currents and position. It then implies that the different inductances (self and mutual) can be determined by adding a small change to one phase current while keeping others constant, and deriving the corresponding flux linkages. The corresponding flux linkages the author is referring to are the flux linkages due to the current after adding a small change in current and after subtracting a small change as shown in Table 6.1. What should be noted is that the analysis of the machine under study is based on current controlled machines, that is, a known current is inputted together with the machine dimensions and the FE calculates the flux linkages. It is also worth mentioning that the flux

linkages are determined at rated field and torque currents. This can best be shown in a table form as in Table 6.1, showing the FE current inputs with their corresponding FE flux linkage outputs. Note that in this table, a small change, Δi, is added and subtracted to phase *a* current. The small change of 0.1 A was used for this analysis.

Table 6.1: Flux linkages as a function of current with small current disturbance.

INPUT	**OUTPUT**					
$i_a + \Delta i_a$	λ_a	λ_b	λ_c	λ_d	λ_e	λ_f
$i_a - \Delta i_a$	λ_a'	λ_b'	λ_c'	λ_d'	λ_e'	λ_f'

Based on equation (6.7) and the results in Table 6.1, the inductances can be calculated as follows (taking phase *a* as an example):

$$L_a = \frac{\lambda_a - \lambda_a'}{2\Delta i_a}, \tag{6.8}$$

while the mutual inductance is calculated by

$$L_{ak} = \frac{\lambda_k - \lambda_k'}{2\Delta i_a}, \tag{6.9}$$

where *k* represents the coupling phases and the coupling phases for phase *a* are *b,c,d,e* and *f*.

Based on the above analysis, the self-inductance versus position of the machine under no-load and loaded conditions are shown in Figures 6.5(a) and 6.5(b) respectively. No load conditions refers to the case when the machine is excited with field current only, while the loaded condition is when the machine is excited with both field and torque currents.

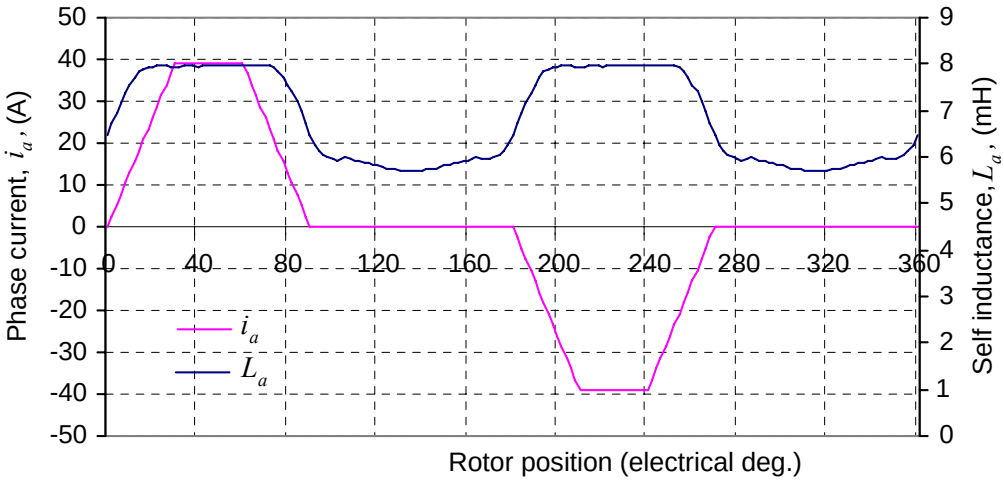

Figure 6.5(a): Self-inductance and phase current for phase *a* as a function of rotor position at rated no-load.

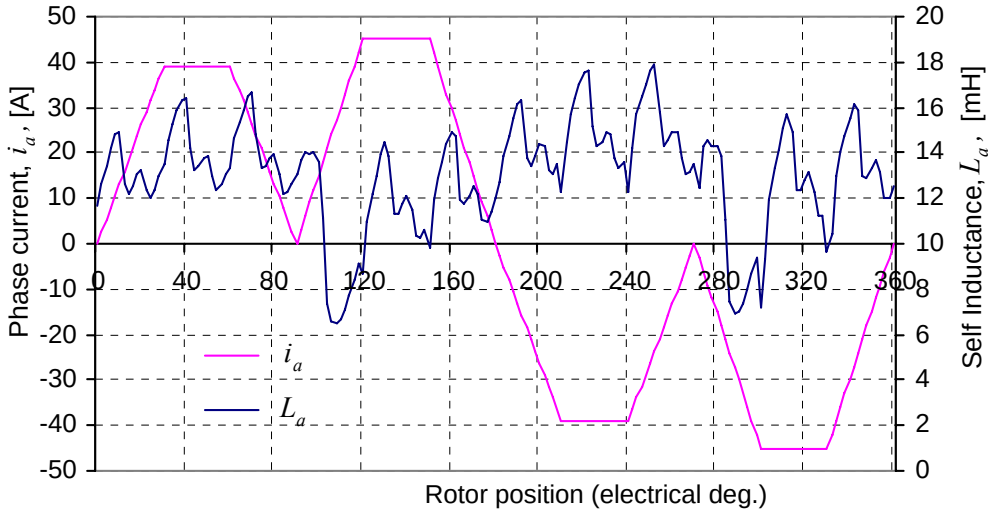

Figure 6.5(b): Self-inductance and phase current for phase *a* as a function of rotor position at rated loaded condition.

It is noticeable from Figure 6.5(a) that the self-inductance of phase *a* tends to follow its current waveform at no load conditions. But with load conditions, that is, with an addition of torque current the self-inductance waveform does not follow the current waveform exactly due to the strong cross-coupling effect of the machine. It is also noticeable from Figures 6.5(a) and (b) that the self-inductance waveform for the loaded condition contains some ripples as compared to that of no-load conditions. The analysis of the ripple content on loaded conditions is elaborated at a later stage in this chapter. The mutual inductance versus rotor position as determined by the method described above for both no-load and on-load conditions are as shown in Figures 6.6 (a) and (b) respectively.

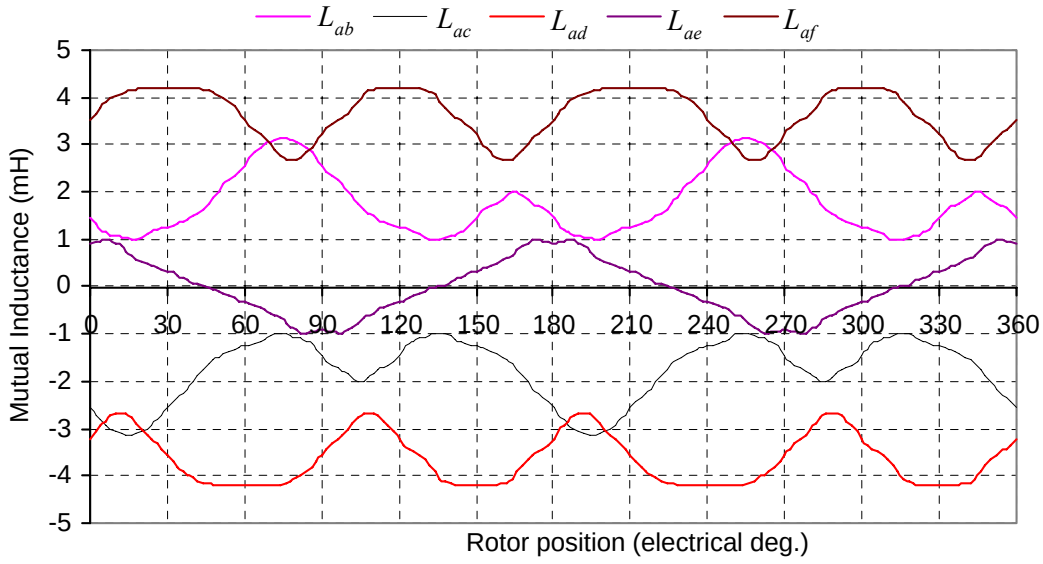

Figure 6.6(a): Mutual inductance between phases *a* and other coupling phases as a function of rotor position at rated no-load conditions.

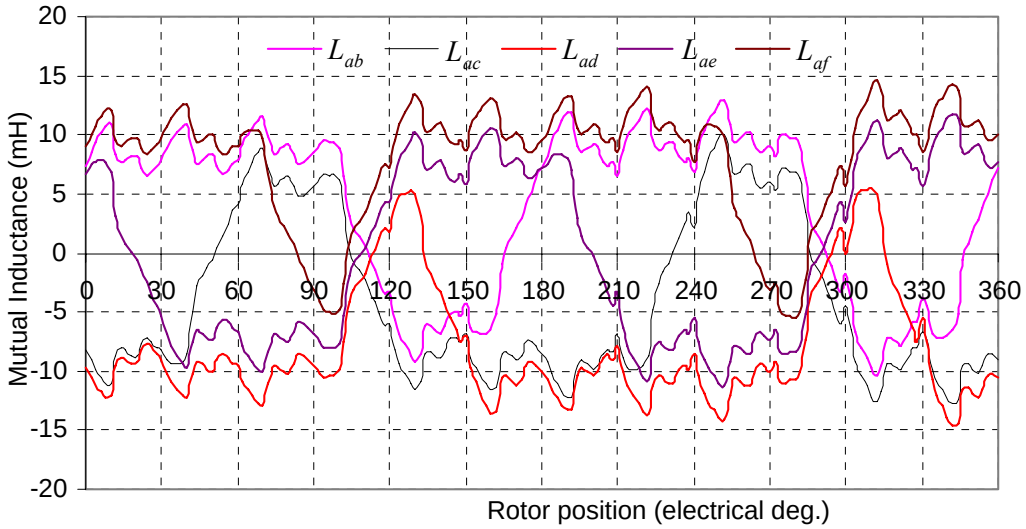

Figure 6.6 (b): Mutual inductance between phases *a* and other phases as a function of rotor position at rated loaded conditions.

It is noticeable from the above figures that just like for the self-inductance waveforms the mutual inductance waveforms at-load conditions contain high ripples. It is also noticeable from the figures that there is symmetry between the mutual inductances.

6.2.2 Back EMF

The procedure applied for the inductance calculation, can be applied to determine the back EMF. But for the determination of back EMF, all the six phase currents are kept constant and a small disturbance is added to the position and the corresponding flux linkage values are FE calculated which are then used to calculate the back EMF. With the knowledge that the 6-phase currents are functions of position, the change in position without a change in currents can be achieved in FE by adding a small change in position in the skew sub-routine. Like for the inductance calculation as described previously, the input and output parameters of interest for the back EMF calculations are as given in Table 6.2. The small change in position, $\Delta\theta_r$, was taken as $\pi/60$ radians.

Table 6.2: Flux linkages as a function of position with a small position disturbance.

INPUT	**OUTPUT**					
$\theta_r + \Delta\theta_r$	λ_a	λ_b	λ_c	λ_d	λ_e	λ_f
$\theta_r - \Delta\theta_r$	λ_a'	λ_b'	λ_c'	λ_d'	λ_e'	λ_f'

From the flux linkages derived from FE (Table 6.2) with a small disturbance in position, the back EMF can be calculated by

$$e_k = \frac{\left(\lambda_k - \lambda_k^{'}\right)}{2\Delta\theta_r}\omega_r\,, \tag{6.10}$$

where k is the different phases (*a, b, c, d, e, f*), so with the above equation, the back EMF of the different phases can be determined. The calculated back EMF for phase a, e_a, at rated speed of 1500 rpm at no-load and load conditions are as shown in Figures 6.7(a) and (b) respectively; note that the back phase EMF waveform is shown with its corresponding phase current waveform.

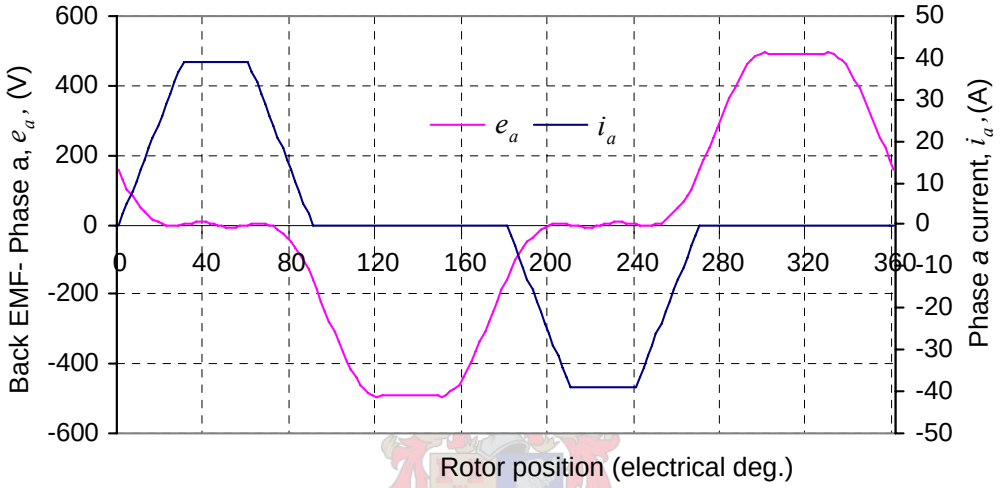

Figure 6.7(a): Back EMF and current of phase a versus rotor position at no-load (I_F = 39 A and I_T = 0)

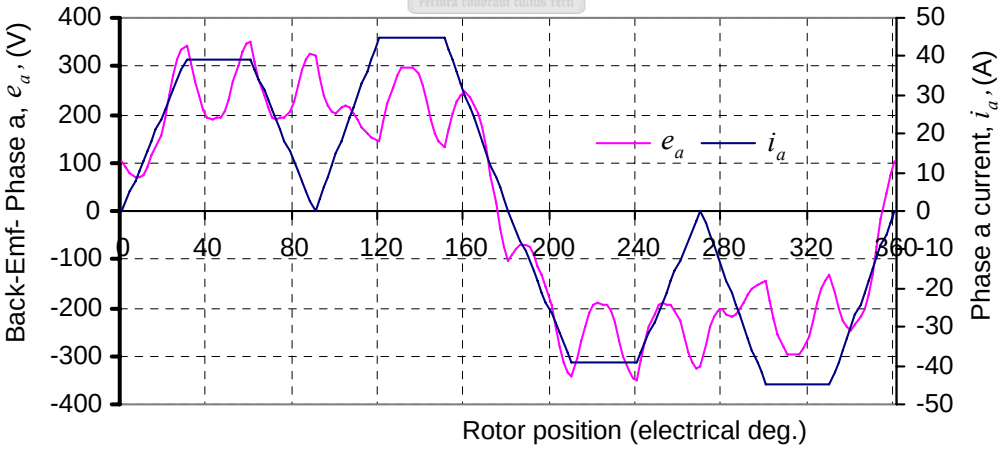

Figure 6.7(b): Back EMF and current of phase a versus rotor position at full – load (I_F = 39 A and I_T = 45 A)

It is noticeable from figure 6.7(a) that even though at no-load conditions, there is no current in the torque coils there is a voltage induced over the torque coils. The addition of torque current as shown in figure 6.7(b) results in a trapezoidal shaped back EMF just like for the BDCMs.

It is also observed that just like for the inductance waveforms at load conditions, the back EMF waveform at load conditions does have some ripples. The back EMF waveform at load conditions also shows a drop in the torque region, which is due to the strong cross-coupling effect of the machine.

6.2.3 Supply Voltage

There are two methods that are used in this section to determine the supply voltage. The first method is similar to that applied for determining the back EMF but for these method a small disturbance in position results in a change in current. The second method applies equation (6.5) to derive the supply voltage and for this thesis the method is referred to as the voltage addition method.

For the calculation of supply voltage by the use of the first method, the FE input and output parameters for the calculation are the same as those for the calculation of the back EMF. The supply voltage can be calculated by the use of the same equation (equation (6.10)) that was used to calculate the back EMF. Just like for the back EMF, the calculated phase *a* supply voltage as a function of position for the no-load and at-load conditions are as shown in Figures 6.8(a) and (b) respectively.

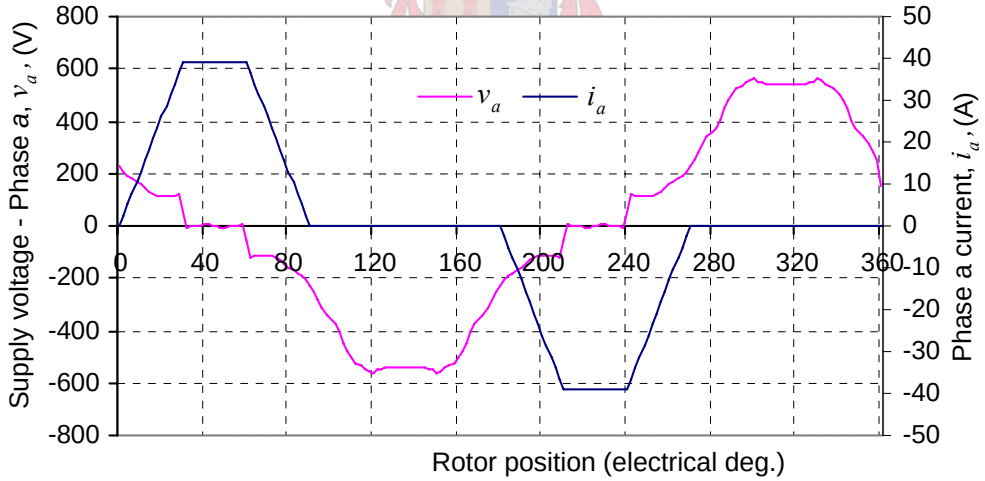

Figure 6.8 (a): Supply voltage with its corresponding current waveform at no- load (I_F = 39A and I_T = 0A)

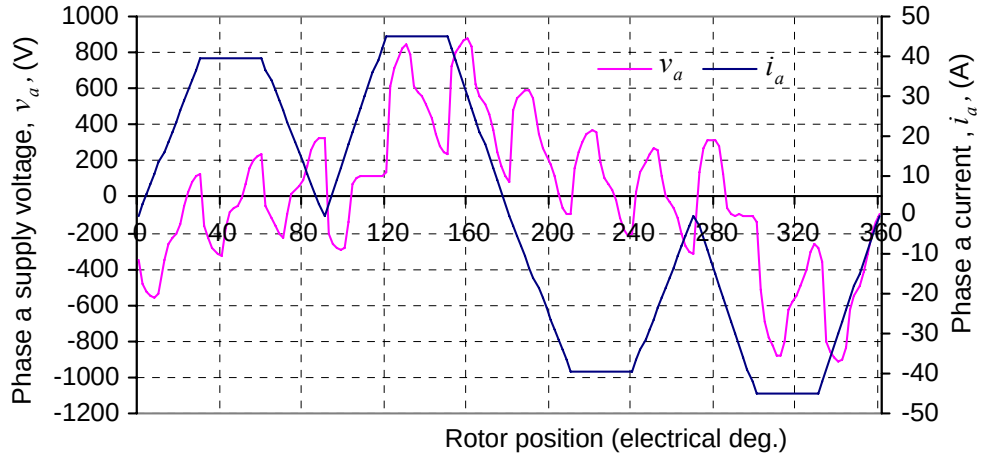

Figure 6.8 (b): Supply voltage with its corresponding current waveform at full – load (I_F = 39A and I_T = 45A)

It is noticeable from Figure 6.8(a) that the phase supply voltage at no-load conditions is similar to the phase back EMF at no load conditions (refer to Figure 6.7(a)), just like in separately excited DC motors, while for the phase supply voltage at load conditions as shown in figure 6.8(b), the average voltage in the field region is almost zero and builds up in the torque region. Just like for other previously discussed waveforms at load conditions, the phase supply voltage does comprise of the same ripples that will be explained in the next section.

For the voltage addition method, the already determined instantaneous inductances and back EMFs together with the derivatives of the phase current waveforms are substituted into equation (6.5) to determine the supply voltage. In determining the supply voltage the resistive voltage drop, $r_s i_a$, is neglected and it is calculated for full-load condition. The supply voltages as calculated by the two methods are as shown in Figure 6.9. It can be observed that there is a good agreement between the results of the two methods.

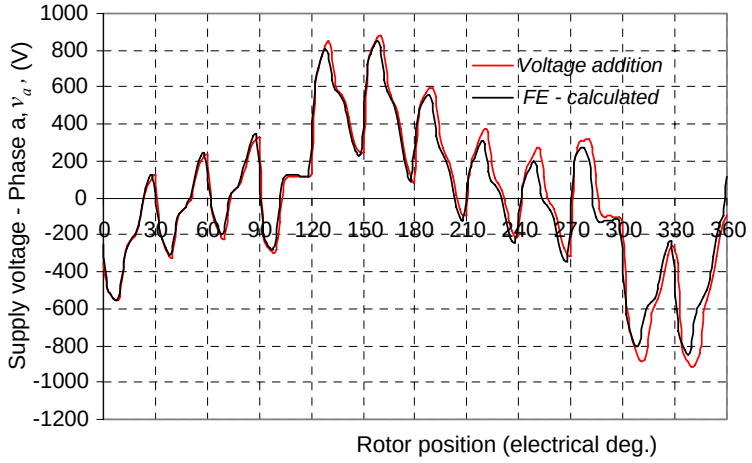

Figure 6.9: Calculated supply voltage with both the voltage addition and the FE method versus rotor position at full – load (I_F = 39 A and I_T = 45A).

6.3 Remarks on the determined parameters

As discussed in the previous sections, the determined per phase equivalent circuit parameters at load conditions do have some ripples. The ripple content on the equivalent parameters is reflected on the inductance waveforms, the back EMF waveforms and also on the supply voltage waveforms. The ripple on the waveforms is of the same frequency meaning that the ripple in all the parameters is generated from the same source. It is noticeable from the waveforms, taking for example the supply voltage waveform of Figure 6.8(b) that the oscillations in the supply voltage correspond to the current change. The ripple is surely not due to the slotting effect as only skewed machines are considered and skewing eliminates the slotting effect. Based on this, it can be concluded that the ripple content of the per phase equivalent circuit parameters is due to the current commutation every 30 electrical degrees.

6.4 Verification of the Model

The verification of the per phase equivalent circuit model proposed in this chapter was done by comparing the FE calculated torque and the torque calculated from the per phase equivalent parameters.

Based on the per phase equivalent circuit model developed in this chapter, the instantaneous electromagnetic torque equation of the 6-phase RDCM is [Ishak (2005)]

$$\begin{aligned} T &= \frac{P_{out}}{\omega_r} \\ &= \frac{1}{\omega_r} \sum_{j=1}^{6} e_j i_j \ , \end{aligned} \tag{6.11}$$

where e_j and i_j are the instantaneous back EMFs and currents in phases 1-6 respectively. For purposes of this thesis, this method is to be referred to as simply the equivalent circuit calculation method. With the torque equation (6.11), the torque performance of the 6-phase RDCM can be determined with the known 6-phase current waveforms and the FE calculated phase back EMFs. It should be noted that the torque is calculated at rated speed of 1500 rpm (157 rads/s) and rated loaded conditions. The calculated torque performance of the machine with both the equivalent circuit torque calculation method and the FE Maxwell stress tensor method is as shown in Figure 6.10.

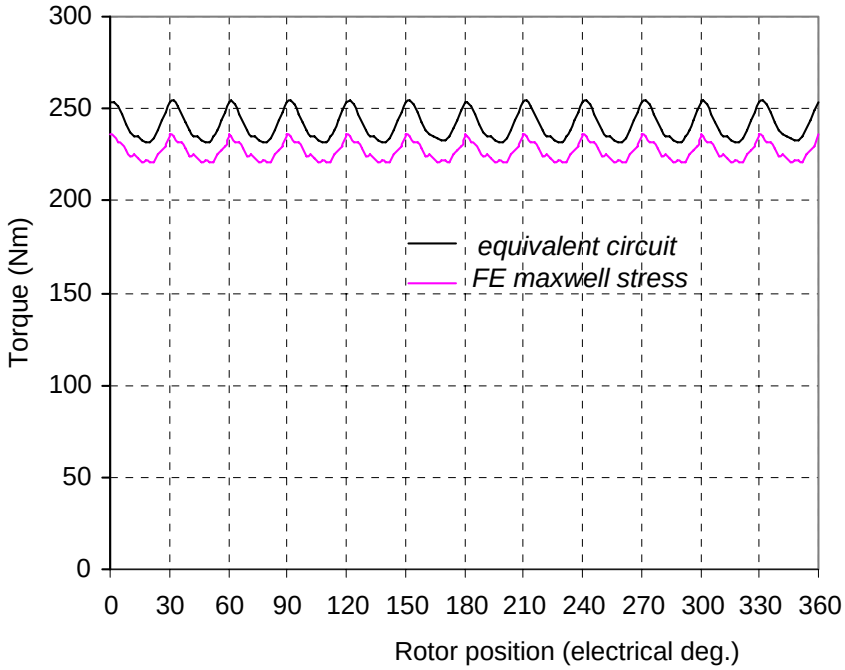

Figure 6.10: Torque performance of the 6-phase RDCM with both the equivalent circuit and the FE Maxwell stress tensor torque calculation method.

It is noticeable from Figure 6.10 that the calculated torque by the two methods is in good agreement verifying that the per phase equivalent circuit modelling proposed in this chapter is correct. The torque calculated by the equivalent circuit method is slightly higher than the one by FE Maxwell stress tensor method. This is due to the fact that equation (6.3) used for the calculation of the instantaneous back EMF is based on super position. Super position is not necessarily accurate for the non-linear systems as changing one parameter has an effect on others.

6.5 Summary

The per phase equivalent circuit parameters of the machine were determined by the use of FE analysis for both no load and load conditions. The determined parameters are the per-phase inductance and the voltages (both back EMF and supply voltage). With the determined parameters, it was shown that the parameters as a function of rotor position at load conditions do contain a ripple content due to the current commutation of the trapezoidal current waveform. The determined back EMF waveform for the RDCM resembles that of BDCMs because of its trapezoidal waveshape. It has also been shown that the torque calculated from the instantaneous FE calculated back EMF and current and the torque calculated by the FE Maxwell stress tensor are in good agreement. This verifies the per-phase equivalent circuit model of the machine.

CHAPTER 7 Measured and calculated results

In order to verify the accuracy of the FE analysis, measurements need to be performed on the designed machine. The measured torque performance in comparison with the FE-calculated torque performance of the optimum designed 6-phase RDCM with the salient pole rotor is focussed in this chapter. The components of the electric drive system of the 6-phase RDCM that includes the power converter, the electric machine and the digital controller are also briefly described. In addition to the components of the electric drive system, the current control method (hysteresis) used in this thesis is briefly described. The tests carried out to verify the optimum designed machine are also described and the tests are static and running tests. The static tests are carried out both with DC power source and with the electric drive system. The running tests are performed both in the constant torque region and in the constant power region. The measured results of the above tests are presented and compared to the FE-calculated ones.

7.1 Experimental set-up

The different components of the experimental set-up that make up an electric drive system are as shown in Figure 7.1. It can be shown from the figure that the 6-phase RDCM is connected to the supply via a rectifier and the inverter. The rectifier used in this set-up is a controlled rectifier and it rectifies 380 V AC to 550 V DC. The inverter built for this application is a 6-phase full-bridge inverter with 200 A IGBT modules. The digital controller via the semikron SKH121 drivers controls the switching of the IGBT modules. Photos of the built rectifier and the inverter are shown in appendix C.

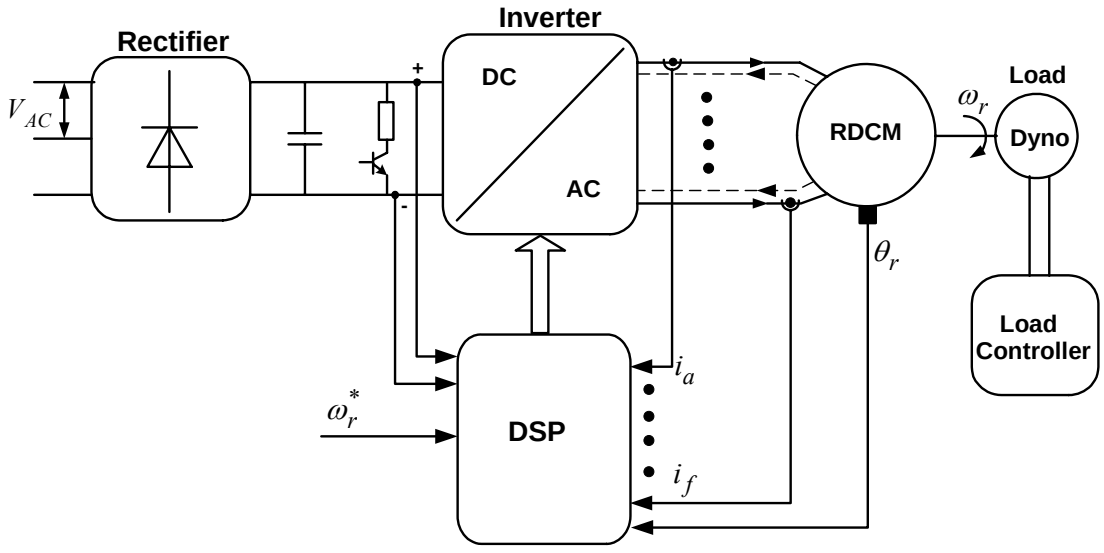

Figure 7.1: 6-phase RDCM drive system

The machine under test for this investigation is a 6-phase RDCM with a salient pole rotor. The optimum 4-pole, 35kW 6-phase RDCM has been built with the rotor skewed by one stator slot pitch and a 48-slot stator winding. Photos of the stator and the rotor of the machine are shown in the appendix D. For the loading of the machine, water-cooled Eddy-current dynamometers coupled to the shaft of the machine are used. As can be seen in Figure 7.1, the type of the digital controller used for the electric drive system is the TMS 320 VC 33 DSP. The DSP used is a 20 MHz floating- point processor. This type of DSP was manufactured specifically for use in the control of variable AC motor drives and power electronics. The DSP consists of four major blocks as shown in Figure 7.2. The four blocks are the processor, measurement interface, position interface and the fibre optic interface. The position and speed are measured digitally and then read by the processor. The rest of the control is implemented in software running in the DSP processor. The software used for this particular DSP is C-language. The photo of the DSP controller is shown in Figure E.1. The main task of the digital controller is to regulate the current into the machine based on the reference current waveforms. The current control method used for this particular investigation is the hysteresis current controller. The next section describes the hysteresis current control method and how it is implemented in this thesis by the use of the floating point DSP.

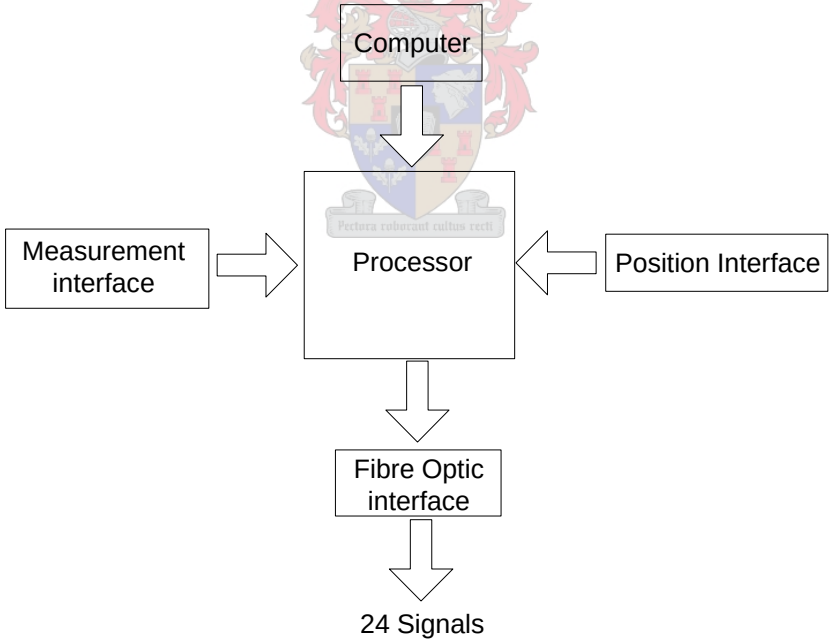

Figure 7.2: Block diagram of the DSP control unit

7.2 Hysteresis Current Controller

As reflected by Kazmierkowski (1998), the performance of the electric drive largely depends on the quality of the applied control strategy. In this thesis, the current control strategy that is

applied is the hysteresis current controller as it is the popular choice for current control with sufficient dynamic stability [Manjrekar (2000)]. A hysteresis current control scheme is based on a non-linear feedback with two level hysteresis comparators. The switching signals results when the error exceeds an assigned hysteresis band. As reflected by the above-mentioned authors, the main objective of the current controller is to force the currents in a six-phase AC load to follow the reference currents.

The block diagram of the hysteresis current controller is as shown in Figure 7.3. As shown in the block diagram, the controller generates the switching states (s_a - s_f) by comparing the reference current signals ($i_a^* - i_f^*$) and the measured currents ($i_a - i_f$). The controller is such that the switching of the converter devices regulates the currents so as to decrease the current errors ($\varepsilon_a - \varepsilon_f$). Hence based on the above, it can be concluded that the current controller implements both the error compensation and the determination of the switching states. Also as shown from the figure, the controller derives the converter switching signals from the comparison of the current error and the fixed hysteresis band. The unpleasant feature of the hysteresis current controller is that it produces a varying modulation frequency for the power converter [Kazmierkowski (1998), Buso (1998), Manjrekar (2000)]. Hence, it is important to make sure that the hysteresis band selected does not result in a very high switching frequency that might damage the power semi-conductor devices. The magnitude of the hysteresis band is a compromise between losses in either the motor or the controller. As the hysteresis band gets larger the switching frequency reduces and hence the IGBT switching losses get lower. For purposes of this thesis, a hysteresis current controller with a fixed band is implemented digitally. In summary, it means that for purposes of this thesis, with the measured and reference phase currents, the hysteresis current controller is implemented by software in the DSP.

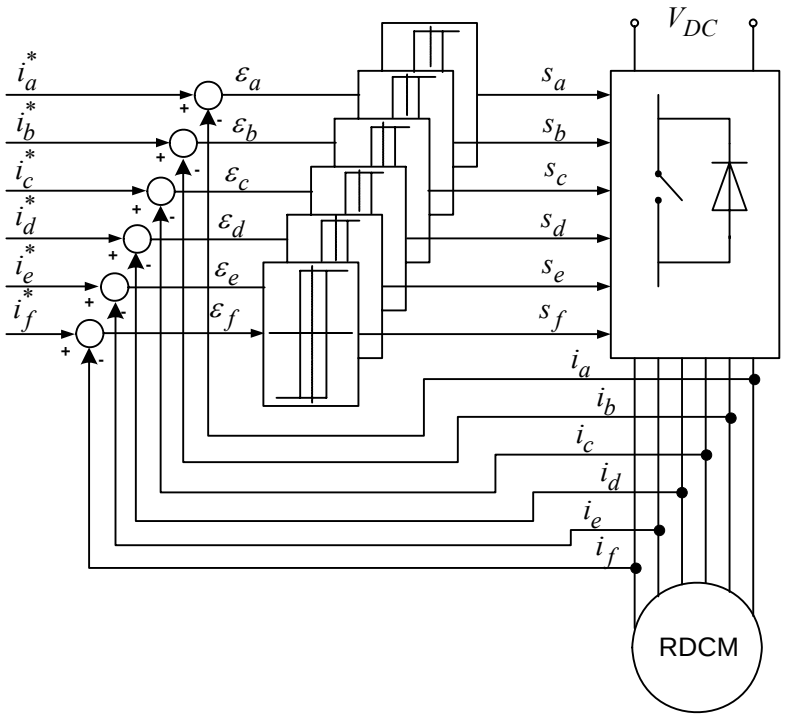

Figure 7.3: Block diagram of a hysteresis current controller for a 6-phase RDCM.

7.3 Determination of the zero position

The zero position of the machine is very important for the correct placement of the current waveforms as per rotor position, hence, it is important to determine the zero position of the machine. With the 6-phase trapezoidal current waveform (refer to Figure 5.11 from chapter 5), the zero position of the machine was determined by injecting DC current to phase windings *C* and *F* with the correct polarity and the rotor aligned itself as shown in Figure 7.4. But for simplicity, the machine is taken to be a 2-pole machine even though the machine under study is a 4-pole machine. Note that from the current waveforms, at zero position there are two active field windings (C and F) and two torque (B and D) windings active. The correct zero position means that when torque current, I_T, is zero and field current, I_F, is larger than zero, the rotor will not rotate provided the rotor is at zero position. The zero position of the machine is then marked.

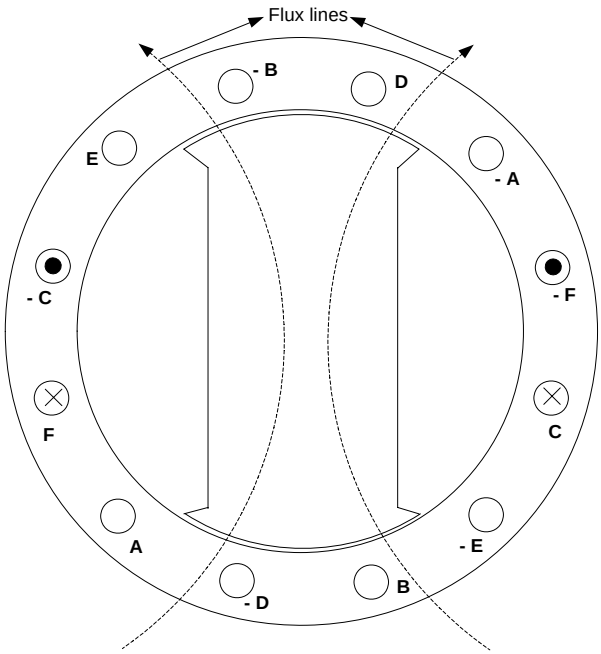

Figure 7.4: RDCM rotor alignment with the injection of DC currents in the phase windings C and F.

7.4 DC Static test

With the known zero position of the machine, the DC static test of the machine can then be performed. For the DC static test, the rotor is locked at a certain known rotor position and the corresponding field and torque currents of known magnitude are applied to the appropriate phase windings depending on the instantaneous 6-phase trapezoidal current waveforms. A clamp with an arm length of just over 20 cm was used to lock the rotor of the machine with the load cell coupled to the clamp for measuring force.

For instance at zero rotor position, the rotor is locked at zero position and DC currents of known magnitude is applied to phase windings C and F (i.e. field circuit) and B and D (i.e. torque circuit). The connection diagram is as shown in Figure 7.5(a), note that for simplicity the field and torque currents are taken to be equal and the field and torque windings are connected in series. The polarity of the phase winding currents is taken into consideration. The DC injected current, I_{DC}, was taken to be 40 A. The test was carried out from 0^0 – 60^0 (mechanical) in steps of 7.5^0 (mechanical). It should be noted that at 7.5^0 (mechanical) as shown from the current waveforms, all the six phase windings currents are active, three field ones and three torque ones. The test connection diagram for the case when all the six-phase winding currents are active is as shown in Figure 7.5(b). The torque measurement is done by the use of a load cell that is coupled to the arm of the blocked rotor test equipment. The photo of the blocked rotor test equipment is as shown in Figure E.2. The blocked rotor test

equipment is calibrated in degrees, allowing the rotor to be locked in certain known rotor positions.

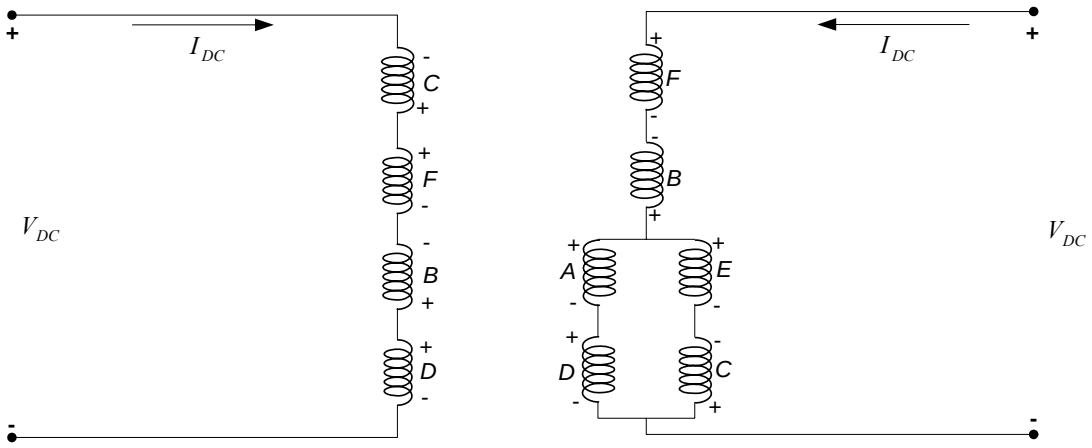

(a) (b)

Figure 7.5: Connection diagram for DC static test at (a) 0^0 and (b) 7.5^0 (mechanical).

With the 6-phase trapezoidal current waveforms it shows that the connection diagrams of Figures 7.5(a) and (b) was repeats every 15 mechanical degrees, but with different phase windings. The results of the DC static test in comparison with the FE-calculated results are as shown in Figure 7.5(c).

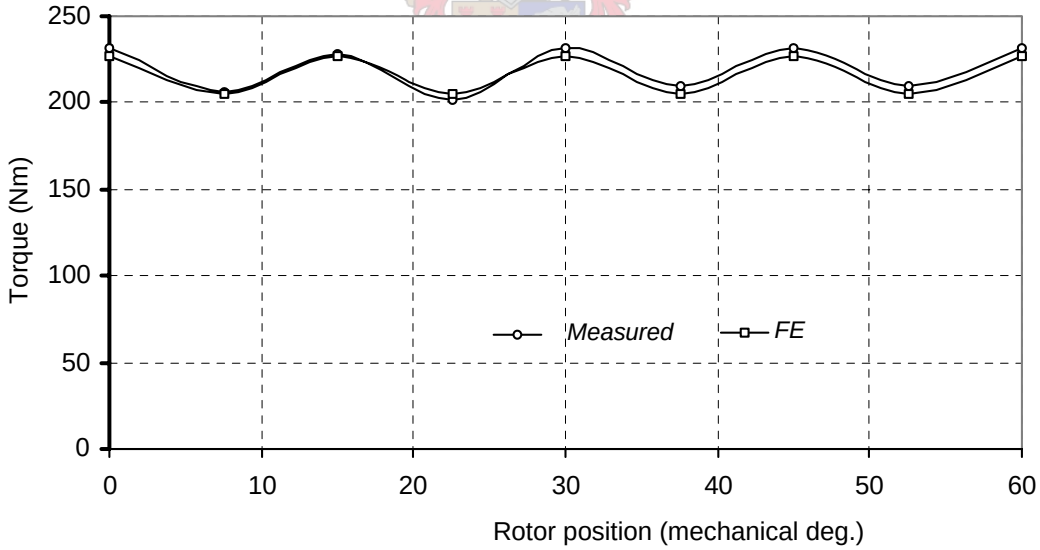

Figure 7.5 (c): FE – calculated and measured torque versus rotor position for the DC static test

It can be observed from the figure that there is a good agreement between the measured and FE calculated torque results. This then verifies that the built 6-phase RDCM is a complete replica of the FE analysed machine. Having verified the machine with the above DC static test, the next step is to perform the static test by making use of the electric drive system. For

the electric drive system to accomplish this task, the control is such that the instantaneous trapezoidal phase current waveforms are generated as a function of rotor position. As mentioned from chapter 6, the ripple torque is clearly caused by the phase current commutation every 30° electrical.

7.5 Inverter Static test

The aim of the inverter static test is to test the DSP and the inverter, as the machine was verified by the DC static test. With the inverter static test, the electric drive system through the DSP is controlled in such a way that the controller supplies instantaneous 6-phase trapezoidal current waveforms as a function of rotor position with the zero position of the machine taken into account. So with the rotor locked at a certain rotor position, the controller ensures that suitable instantaneous trapezoidal currents are applied to the correct phase windings. With given reference field and torque currents, the controller through the use of a digital hysteresis current controller ensures that the applied currents follow the reference currents. The control block diagram for the inverter static test is as shown in Figure 7.6(a).

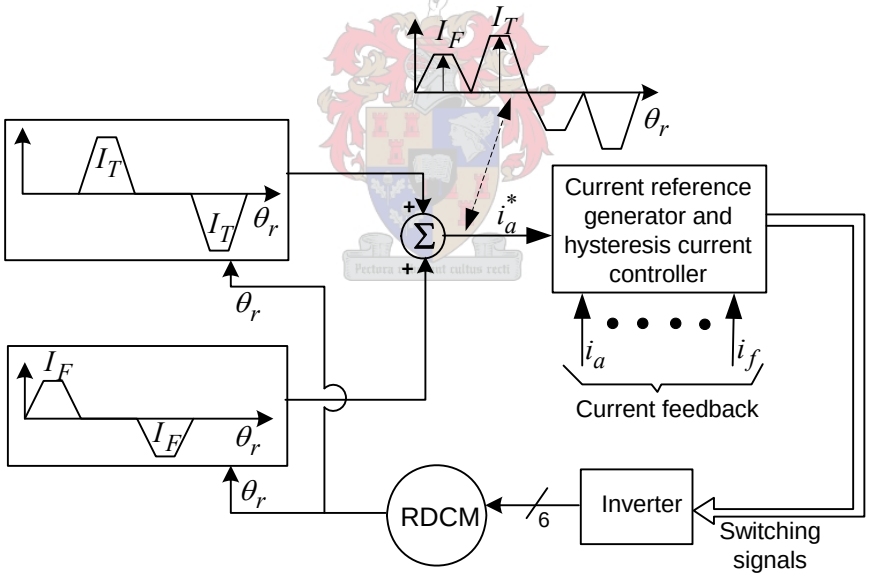

Figure 7.6 (a): Block diagram for the current-controlled 6-phase RDCM for the Inverter static test.

Unlike for the DC static test, the inverter static test was performed with rated field and torque currents of 39 A and 45 A respectively; the results of the test are as shown in Figure 7.6 (b).

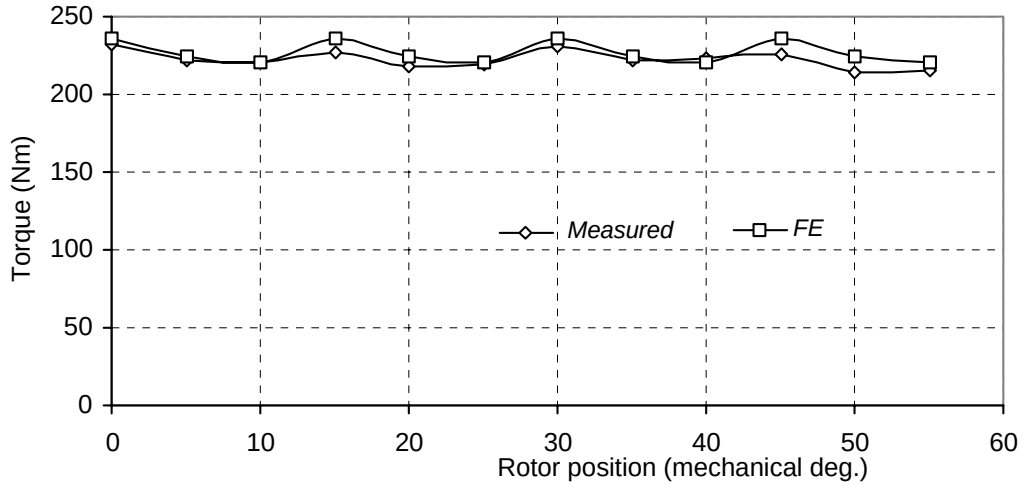

Figure 7.6 (b): Measured and FE-calculated torque versus rotor position for the inverter static test for the 6-phase RDCM with I_F = 39 A and I_T = 45A.

The good agreement of the measured and calculated torque versus position of the 6-phase RDCM does not only further verify the FE analysed machine, most importantly, it validates the electric control system. This then implies that the inverter and the DSP are well suited for the application. With the validated electric drive system, the next step is to perform the running tests of the machine, both at load and no-load conditions.

7.6 Running test

The running tests on the machine for this thesis were carried out under steady-state conditions. The 6-phase RDCM electric drive system was designed to emulate both the separately excited DC motor and the DC series motor. In order to accomplish the emulation of both separately excited DC motor and DC series motor the controller was designed in a way as to control the field and torque currents separately.

The block diagram of the electric drive system controlled in such a way as to emulate a separately excited DC motor, is as shown in Figure 7.7(a). The 6-phase RDCM was designed for a supply voltage of 800 V, but the available supply was only upto 550 V; the machine was therefore was tested at a speed of 800 rpm not 1500 rpm (i.e. rated speed of the machine). For the load of the machine, an eddy current water - cooled dynamometer coupled to the machine was used. The photo of the eddy current dynamometers coupled to the machine can be seen in Figure E.3.

From Figure 7.7(a), it can be observed that the controller is such that a constant field command current, I_F^* is input to the system in the constant flux speed region, but a reduced field command current in the field weakening speed (high) region. The torque command current, I_T^* is load dependent so as such it is controlled by the speed controller. With the field and torque command currents, the controller ensures that the measured phase currents follow the reference currents by the use of the hysteresis current controller.

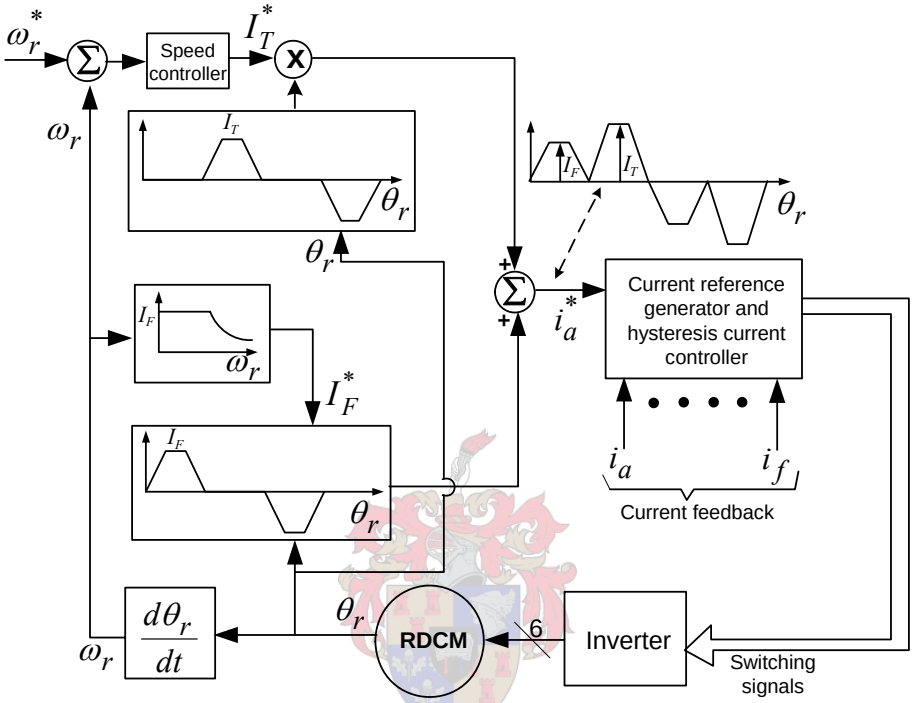

Figure 7.7(a): Block diagram of a current controlled 6-phase RDCM drive emulating separately excited DC motor.

The above test was carried out with different field current values as shown in Figure 7.7(b). It should also be noted from the figure that FE-calculated results are shown in the same figure for comparison purposes.

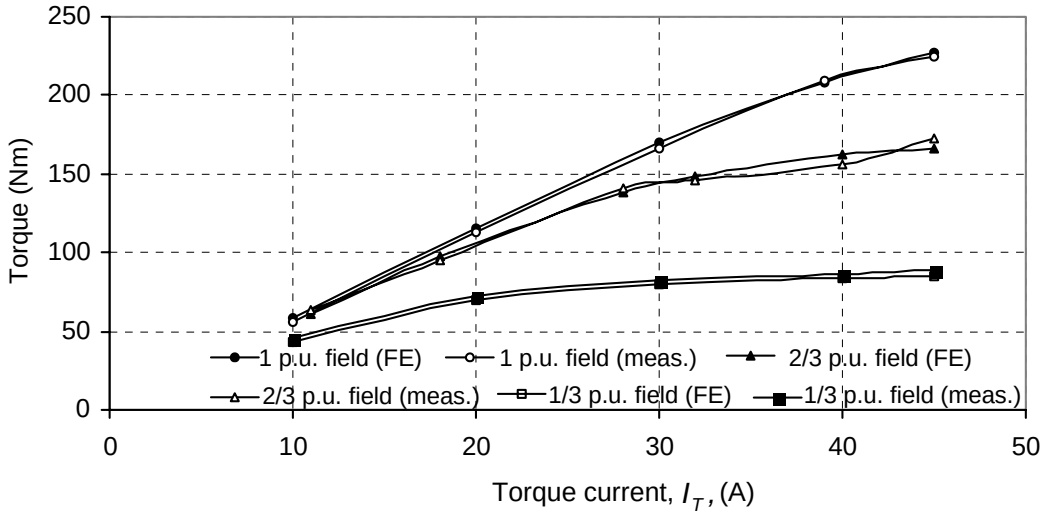

Figure 7.7 (b): Torque performance of the 6-phase RDCM drive with different field currents.

It can be observed from Figure 7.7(b) that the measured and the FE-calculated results do correlate. Furthermore, it is clear that the cross magnetisation effect or armature reaction effect (as in brush dc machine) is severe under field weakening conditions; at rated field current a very much linear relationship between torque and torque current is shown. The measured machine terminal phase voltages with their corresponding phase currents for rated field current only and for rated field and rated torque currents are as shown in Figures 7.7(c) and (d) respectively.

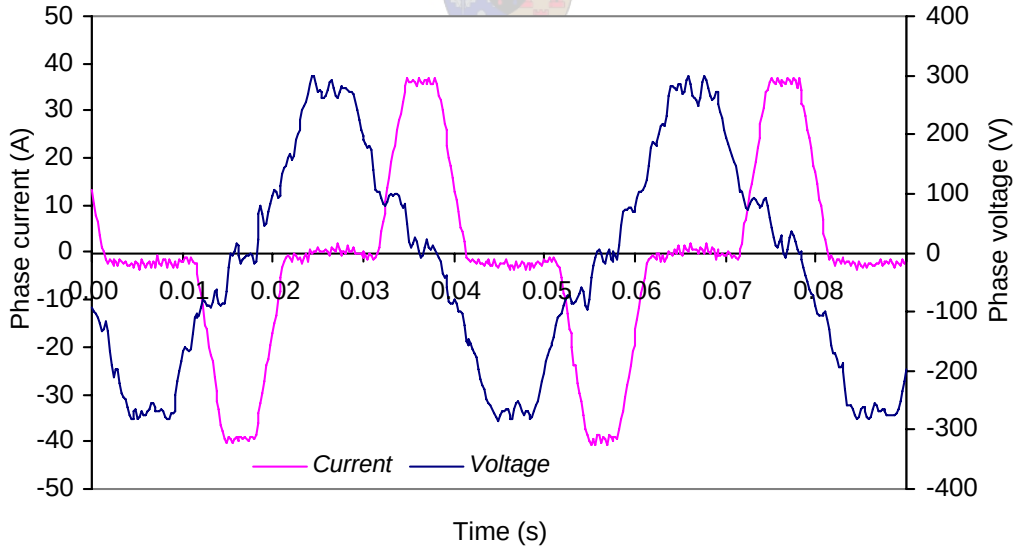

Figure 7.7(c): Measured (filtered) phase supply voltage and phase current for rated field current (I_F = 39 A) only for the 6-phase RDCM.

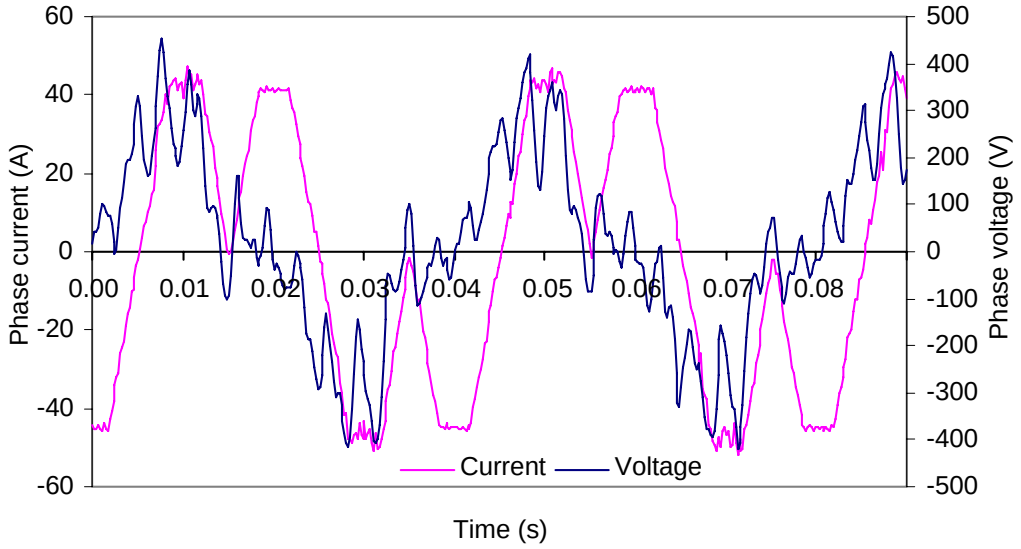

Figure 7.7 (d): Measured (filtered) phase supply voltage and phase current for rated field and torque current (I_F=39A and I_T = 45A) for the 6-phase RDCM.

It can be observed from the figures that the filtered measured phase supply voltage resembles the FE-calculated one in chapter 6 (refer to Figure 6.8(a) and Figure 6.8(b)), which further verifies that the built machine is an exact replica of the FE- analysed machine. The measured phase supply voltages are lower from the calculated phase supply voltages in chapter 6 by a factor (800/1500). This is due to the fact that the FE calculated voltages were calculated at rated speed conditions of 1500 rpm while the measured results are at a de-rated speed of 800 rpm.

The second control strategy whereby the field and torque currents are all controlled by the speed controller was also implemented. The block diagram of the control strategy is as shown in Figure 7.8 (a). As shown from the figure the speed controller controls the field and the torque currents commands. Note that just like for the previous control the machine was only operated at de-rated based speed (800 rpm). The measured and the FE – calculated torque performance of the machine with the control strategy is as shown in Figure 7.8 (b).

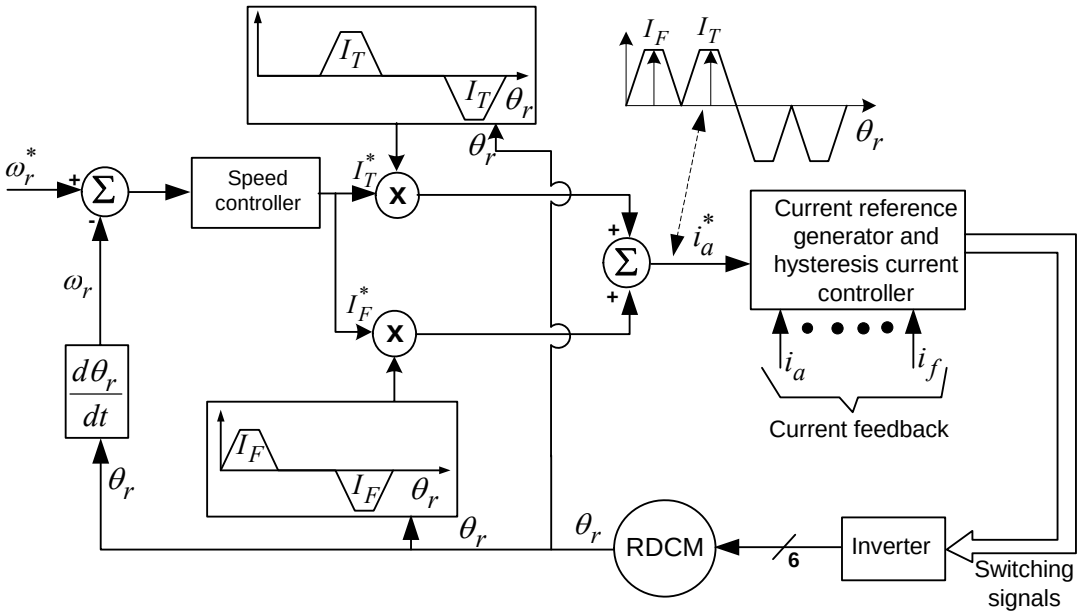

Figure 7.8 (a): Block diagram of a current controlled 6-phase RDCM drive emulating DC series motor.

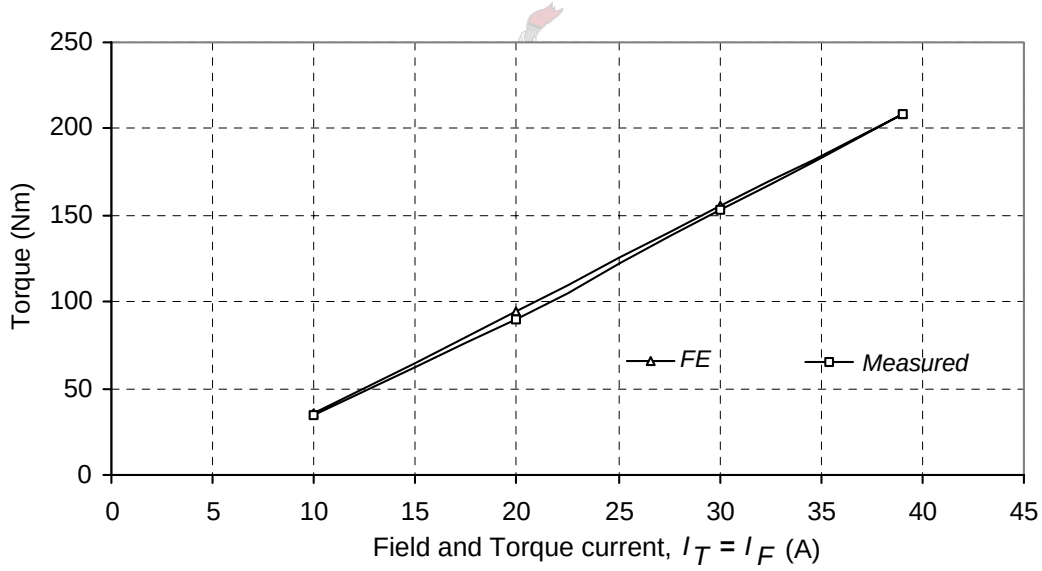

Figure 7.8 (b): Torque performance of the 6-phase RDCM controlled as a DC series motor.

The measured current waveform for the above control strategy for torque and field current of 30 A is as shown in Figure 7.8 (c). There is a noticeable hysteresis band on the current waveform.

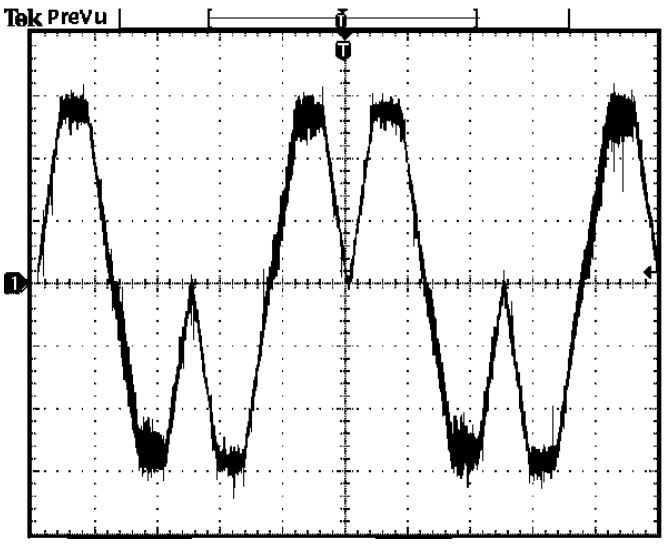

Figure 7.8 (c): Phase current waveform for field and torque current of 30 A (Scale 1:10)

7.7 Field Weakening Test

The torque performance of the machine in the field-weakening region was also investigated. As known from various machine textbooks, the field weakening region is sometimes referred to as the constant power region. This then implies that for the field weakening test, the power output has to be maintained constant with an increase in speed. The test was performed by the use of the first control strategy, whereby the field current is fixed and the torque current is varied as a function of load. With this control strategy at full load conditions, the speed is increased with the torque current kept constant. The increase of speed results in an increase in voltage so to maintain the power output, the field is then reduced so as to maintain the voltage, hence field weakening. The experiment was repeated for different speed values until the supply voltage couldn't be maintained. The results of the investigation are shown in Figure 7.9.

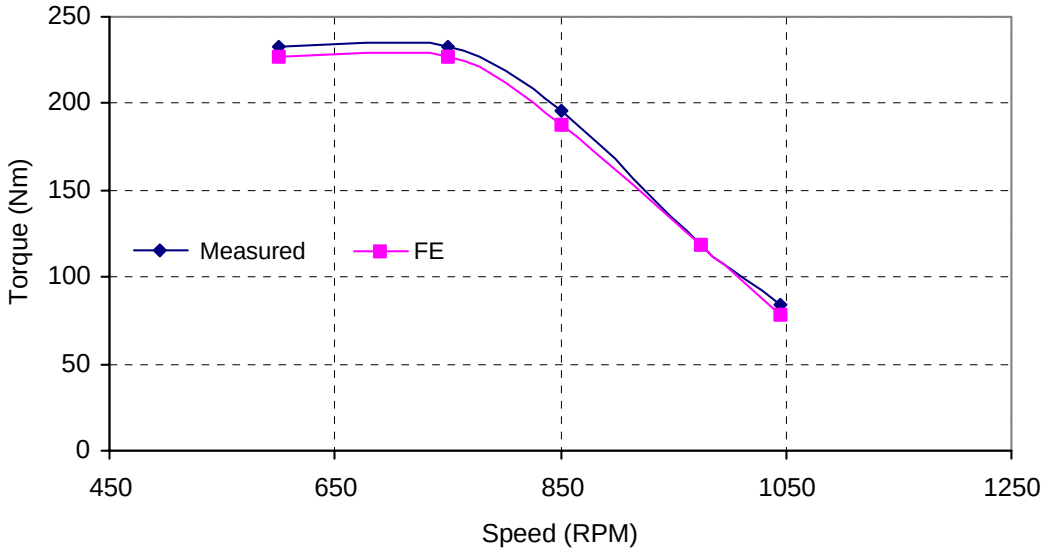

Figure 7.9: Calculated and measured torque versus speed for the 6-phase RDCM.

It can be observed from the figure that the performance of the 6-phase RDCM deteriorates as the field-weakening region is widened. The machine has a poor torque performance in the field–weakening region, it can maintain constant power output up to a speed of 1.4 times base speed. This poor torque performance in the field- weakening region can be improved by the use of a rotor with slits or by pole shaping of the rotor as in brush DC motors.

7.8 Conclusion

The following conclusions are drawn from the experimental test of the 6-phase RDCM under the hysteresis current control:

- It was experienced by the author that the RDCM drive at full load runs silent with low noise.
- It was verified that the RDCM drive with the trapezoidal current waveform can be controlled just like a brush DC machine by separate control of field and torque currents without any complex transformations.
- The measured torque performance of the machine has good correlation with the FE-calculated torque.
- The machine has a poor torque performance in the field weakening region, it can maintain constant power output up to a speed of 1.4 times base speed.

Chapter 8 Summary with Conclusions and Recommendations

The contribution of this thesis can be summarised as the critical evaluation of the torque performance of the optimum designed reluctance DC machine in motoring mode under current control. In the evaluation of the torque performance of the machine finite element (FE) based design optimisation of the current controlled RDCM is implemented. As a basis for the torque performance of the optimum designed RDCM the torque performance of the optimum designed sinusoidal RSMs under the same copper losses and stack volume is performed. It also compares the torque performance of the optimum designed RDCM to optimum designed sinusoidal RSM more especially the optimum designed 5-phase with the injection of third harmonic current. In optimally designing the machines, an FE based Powell design optimisation method is used to optimise the machine in multi-dimensions with torque as the objective function.

The optimum 6-phase RDCM with a skewed rotor has also been built and tested so as to verify the FE calculations and also to prove some important characteristics of the RDCM. The results and conclusions about the optimum design and torque performance of both the sinusoidal RSMs and RDCMs are summarised in the sections below. Recommendations for future work on this particular topic are made in section 8.7.

8.1 Review of sinusoidal RSMs

The steady state *dq* voltage equations of the 3-phase, 5-phase and the 5-phase RSMs with the addition of third harmonic currents are derived in Chapter 2. The torque equations of the machines are also presented and it was shown that the torque equation of a 5-phase with the injection of third harmonic currents RSM is made up of the fundamental torque component and the third harmonic torque component. In addition to the above, the major contribution of chapter 2 is the development of the FE method of determining the equivalent circuit parameters of the steady state *dq* equivalent circuit diagrams, more especially the *dq* flux linkages for the different RSMs. The determination of the fundamental and the third harmonic *dq* flux linkages are of critical importance, more especially for the 5-phase + 3rd RSM for the torque calculation of the machine.

8.2 Torque performance of sinusoidal RSMs

An unconstrained optimisation was carried out for the 3-phase, 5-phase and 5-phase + 3rd RSMs to maximise the torque per copper losses and stack volume with two different rotor

structures as explained in Chapter 3. The rotors studied are the salient pole rotor with no internal flux barriers and the round rotor with internal barriers. The major reason for the analysis of the machines with two different rotor structures is to facilitate the selection of the rotor structure for the RDCMs. All rotors studied are normal transverse laminated rotors. The optimisation algorithm used for the design optimisation of the machines is Powell's algorithm, and some of the results found from the method are as follows:

- In the optimisation process, the mesh changes as the optimisation progresses as and there is a possibility of the elements being badly shaped, which can then affect the accuracy of the process. However, this was not experienced in this research, as the optimisation variables do not change much in the search for the optimum.
- It has been proven that it is feasible to carry out an overall (stator and rotor) unconstrained optimisation of the sinusoidal RSMs, more especially the 5-phase + 3rd RSM using the finite element method directly in the optimisation procedure.

The conclusions that can be drawn from the torque performance of the optimum designed sinusoidal RSMs are as follows:

- With the same rotor structure, the optimum 5-phase RSMs develop slightly more torque than the 3-phase RSM.
- Under sinusoidal 3- and 5-phase conditions, the RSMs with the internal flux barrier reluctance rotor develop more than 33% torque as compared to the RSMs with the cut-out reluctance rotor.
- The 5-phase with the injection of third harmonic currents and using the cut-out reluctance rotor results in only 3.7% increase in torque as compared to the same machine with sinusoidal currents. However, with the internal flux barrier rotor the torque decreases by 3.6%. Thus, it means that the torque performance of the 5-phase with an injection of third harmonic currents depends on the rotor structure.
- Even though there is an increase in torque due to the injection of the 3rd harmonic current in the case of the 5-phase with the cut-out reluctance rotor, the 3-phase RSM with the internal flux barrier rotor still outperforms this machine by almost 24%.
- It has also been shown that optimum designed sinusoidal RSM with more slots per phase (i.e. distributed winding) yielded a higher torque per copper loss as compared to those with concentrated winding.
- From the good agreement of the measured and the FE calculated results for the flux barrier rotor RSM, it can be seen that FE calculated results can be relied upon.

8.3 Reluctance DC Machines

In chapter 4 the working principle of the reluctance DC machine was developed based on the working principle of the permanent magnet DC machine. The major contribution of chapter 4 is the formulation of the criteria for selecting the best current waveform for the RDCM based on the rotating airgap MMF analysis. Based on this criterion, it was shown that the trapezoidal current waveform is the best current waveform for the RDCM drive in comparison to the well-known square current waveform and the half-sinusoidal current waveform. This is based on the fact that it resulted in a continuous smooth rotating MMF. In addition to the above, the torque equation of the RDCM was derived based on the Lorentz law; this equation turned out to be similar to that of brush DC machines.

8.4 Torque performance of Reluctance DC machines

The trapezoidal current waveform was further verified as the best current waveform (as compared to the square current waveform) in the sense that it resulted in a lower torque ripple and higher torque per copper loss. It was shown in chapter 5 that the optimum designed 5-phase RDCM with the trapezoidal current waveform developed a slightly higher torque than that of the optimum designed 5-phase RDCM with the square current waveform. But most importantly the ripple torque of the optimum designed skewed 5-phase RDCM with the trapezoidal current waveform was found to be 16% lower than that of the optimum designed 5-phase RDCM with the square current waveform. It was also found that the maximum torque with the same copper losses and stack volume of the machine with the trapezoidal current waveform is close (4% lower) to that of the optimum designed 5-phase RSM with the injection of third harmonic currents. The 6-phase RDCM drive is better to use than its 5-phase counterpart due to the fact that for maximum torque per copper loss, the optimum designed 6-phase machine resulted in an I_F/I_T ratio close to unity. This implies that the required current capability of the full-bridge inverter during field mode is close to the required current capability during torque mode.

With the optimum designed 6-phase RDCM, it was further found that the torque per copper loss per stack volume of the machine is similar (1.3% higher) to that of the optimum designed 5-phase RSM with the injection of third harmonic current. The optimum I_F/I_T ratio for maximum torque with different rotor structures (normal salient pole rotor, salient pole rotor with slitted poles and the salient pole rotor with chamfered pole tips) was found to be between 0.85 – 0.88. It was also shown that the torque calculated based on the Lorentz force law is in agreement with the FE Maxwell stress tensor method. Lastly, it was found that the optimum

designed 6-phase RDCM with normal salient pole rotor has a severe armature reaction effect. It was shown that using slitted or chamfered salient pole rotors can reduce this armature reaction effect. This then improves the torque per copper loss output of the machine by 6 %.

8.5 Per-phase equivalent circuit modelling of the 6-phase RDCM

In chapter 6 the per-phase equivalent circuit parameters are determined by the use of FE analysis for both no-load and load conditions. The parameters determined are the per-phase inductances and voltages (both back EMF and supply voltage). It was shown that the determined parameters as a function of rotor position under load conditions do contain a ripple content that corresponds to the current commutation of the trapezoidal current waveform. It was also shown that the torque calculated from the instantaneous FE calculated back EMF and current, and the torque calculated directly by the FE Maxwell stress tensor method are in good agreement. This verifies the per-phase equivalent circuit model of the machine.

8.6 Measured and calculated Results

An optimum designed 6-phase RDCM with a skewed salient pole rotor was built. Photos of the stator and the rotor of the machine are as shown in appendix E. With the machine under the hysteresis current control, the following conclusions are drawn from the drive system:

- It was experienced by the author that the RDCM drive at full load runs silent with low noise.
- It was verified that the RDCM with the trapezoidal current waveform can be controlled with separate control of field and torque currents just like a brush DC machine without any complex transformations.
- The measured torque performance of the machine shows good correlation with the FE – calculated torque.
- The machine has a poor torque performance in the field-weakening region; it can maintain constant power output up to a speed of 1.4 times base speed.

8.7 Recommendations

It is recommended that the following further research be carried out on RDCM drives:

- Further investigation on the performance of the machine with a salient pole rotor with slitted field poles and chamfered pole arc tips. The investigation carried out in this thesis considered the slitted poles and chamfered poles separately.
- Investigation of the RDCM in generator mode as the current investigation was focussed on the machine in the motoring mode.
- Further extension of the 6-phase RDCMs to 7-phase RDCMs with trapezoidal current waveform with the ratio of field phase winding to torque phase winding of 3:4. This might in a way improves on the I_F/I_T ratio, which ideally must be unity.
- With the FE-calculated parameters, a suitable PI controller can be designed for the current control of the machine. For this thesis, a hysteresis current controller was used.
- Investigation of the use of the RDCM drives in high power and high speed applications.

R References

Abdel-Razek (1981), A.A., Coulomb, J.L., Feliachi, M. and Sabonnadiere, J.C.: "The calculation of the electromagnetic torque in saturated electric machines within combined numerical and analytical solutions in the field equations", *IEEE Trans. on Magnetics*, vol. 17, no. 6, pp. 3250-3252, Nov. 1981.

Abdel-Razek (1982), A.A., Coulomb, J.L. and Sabonnadiere, J.C.: "Conception of an air-gap element for the dynamic analysis of the electromagnetic field in electric machines", *IEEE Trans. on Magnetics*, vol. 18, no. 2, pp. 655-659, March 1982.

Alhamadi (1991), M.A. and Demerdash N.A.: "Modelling of effects of skewing of rotor mounted permanent magnets on the performance of brushless DC motors", *IEEE Trans. on Energy Conversion*, vol. 6, no. 4, pp. 721-729, 1991.

Andersen (1967), O.W.: "Optimum design of electrical machines", *IEEE Trans. PAS*, vol. 86, no. 6, pp. 707-711, June 1967.

Andersen (1992), O.W.: "Optimal design of induction motors", *Int. Aegean Conf. on Electrical Machines and Power Electronics*, vol. 2, pp. 763-768, May 1992.

Anvari (1985), H.A., Faucher J. and Trannoy B.: "An investigation into the influence of a cross-coupling effect on reluctance machine performance", *Int. Conf. on Electrical Machines – design and applications*, IEE, vol. 254, pp. 70-75, 1985.

Binder (1989), A.: "Untersuchung zur magnetischen kopplung von Längs- und Querachse durch sättigung am beispiel der reluktanzmaschine", *Arch. Elektrotech.*, vol. 72, pp. 277-282, 1989.

Boldea (1991), I., and Nasar S.A.: "Emerging electric machines with axially laminated anisotropic rotors: A review", *Electric Machines and Power systems Journal 19*, pp. 673-703, Hemisphere Publishing corporation, 1991.

Boldea (1996), I.: "*Reluctance synchronous machines and drives*", Clarendon press, Oxford, 1996.

Bomela (2002), X.B. and Kamper M.J.: "Effect of stator chording and rotor skewing on performance of reluctance synchronous machine", *IEEE Trans. Ind. Appl. Soc.* (IAS), vol. 38, no. 1, pp. 91-100, Jan. 2002.

Brinkman (1965), J.: "*Theoretische and experimentelle untersuchungen an einem motor mit verbesserter ausnuzung des reaktionsprinzips*", Dissertation, Fakultät für Maschinenwesen der Technischen Hochschule Carolo-Wilhelmina, Braunschweig, Jan. 1965.

Buso (1998), S., Malesani L. and Mattavelli P.: "Comparison of current control techniques for active filter applications", *IEEE Trans. on Indus. Applications*, vol. 45, no. 5, Oct. 1998.

Chapman (1991), S.J.: "*Electric machinery fundamentals*", McGraw-hill international, second edition, 1991.

Chiricozzi (1996), E., Conti G., Parasiliti F. and Villani M.: "Design solutions to optimise torque ripple in synchronous reluctance motors", *Proc. ICEM'96*, Vigo (spagna), pp. 148-153, 1996.

Conti (1996), G., Parasiliti F. and Villani M.: "Torque ripple analysis in synchronous reluctance motors", *ELECTROMOTION 3* (1996), pp. 188-193, 1996.

El-Antably (1985), A. and Hudson, T.L.: "The design and steady-state performance of a high efficiency reluctance motor", *IEEE-IAS Annual meeting*, pp. 770-776, 1985.

Fitzgerald (1990), A.E., Kingsley C. and Umans S.D.: "*Electric machinery*", 5th edition, Mc Graw Hill, New York, 1990.

Flack (1994), T.J. and Volschenk A.F.: "Computational aspects of time-stepping finite-element analysis using an airgap element", *ICEM*, Sept. 1994.

Fratta (1995), A., Troglia G.P., Vagati A. and Villata F.: "Torque ripple evaluation of high-performance synchronous reluctance machines", *IEEE-IAS Magazine*, pp. 14-22, July/Aug. 1995.

Haataja (2003), M.J.: "*A comparative performance study of four-pole induction motors and synchronous reluctance motors in variable speed drives*", *Ph.D. dissertation*, Lappeenranta University of Technology, June 2003.

Hendershot Jr. (1994), J.R. and Miller T.J.E.: "*Design of brushless permanent-magnet motors*", Claredon press, Oxford, 1994.

Hindermarsh (1984), J.: "*Electrical machines and their applications*", Butter-Heinemann Ltd (Oxford), fourth edition, 1984.

Honsinger (1971), V.B.: "The inductances L_d and L_q of reluctance machines", *IEEE Trans. PAS*, vol. 90, no. 1, Jan. 1971.

Hooke (1961), R. and Jeeves, T.A.: "Direct search solution of numerical and statistical problem", *Journal of ACM*, vol. 8, pp. 212, 1961.

Ishak (2005), D., Zhu Z.Q. and Howe D.: "Permanent-magnet brushless machines with unequal tooth widths and similar slot and pole numbers", *IEEE Trans. on IAS*, vol. 41, no. 2, March/April 2005.

Kamper (1994), M.J. and Volschenk, A.F.: "Effect of rotor dimensions and cross magnetisation on L_d and L_q inductances of reluctance synchronous machine with cageless flux barrier rotor", *IEE Proc.-Electr. Power Appl.*, vol. 141, no. 4, pp. 213-220, July 1994.

Kamper (1995), M.J. and Mackay A.T.: "Optimal control of the reluctance synchronous machine with a cageless flux barrier rotor", *Trans. S.A. of the South African Institute of Electrical Engineers*, vol. 86, no. 2, pp. 49-56, June 1995.

Kamper (1996), M.J.: "*Design optimisation of cageless flux barrier rotor reluctance synchronous machine*", *Ph.D. dissertation*, University of Stellenbosch, Dec. 1996.

Kazmierkowski (1998), M.P. and Malesani L.: "Current control techniques for three-phase voltage-source PWM converters", *IEEE Trans. on Indus. Electronics*, vol. 45, no. 5, Oct. 1998.

Kosto (1923), J.K.: "Polyphase reaction synchronous motors", *Journal AIEE*, vol. 42, pp. 1162-1168, 1923.

Krause (1986), P.C.: "*Analysis of Electric machinery*", Mc Graw-Hill Book Company, 1986.

Law (1994), J.D., Chertok A. and Lipo T.A.: "Design and Performance of field regulated Reluctance machine", *IEEE Trans. on Industry Appl.*, vol. 30, no. 5, Sept./Oct. 1994.

Law (1996), J.D., Busch T.J. and Lipo T.A.: "Magnetic circuit modelling of the field regulated reluctance machine Part 1: Model development", *IEEE Trans. on Energy Conversion*, vol. 11, no. 1, March 1996.

Busch (1996), B.J., Law J.D. and Lipo T.A.: "Magnetic circuit modelling of the field regulated reluctance machine Part II: Saturation modelling and results", *IEEE Trans. on Energy Conversion*, vol. 11, no. 1, March 1996.

Lawrenson (1964), P.J.: "Theory and performance of polyphase reluctance machines", *Proc. IEE*, vol. 111, no. 8, pp. 1435-1445, Aug. 1964.

Li (1990), C. and Rahman A.: "Three-phase induction motor design optimisation using the modified Hooke-Jeves method", *Electric Machines and Power Systems*, vol. 18, pp. 1-12, 1990.

Manjrekar (2000), M.D., Steimer P.K. and Lipo T.A.: "Hiybrid multivel power conversion system: A competitive solution for high-power applications", *IEEE Trans. on Indus. Applications*, vol. 36, no. 3, May/June 2000.

Matsuo (1994), T. and Lipo, T.A.: "Rotor design optimisation of synchronous reluctance machine", *IEEE Trans. on Energy Conversion*, vol. 9, no. 2, pp. 359-365, June 1994.

Mayer (1986), R., Mosebach H., Schröder U. and Weh H.: "Inverter-fed multiphase reluctance with reduced armature reaction and improved power density", *Proc. of the ICEM'86 (Munchen)*, part 3, pp. 1138-1141, Sept. 1986.

Miller (1991), T.J.E., Huston A., Cossar C. and Staton D.A.: "Design of synchronous reluctance motor drive", IEEE Trans. on Industrial Applications, vol. 27, no. 4, July 1991.

Mohan (2001), N.: "*Electric drives: An integrative approach*", MNPERE, Minneapolis, 2001.

Powell (1964), M.J.D.: "An efficient method for finding the minimum of a function of several variables without calculating derivatives", *Computer Journal*, vol. 7, pp. 155-162, 1964.

Parasiliti (1993), F. and Villani M.: "Optimised design of a double-cage induction motor", *Int. Conf. on Electrical Machines in Australia* (ICEMA), Adelaide, pp. 81-86, Sept. 1993.

Parasiliti (1995), F. and Villani M.: "Optimisation analysis of synchronous reluctance motor design", *IEE Electrical Machines and Drives Conf. Publication No. 412*, Sept. 1995.

Rakgati (2006), E.T. and Kamper M.J.: "Torque performance of optimally designed three and five-phase reluctance synchronous machines with two rotor structures", *Trans. SAIEE*, on printing, July 2006.

Ramamoorty (1979), M. and Rao P.J.: "Optimisation of polyphase segmented-rotor reluctance motor design: a nonlinear programming approach", *IEEE Trans. PAS*, vol. 98, no. 2, pp. 527-535, March/April 1979.

Schittkowski (1981), K.: "The nonlinear programming method of Wilson, Han and Powell with an augmented Lagrangian type line search function", *Numerische Mathematik*, vol. 38, pp. 83-114, 1981.

Singh (1992), C. and Sarkar D.: "Practical considerations in the optimisation of induction motor design", *IEE Proceedings-B*, vol. 139, no. 4, pp. 365-373, July 1992.

Thompson (1911), S.P.: "*Dynamo electric machinery*", M. Strong (New York, N.Y.), eighth edition, pp. 389 (Fig. 264), 1911.

Toliyat (1992), H.A., Xu L. and Lipo T.A.: "A five phase reluctance motor with high specific torque", *IEEE Trans. on IAS*, vol. 28, no. 3, pp. 659-667, May/June 1992.

Toliyat (1998), H.A., Waiker P.S. and Lipo T.A.: "Analysis and simulation of five phase synchronous reluctance machines including third harmonic airgap MMF", *IEEE Trans. on IAS*, vol. 34, no. 2, pp. 332-339, March/April 1998.

Toliyat (2000), H.A., Shi R. and Xu H.: "A DSP-based vector control of five-phase synchronous reluctance motor", *IEEE IAS Conf. record* – 2000, pp. 1-8, 2000.

Vagati (2000), A., Canova A., Chiampi M., Pastorelli M. and Repetto M.: "Design refinement of synchronous reluctance motors through finite-element analysis", *IEEE Trans. Industry Applications*, vol. 36, no. 4, pp. 1094-1101, July/August 2000.

Vagati (1992), A., Franceschini G., Marongiu I. and Troglia G.P.: "Design criteria of high performance synchronous reluctance motors", *IEEE-IAS Annual Meeting Record*, pp. 66-73, Sept. 1992.

Volschenk (1993), A.F.: "*Finite element analysis of a salient-pole generator feeding a rectifier load*", Ph.D. dissertation, University of Cambridge, March 1993.

Weh (1984), H.: "*Zur Weiterentwicklung wechselrichter-gespeister reluktanzmaschinen fur hohe leistungs-dichten und grobe leistung*", ETZ Archiv, vol. 6, no. 4, pp. 135-141, 1984.

Weh (1985), H. and Schroder U.: "Static inverter concepts for multiphase machines with square-wave current field distributions", *European Power Electronic Conf. (Brussels)*, pp. 1147-1152, October 1985.

Weh (1990), H., Mosebach W., Niemann W. and Tareilus A.: "Field control in synchronous machines with permanent magnet excitation in flux concentration mode", *Proc. ICEM* (Cambridge), 1990.

Williamson (1994), S., Flank T.J. and Volschenk A.F.: "Representation of skew in time-stepped two-dimensional finite element models of electrical machines", *IEEE-IAS Annual Meeting Record*, pp. 143-148, 1994.

Xu (1992), L.: "Rotor structure selections of non-sine five-phase synchronous reluctance machines for improved torque capability", *IEEE Trans. on IAS*, vol. 36, no. 4, pp. 1111-1117, July/Aug. 1992.

Xu (2000), L. and Fu W.N.: "Evaluation of 3rd harmonic component effects in 5-phase synchronous reluctance motor drive using time stepping finite element method", *IEEE-IAS Conf. record*, pp. 1-8, 2000.

Xu (1991), L., Xu X., Lipo T.A. and Novotny D.W.: "Vector control of a synchronous reluctance motor including saturation and iron loss", IEEE Trans. Industry Applications, vol. 27, no. 5, pp. 977-987, Sept. 1991.

A Finite Element program and Calculation of Phase Flux Linkage, Airgap Flux Density and Torque

In this appendix the finite element program and the calculation of the total flux linkage of a phase winding, the calculation of the airgap flux density and the calculation of the torque are briefly described.

A.1 The finite element program

The finite element software used in this study is a non-commercial package. The package has been developed at Cambridge University. The FE analysis makes use of triangular elements of the 1st order. Only one pole of the machine is meshed with one airgap macro-element [Abdel-Razek (1982)] comprising nodes on both sides of the airgap as shown in Figure A.1.

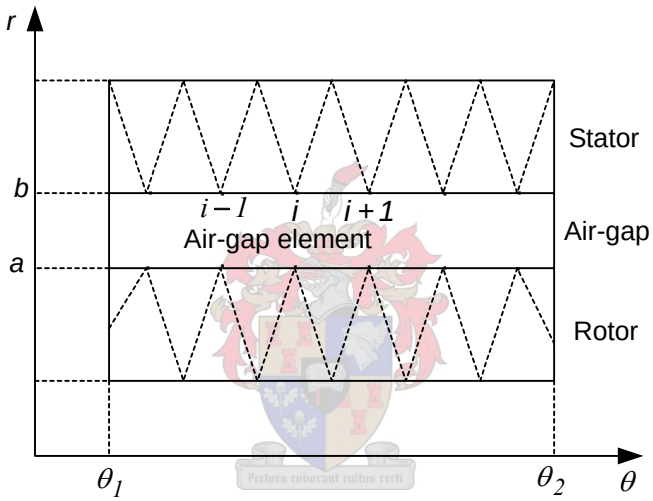

Figure A.1: Special air-gap element with periodicity at θ_1 and θ_2 and conformity with rotor and stator finite elements.

The rotor movement is modelled by the use of one airgap element as devised by Volschenk (1993) and later followed by Flack (1994). The Newton-Raphson method is used for the solution of the set of non-linear equations. The FE solution procedure follows the following steps:

- *Mesh generation*

The mesh generation involves division of machine cross-section into a set of triangular elements. The accuracy of the FE solution is dependent on the topology of the mesh, thus, attention should be placed in the creation of the mesh. The creation of the mesh for the stator is done in such a way that only one stator slot of the machine is outlined in terms of x-y coordinates and meshed and mirrored to the number of stator slots over a pole pitch.

Thereafter to complete the stator model, the phase windings are allocated to the respective slots. For the rotor, just like for the stator, half of the rotor structure is outlined and meshed and mirrored to the other half.

- *Pre-processing*

Under the pre-processing the following main tasks are performed which are the material definition, the setting of the boundary conditions and the problem definition.

- *Solving*

The Newton-Raphson method is used to solve for the magnetic vector potentials at different nodes. It is a set of non-linear equations due to the non-linearity of the magnetic materials.

- *Post-processing*

From the known nodal magnetic vector potentials, the flux linkages, inductances, airgap flux density and the torque of the machine can be calculated as given in sections A.2-A.4.

A.2 Calculation of the total phase flux linkage

The flux linkage of a coil with z-turns, coil area, S, and length, l, along the z-direction in terms of finite elements using first order triangular mesh as given by Kamper (1996) is given by:

$$\lambda = z\phi = z\sum_{j=1}^{n}\frac{\Delta_j}{S}\left(\zeta\frac{1}{3}\sum_{i=1}^{3}A_{ij}\right)l, \tag{A.1}$$

where A_{ij} is the magnetic vector potential of nodal point $i = 1$, $i = 2$ or $i = 3$ of the triangular element j. The direction of integration either into the plane or out of the plane is given by ζ = +1 and ζ = -1 respectively. Δ_j is the area of the triangular element j and n is the total number of elements of the in-going and out-going areas of the coil being meshed.

With reference to equation (A.1) for an electric machine with only one pole meshed, the total flux linkage of a phase winding is given as follows:

$$\lambda_{phase} = \frac{2pzl}{n_a S}\sum_{j=1}^{u}\left(\frac{\Delta_j\zeta}{3}\sum_{i=1}^{3}A_{ij}\right), \tag{A.2}$$

with u being the total number of elements of the meshed coil areas of the phase in the pole region.

A.3 Calculation of the airgap flux density

The flux density vector can be expressed in terms of cylindrical coordinates as from Kamper (1996) is given by the following equation:

$$B = \left(\frac{1}{r}\frac{\partial A_z}{\partial \theta}\right)a_r + \left(-\frac{\partial A_z}{\partial r}\right)a_\theta , \tag{A.3}$$

where a_r is the unit vector directed radially outwards, perpendicular to the cylindrical surface, a_θ is the unit vector that points in the direction of increasing θ, tangential to the cylindrical surface. With equation (A.3), it then implies that the radial airgap flux density at the stator inner surface is as follows:

$$B_{gn}(\theta) = \frac{2}{d_i}\frac{\partial A_z}{\partial \theta} \tag{A.4}$$

With the finite-difference approximation, the partial derivative of A_z with respect to θ is as given by the following equation:

$$\frac{\partial A_z}{\partial \theta} = \frac{A_z(\theta+\delta) - A_z(\theta)}{\delta} \tag{A.5}$$

With the known nodal values in terms of the magnetic vector potentials at the stator inner surface, the radial airgap flux density between nodal points *i and i+1* can be determined by the use of equations (A.4) and (A.5) as follows:

$$B_{gn}(\theta) = \frac{2}{d_i}\left(\frac{A_{z(i+1)} - A_{z(i)}}{\theta_{(i+1)} - \theta_{(i)}}\right) \tag{A.6}$$

Bearing in mind that the angles of equation (A.6) are electrical angles and that only a pole is meshed. It then implies that the airgap flux density is known for a pole pitch (half a cycle). However, with negative periodicity where

$$B(r,\theta+\pi) = -B(r,\theta) , \tag{A.7}$$

the flux density is as such known over 2 pole pitches.

A.4 Calculation of the electromagnetic torque

By definition of the Maxwell stress tensor method as described by Abel-Razek (1981) the total electromagnetic torque in the air-gap of the electric machine can be determined by the line integral along a closed path located in the air-gap as given by the following equation:

$$T_e = \frac{p r^2 l}{\mu_0} \int_{\theta_1}^{\theta_2} B_r B_\theta \, d\theta, \tag{A.8}$$

where r is the radius of the arbitrary circumference which lies in the air-gap, l is the stack length of the machine, p is the number of pole pairs of the machine, B_r is the radial component of the flux density and the B_θ is the tangential component of the flux density. The flux density in the air-gap is computed by derivatives of the expansion of the shape functions. Thus the electromagnetic torque is given by

$$T_e = \frac{-p l}{\mu_0} [A]_e^T [T][A]_e, \tag{A.9}$$

where $[A]_e$ is the vector of nodal values of the vector potential in the air-gap and $[T]$ is the matrix defined by

$$t_{ij} = \frac{\theta_2 - \theta_1}{2} \sum_{n=1}^{\infty} k^2 \frac{(r/c)^k + (c/r)^k}{(c'/c)^k - (c/c')^k} \frac{(r/g)^k - (g/r)^k}{(g'/g)^k - (g/g')^k} (a_{in} b_{jn} - b_{in} a_{jn}), \tag{A.10}$$

where

$$k = \frac{2\pi n}{\theta_2 - \theta_1}.$$

Referring to Figure A.1 that shows the air-gap element with periodicity at θ_1 and θ_2 and conformity with rotor and stator finite elements, the parameters of equation (A.10) are defined as follows:

$c = a$, $c' = b$ when i is on the stator interface

$c = b$, $c' = a$ when i is on the rotor interface

The same applies for g and g' but unlike for c and c', g and g' are for node j. And a_{in}, b_{in}, a_{jn} and b_{jn} are the fourier coefficients of the shape functions at node i and j respectively.

B Calculation of the number of turns per phase and the diameter of the conductor used for the winding

In this appendix, the calculation of the number of turns and the size of the conductor to be used for the practical machine are briefly described.

B.1 Calculation of Number of turns per phase

The number of turns per phase, *N*, is calculated based on equation (B.1) where *E* is the induced voltage in a phase winding, φ_p is the average flux per pole, *f* is stator voltage frequency and k_w is the winding factor.

$$E = 4.44\, f\, k_w\, N\, \varphi_p \tag{B.1}$$

The average flux per pole for a 4-pole machine is given as

$$\varphi_p = \frac{\pi}{2} B\, r\, l, \tag{B.2}$$

where *B* is the average flux density, *r* is the stator inner radius and *l* is the stack length of the machine. For the practical machine the stator inner radius and the stack length are as follows:

$$r = \frac{d_i}{2} = \frac{0.1961}{2} = 0.098m$$

$$l = 0.175m$$

With the above machine specifications, winding factor of 0.87 and the average flux density in the stator teeth assumed to be 0.8 T, the number of turns can then be calculated as follows from equations (B.1) and (B.2) [the designed voltage for a phase winding is taken as 400 V].

$$N = \frac{400}{4.44*50*0.87*(\pi/2)*0.8*0.098*0.175}$$
$$= 96 \text{ turns}$$

This then implies that the number of turns per pole per phase is **96 turns.**

B.2 Calculation of the Conductor size

The FE software adapted for the machine analysis is programmed in such a way that with the slot dimensions and the fill factor, it calculates the cross sectional area of a single conductor, A_{sc}. For the practical machine this is:

$$A_{sc} = 2.6079393 \times 10^{-6}\, \mathrm{m}^2 .$$

With the A_{sc} known, the conductor diameter, *d*, of the conductor is calculated by

$$\begin{aligned} d &= 2\sqrt{\frac{A_{sc}}{\pi}} \\ &= 2\sqrt{\frac{2.6079393\times10^{-6}}{\pi}} \\ &= 1.82\,mm \end{aligned} \tag{B.2}$$

A conductor diameter of 1.82 mm is difficult to wind and also have a high skin effect as compared to a conductor with a smaller diameter. The above problem was then avoided by using 4 conductors in parallel. The diameter of the single conductor is given by

$$\begin{aligned} d &= 2\sqrt{\frac{A_{sc}}{4\pi}} \\ &= 2\sqrt{\frac{2.6079393\times10^{-6}}{4\pi}} \\ &= 0.91mm \end{aligned} \tag{B.3}$$

In conclusion, four conductors in parallel with a single conductor diameter of **0.91 mm** were used for the windings of the practical machine.

C Construction of the 6-phase full bridge Inverter

In Figures C.1 the details of the inverter that shows more especially the SKH121 driver circuitry and the DC bus layout are shown. The finished product of the rectifier and inverter used for the RDCM drive are also shown in Figure C.2.

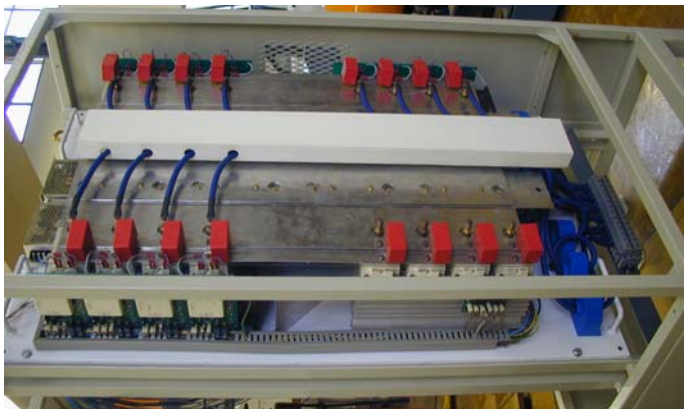

Figure C.1: The 6-phase full bridge inverter showing the SKH121 driver circuitries and DC-bus layout.

Figure C.2: The complete rectifier and 6-phase full bridge inverter used for the RDCM drive system.

D Construction of the 35 kW reluctance DC machine

In Figures D.1-D.3 the photos of the optimum designed stator and the rotor laminations, the assembled skewed rotor and the stator of the 6-phase RDCM are shown.

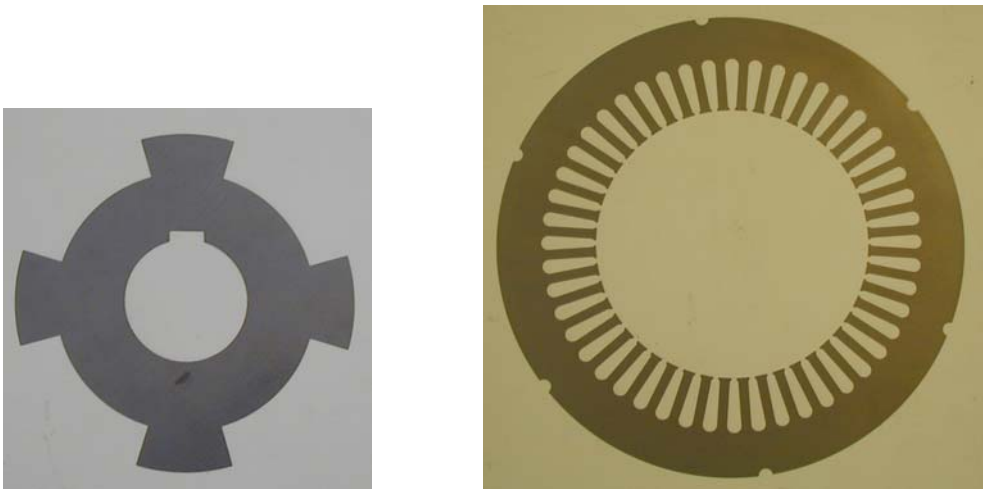

(a) (b)

Figure D.1:(a) rotor and (b) stator laminations of the reluctance DC machine.

Figure D.2: Skewed rotor of the reluctance DC machine.

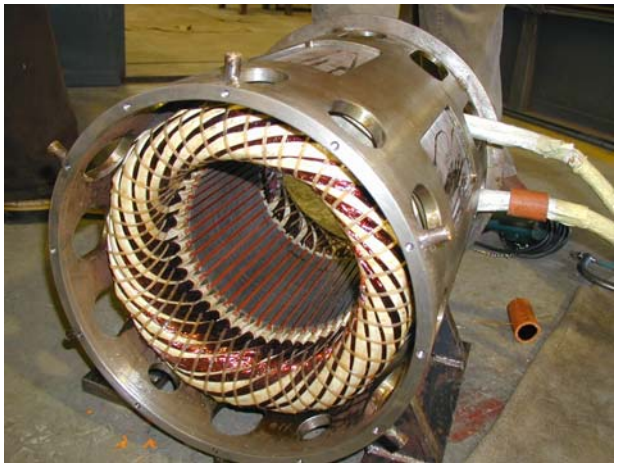

Figure D.3: Stator of the reluctance DC machine.

E Photo album of the DSP controller unit, RDCM under blocked rotor test and the Eddy-current Dynamometer

In Figures E.1-E.3, the photos of the DSP control unit, the 6-phase RDCM under blocked rotor test and the 6-phase RDCM together with the Eddy-current dynamometer are shown.

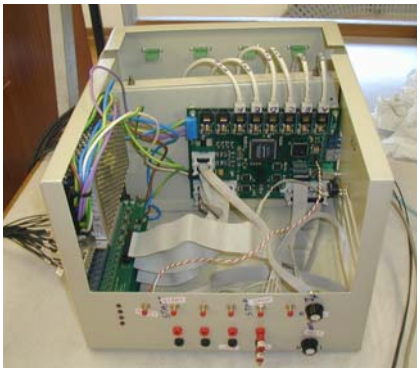

Figure E.1: DSP controller unit.

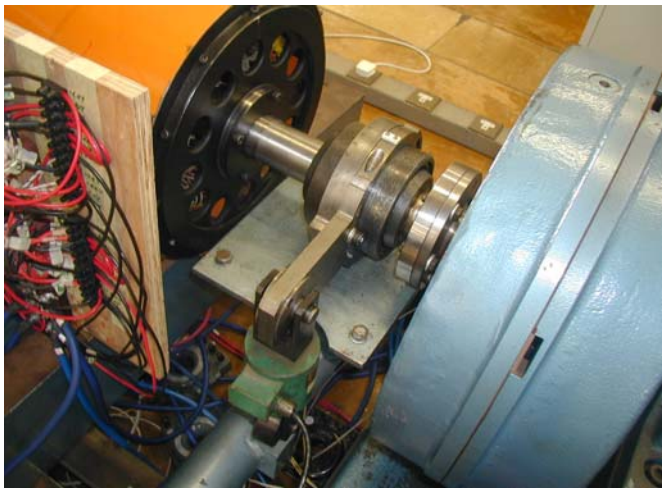

Figure E.2: 6-phase RDCM under blocked rotor test.

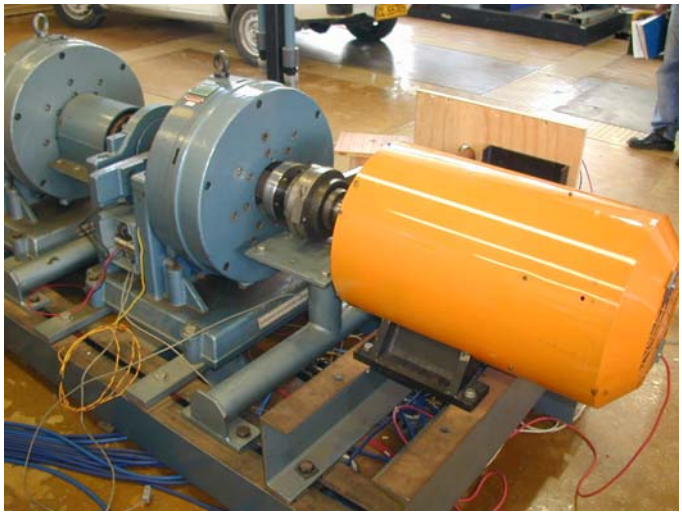

Figure E.3: 6-phase RDCM (orange) and the eddy current dynamometer (blue).